The Characterisation and Position Resolution of a Planar Germanium Strip Detector

Thesis submitted in accordance with the requirements of the University of Liverpool for the degree of Doctor in Philosophy

by

Jennifer Lynn Dobson

Oliver Lodge Laboratory

August 2005

Abstract

The Characterisation and Position Resolution of a Planar Germanium Strip Detector

Jennifer Lynn Dobson

This work presents the development of a high resolution detection system for use in positron emission tomography. HPGe segmented planar detectors will provide excellent energy resolution in addition to the three-dimensional position resolution achievable with pulse shape analysis, thus improving the granularity of the detectors beyond their electrical segmentation. The improved position resolution will allow the use of gamma-ray tracking to enable the reconstruction of Compton scattered events to increase the PET system detection sensitivity.

A prototype HPGe segmented planar detector (the *GREAT* planar) has been characterised. The *GREAT* planar is a high purity germanium strip detector that has 12 x 24 fold provided by the electrical segmentation of its two contacts into orthogonal strips. The response of the detector has been investigated by scanning a finely collimated source over the detector surface to calibrate pulse shapes as a function of interaction position.

The charge pulses arising from the scan data were compared to simulated pulse shapes. Differences between experimental and simulated pulse shapes were sufficient to re-examine experimental methods used to calibrate pulse shapes through the depth of planar detectors. Lateral position information across the strips was provided by analysing transient pulses induced in the detector. By validating transient pulse heights with those from simulated data, it has been shown that the *GREAT* planar detector has a two-dimensional position resolution of $\sim$1 mm to 2 mm at 662 keV.

Contents

Contents i

1 Introduction **1**

1.1 Positron emission tomography (PET) 1

1.2 SmartPET 3

1.3 Research overview 4

2 Principles of Radiation Detection and Measurement **6**

2.1 Interactions of photons with matter 6

2.1.1 The attenuation of photons 7

2.1.2 Photoelectric effect 8

2.1.3 Rayleigh scattering 8

2.1.4 Compton scattering 8

2.1.5 Pair production 10

2.1.6 Mean free path of gamma rays 10

2.2 Semiconductor detectors 11

2.2.1 Band structure in solids 11

2.2.2 The p-n junction 13

2.2.3 Germanium detectors 15

2.2.4 Planar HPGe detectors 15

2.3 The signal generation process 17

2.3.1 The electric field 17

2.3.2 Production of charge carriers 18

2.3.3 Signal generation 19

2.3.4 The anisotropic nature of drift velocity within germanium 21

2.4 Detector characteristics 23
2.4.1 Preamplifier 23
2.4.2 Efficiency 24
2.4.3 Energy resolution 25

3 Experimental Measurements 27
3.1 The *GREAT* planar detector 27
3.2 Digital acquisition 28
3.2.1 Digital signal processing 30
3.2.2 The scan 31
3.3 Experimental details 32

4 Detector Characteristics 39
4.1 Operational characteristics 39
4.1.1 DC offset and measured noise 39
4.1.2 Preamplifier response 40
4.1.3 Energy resolution measurements and noise evaluation 41
4.1.4 Efficiency measurements 46
4.1.5 Detector response to varying high voltage 46
4.2 Detector response to radiation events 48
4.2.1 Fold 48
4.2.2 Intensity per position 50
4.2.3 Crosstalk 54
4.2.4 Energy losses 56

5 Pulse Shape Analysis 61
5.1 Pulse shape analysis concepts 62
5.1.1 Rise time 62
5.1.2 Transient charges 64
5.2 Pulse shape analysis of the *GREAT* planar detector 66
5.2.1 Rise time distributions 66
5.2.2 Interaction depth determination 67
5.2.3 Lateral interaction position 74

6 Conclusion and Discussion **82**
6.1 Conclusion 82
6.2 Discussion 83
6.3 Future work 85

A Detector Characteristics **87**
A.1 Crystal orientation 87
A.2 Operational characteristics 87

B Electric Field Simulations **91**
B.1 Calculating the fields 91

C Collimator Simulation **97**

D Background Investigation **99**

List of Figures

List of Figures iv

2.1 Dominating interaction mechanism 7
2.2 Compton scattering 9
2.3 Band theory in solids 12
2.4 Donor and acceptor levels in semiconductors 13
2.5 Charge carrier migration across a junction 14
2.6 Lattice planes described using Miller indices and the diamond lattice structure 16
2.7 Schematic of a planar germanium detector. 17
2.8 The weighting field concept for a planar strip configuration . 22
2.9 A resistive feedback charge-sensitive preamplifier 24

3.1 Photograph of the *GREAT* planar detector 29
3.2 The *GREAT* planar geometry 29
3.3 A digitized pulse 30
3.4 Acquisition system 32
3.5 The complete scanning apparatus for the *GREAT* planar detector 33
3.6 Experiment 3. A fine scan 34
3.7 Experiment 4. A collimated source positioned at an angle to the detector 35
3.8 The EXOGAM Clover detector 37
3.9 Experiment 5. Planar plus Clover basic configuration 37

4.1 Energy resolutions at 60 and 122 keV for analogue and digital acquisition 43

4.2 Noise pulse from a typical boron(DC) strip 45
4.3 Charge collection noise contributions 45
4.4 Efficiency of the *GREAT* planar detector 47
4.5 Energy collected with varying high voltage 49
4.6 Strip fold 50
4.7 Intensity of counts per scan position 51
4.8 Intensity per fine scan position on boron(DC) 7. 53
4.9 Integrated counts on boron(DC) strips 53
4.10 Lithium(AC) energy collected versus boron(DC) energy collected 54
4.11 Schematic of considered fold 2 events 55
4.12 Add-back spectra 57
4.13 Fold 2 energy matrices 58
4.14 Zoomed fold 2 energy matrices 59
4.15 Fold 2 adjacent add-back spectra 60

5.1 Schematic demonstrating position dependent pulses shapes . 63
5.2 The small electrode effect 64
5.3 The parameters used to compare pulse shapes 64
5.4 An example of a net charge pulse and transient charge pulses 65
5.5 Lithium(AC) average rise time per scan position 68
5.6 Boron(DC) average rise time per scan position 69
5.7 Lithium(AC) rise time distributions 71
5.8 Boron(DC) rise time distributions 73
5.9 Simulated net charge pulses and their associated transient charge pulses 75
5.10 Transient heights as a percentage of real charge pulse height . 76
5.11 Transient charge pulses for varying interstrip interactions . . 77
5.12 Simulated transient charge pulse heights for varying interstrip interaction position 78
5.13 Transient charge pulse heights as a function of distance from interaction strip 81

6.1 Averaged 662 keV pulses calibrated at different depths in the first SmartPET planar detector 85

A.1 Crystal orientation of the *GREAT* planar detector. 87

B.1 Electric field simulation. Step 1: create geometry 94
B.2 Electric field simulation. Step 2: solve the electric potential . 94
B.3 Electric field simulation. Step 4: drift velocity of holes and electrons 95
B.4 Electric field simulation. Step 5: weighting field 96

C.1 1 mm collimator geometry and simulation results 98
C.2 2 mm collimator geometry and simulation results 98

D.1 1 mm collimated source moved in 1 mm steps in a lateral direction towards the crystal. 100
D.2 Background counts recorded 101

List of Tables

List of Tables vii

2.1 The mean free path of gamma rays in germanium 10
2.2 The physical properties of germanium 16

3.1 Summary of experiments performed 38

4.1 DC offset and peak-to-peak noise measured from preamplifier outputs for edge and centre strips 40
4.2 Analogue energy resolution results at 60 and 122 keV for edge and centre strips 42
4.3 Digital energy resolutions at 60, 122 and 662 keV for edge and centre strips 44

5.1 T30 rise-time gates used for large scale lateral position sensitivity measurements. 79

A.1 DC offset and noise measured from preamplifier outputs . . . 88
A.2 Analogue acquired energy resolution results at 60 and 122 keV for all strips 89
A.3 Digitally acquired energy resolutions at 60, 122 and 662 keV for all strips 90

B.1 Parameters required by MGS code to create matrices. 92

Chapter 1

Introduction

Advances in semiconductor technology led to the production of high-purity germanium (HPGe) detectors in the 1970's. Subsequently, HPGe detectors have been used extensively in gamma-ray spectroscopy to improve our knowledge of the nucleus. In recent years, electrical segmentation of HPGe detector contacts (electrodes) and their uses have been the focus of detector research, pushing the boundary of interaction position determination towards its fundamental limit. Many varieties of segmented coaxial and segmented planar geometry detectors have been used for an assortment of applications, from the large arrays of tightly packed detectors used in nuclear physics research [Nol94], to single detector Compton imaging devices [Bur03]. A new application in medical imaging has been devised employing double sided strip planar detectors in positron emission tomography (PET). The research of strip planar detectors for this application is the subject of this thesis.

1.1 Positron emission tomography (PET)

Positron emission tomography is a technique used in clinical medicine and biomedical research to create functional images. Radioactive nuclei are introduced into the body as labels on tracer molecules. These nuclei decay emitting positrons that annihilate with electrons in the tissue, producing two 511 keV gamma rays moving in opposite directions. The gamma rays

are detected in coincidence in oppositely situated detectors, and a line drawn between the detection points. Many lines are produced and used to build an image of the tissue where the tracer molecules are concentrated.

The intrinsic spatial resolution attainable with PET is limited by two factors, the range of the positron before it annihilates to produce two 511 keV gamma rays and the non-collinearity of the emitted 511 keV gamma rays due to a non-zero momentum of the electron and positron at annihilation. The range of the positron is dependent on its energy which varies with radionuclide and the resolution limits imposed by non-collinearity worsen with distance from emitter to detector. Present human clinical PET devices have a spatial resolution of $\sim$5 to 10 mm [Cha02].

For many reasons, in the last decade, the mouse has become the animal of choice for medical research. Imaging of a subject with such a vast difference in physical size to humans presents a significant challenge. Clearly the spatial resolution available is not sufficient for PET of small animals which would require resolutions of $<$1 mm. The detection sensitivity (fraction of decays that result in a detected valid event) must also be improved for animals with such a small mass. Cutting edge commercially available whole-body human PET scanners detect a maximum of $\sim$2 to 4 % of the coincident annihilation photons. Scaling this down to rodent size would require an increase in the detection sensitivity to preserve the number of counts per image resolution element.

Spatial resolution in PET has been constrained to the size of the crystal used for detection. Advances in PET have been made to reduce crystal size and increase the number of crystals used thus improving the sensitivity and active volume studied. Commercially available PET imaging devices for animals became available with the following specifications:

- The first animal PET detection systems were built for non-human primates and were based on the bismuth germanate (BGO) scintillator with photomultiplier tubes. Improvements made to the design now

give a volumetric resolution of 0.022 cc (2.6 x2.6 x3.2 mm^3 spatial resolution) in a 51 cm diameter ring of 60 detectors and 4 rings next to each other giving 11.4 cm detection field of view in the other direction [Wat97].

- Hammersmith RATPET was the first PET system specifically designed for rodent imaging. BGO blocks were arranged in an 11.5 cm diameter ring and length of 50 mm giving volumetric resolution near the centre of 0.026 cc [Blo95].

To improve the detector resolution, BGO crystals have been getting increasingly smaller, to a point now where the light yield of the scintillators is a limiting factor in their usefulness. Some of the research into improving PET detectors includes using a different scintillator material, lutetium oxyorthosilicate (LSO) [Cha99], which has a higher light output than BGO. Depth of interaction determination is being investigated [Hon04] by layering scintillator detector blocks. The use of HPGe double sided strip detectors to image small animals is being investigated by [Phl02] who quote limited success using 2 mm strip width for lateral position and pulse shape analysis for depth information. The group speculates that moving to 1 mm strip width will improve spatial resolution adequately for the required resolution for PET.

1.2 SmartPET

SmartPET is a small animal PET demonstrator being developed that utilises segmented HPGe planar detector technology. It aims to tackle the present deficiencies in PET, specifically, the high proportion of rejected events from Compton scattering and present spatial resolution; important for imaging small animals. Present technology limits the spatial resolution of a PET detector to the size of the crystals within the detector. Decreasing the crystal size and increasing the number of crystals only increases the complexity of the electronics and the algorithms needed. The use of segmented HPGe detectors in conjunction with digital Pulse Shape Analysis (PSA) is being researched to improve position sensitivity and to locate

interactions in three-dimensions for use in gamma-ray tracking. This will enable the interaction position of a gamma-ray photon to be identified with a much higher precision than is possible with the detector strips alone. The excellent energy resolution of germanium offers the possibility of improving system efficiency by utilizing scattered events rather than dismissing them and could even lead to the possibility of using multiple tracers.

Although detection sensitivity is improved with the use of three-dimensional PET, it can result in image degradation for interactions occurring in a non-perpendicular direction to the detector plane. In these circumstances depth of interaction information is crucial to preserving position resolution. Depth of interaction information will be given in the HPGe planar detectors with the use of pulse shape analysis. Improved interaction information in a lateral direction to the detector plane will be provided by the latest transient analysis techniques, providing interaction position information beyond the 5 mm strip width used in these detectors. Together, these methods of analysing pulse shapes will give the required position resolution of $\sim$1 mm for a small animal PET.

The scattering of gamma rays can occur external or internal to the detectors. Presently, all scattered gamma rays are rejected and not used for reconstruction. A major improvement could be made to detection sensitivity if these scattered gamma rays could be utilised. A future project proposal is to use gamma-ray tracking to reconstruct the path of the gamma ray as it scatters and is absorbed in the detector volume and thus assign a correct line of response with the other coincident gamma ray.

1.3 Research overview

The first research steps in this project are described in this work. A prototype HPGe orthogonal strip detector has been characterised to show the feasibility of using such detectors in PET. The aims of this work were:

- To investigate the response of the detector to radiation events, giving information on the charge collection process.

- To characterise the pulse shapes of the orthogonal strip planar HPGe detector at a grid of positions within the crystal volume.
- To show the achievability of pulse shape analysis as a method of improving the position resolution in three dimensions in a planar detector.
- To assess the necessity of modifications to the detector and experiment design for future detectors use as an imaging detection system.

Chapter 2

Principles of Radiation Detection and Measurement

The work for this research project was conducted using a semiconductor detector to detect gamma rays. As such, the background knowledge needed should include an understanding of the principles of radiation detection and measurement, this includes: how photons interact with matter; the basic principles of semiconductor detectors; the specific properties of germanium that are relevant; how signals are produced, and a description of the operational characteristics that the detector will display.

2.1 Interactions of photons with matter

Photons interact with matter by either scattering or complete absorption. The processes to be considered are: Rayleigh scattering; Compton scattering; photoelectric effect and pair production. Rayleigh scattering is elastic and therefore does not attenuate the intensity of the radiation. For the attenuating processes the dominating effect is related to the energy of the interacting photon, this can be seen in Figure 2.1. In the energy range of interest for this work, 60 keV to 662 keV, the major mechanisms for consideration are the photoelectric effect and Compton Scattering. Pair production occurs at energies $\geq$ 1.02 MeV and so it is not considered for the energy range of interest. For completion brief descriptions of Rayleigh scattering

and pair production have been included.

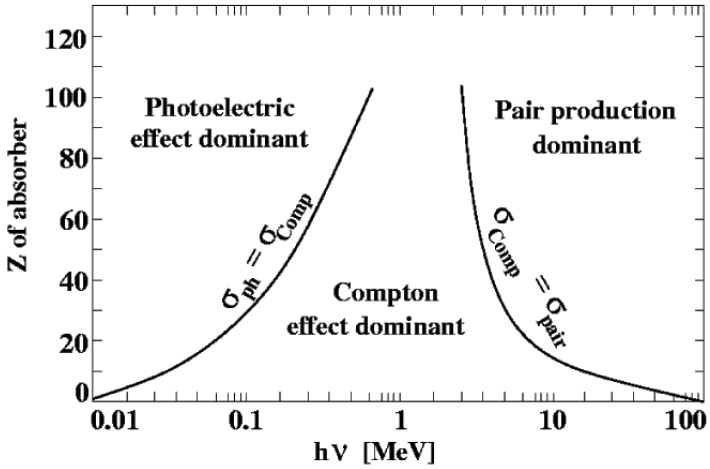

Figure 2.1: Dominating interaction is dependent upon energy of incident photon and Z of absorber.

2.1.1 The attenuation of photons

For X-rays and gamma rays the intensity of the radiation decreases as it passes through a material. This change in intensity, ΔI, is proportional to the thickness of the material, Δx, and it is also proportional to the incident intensity I.

$$\Delta I = -\mu I \Delta x \tag{2.1}$$

$$\mu = \tau(photoelectric) + \sigma(scattering) + \kappa(pairproduction) \tag{2.2}$$

μ is the linear attenuation coefficient or total cross section for absorption obtained by summing the individual cross sections from various processes. It is these interaction processes that will be outlined.

2.1.2 Photoelectric effect

For low energy X-rays and gamma rays ($\lesssim$150 keV in Ge), the photoelectric effect is the dominant interaction. The photon interacts with the atom as a whole and imparts all of its energy to a bound orbital electron. If this energy is greater than the binding energy of the electron in the atomic shell the electron is removed from its orbit, with the remaining energy transferred as kinetic energy. This high velocity electron is called a photo-electron and has an energy given by

$$E_{e^-} = E_\gamma - E_b \tag{2.3}$$

Where E_b is the binding energy of the photo-electron in the atomic shell. The interaction leaves a vacancy in the atomic shell which is filled by the capture of a free electron or by the re-arrangement of electrons from other shells in the atom. This results in the production of characteristic X-rays or Auger electrons. The cross section for photoelectric absorption increases with increasing absorber atomic number Z. A theoretical expression for the cross section for photoelectric absorption is provided by [Dav52]

$$\tau \approx constant \times \frac{Z^5}{E_\gamma^{3.5}} \tag{2.4}$$

2.1.3 Rayleigh scattering

Rayleigh scattering is a form of elastic scattering that occurs at energies < 1 MeV. The interaction is with bound atomic electrons whereby the electrons return to their original state after the interaction. The atom as a whole absorbs the momentum change and the scattered photon is re-emitted with the same energy as the incident photon. The cross section for Rayleigh scattering increases with Z, and the average deflection angle decreases as E_γ increases [Kno00a]. As the main effect of Rayleigh scattering is deflection, the process is not going to be addressed in this work.

2.1.4 Compton scattering

Compton scattering is an inelastic scattering process which results in an energy loss and change of direction for the incident photon. Of the scattering

processes, Compton scattering is the dominant interaction and in germanium it is dominant for incident photons of energy between ∼150 keV to ∼4 MeV.

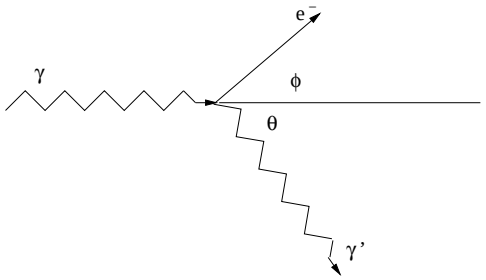

Figure 2.2: A gamma ray Compton scattering by an angle θ.

The incoming photon is deflected from its path by an angle θ, shown in Figure 2.2. The initial energy of the photon is divided between itself and a weakly bound electron, a recoil electron. Assuming the electron is unbound and at rest, the energy of the scattered photon can be found by applying the conservation of momentum and energy, resulting in Equation 2.5. A maximum energy is transferred to the electron when the photon is scattered by $\theta = 180°$.

$$E'_\gamma = \frac{E_\gamma}{1 + \alpha(1 - \cos\theta)} \tag{2.5}$$

Where $\alpha = E_\gamma / m_0 c^2$ and $m_0 c^2$ is the rest-mass energy of an electron (511 keV).

The angular distribution of scattered gamma rays can be predicted by calculating the differential cross section, $\mathrm{d}\sigma/\mathrm{d}\Omega$, using the Klein-Nishina formula [Dav65]

$$\frac{d\sigma}{d\Omega} = \frac{1}{2} r_0^2 \left(\frac{1}{[1 + \alpha(1 - \cos\theta)]^2} \left(1 + \cos^2\theta + \frac{\alpha^2 (1 - \cos\theta)^2}{1 + \alpha(1 - \cos\theta)} \right) \right) \tag{2.6}$$

Where r_0 is the classical electron radius. At energies of E<511 keV (α <1), the differential cross section reduces to the Thompson equation.

$$\frac{d\sigma}{d\Omega} = \frac{1}{2} r_0^2 (1 + \cos^2 \theta) \tag{2.7}$$

Integrating the differential cross section over all solid angles gives the Compton scattering cross section σ_c. For the cross section per atom, the Compton scattering cross section must be multiplied by the atomic number Z.

2.1.5 Pair production

Pair production can only occur for incident gamma-ray energies that are greater than twice the rest mass of an electron ($\geq$1.02 MeV). It takes place in the Coulomb field of a nucleus where the photon disappears and is replaced by an electron-positron pair. The electron-positron pair carry away any excess energy in the form of kinetic energy. After slowing down in an absorbing medium, the positron annihilates with a free electron producing two 511 keV photons. Pair production becomes the dominant interaction process above $\sim$4 MeV.

2.1.6 Mean free path of gamma rays

The mean free path is the reciprocal of the linear attenuation coefficient. It is defined as the average distance a gamma ray travels into a material before an interaction occurs. For the purposes of this work the mean free paths of three gamma-ray energies in germanium are shown in Table 2.1.

Energy (keV)	**photoelectric** $(1/\tau)$	**Compton** $(1/\sigma)$
60	0.1	1.1
122	0.5	1.3
662	> 100	2.4

Table 2.1: The mean free path (cm) in germanium for three energies of interest [Har84].

2.2 Semiconductor detectors

Solid state detectors are used in many radiation detection applications as they are more compact than their gas equivalents. The choice of solid state detector is between a scintillator and a semiconductor device. While scintillation detectors can offer high detection efficiency, they require a large energy to produce charge carriers ($\sim$100 eV). Fewer charge carriers are produced for a given interaction energy resulting in a poorer energy resolution. Conversely, semiconductors require a much lower energy ($\sim$ 3 eV) to produce a charge carrier and therefore for a given interaction energy they produce much larger numbers of carriers. With a larger number of carriers produced, the statistical fluctuation in carrier number is reduced and the energy resolution is much improved. For applications that require accurate energy determination a semiconductor detector is the device of choice.

2.2.1 Band structure in solids

The crystalline structure of solids can be described in terms of two energy bands, namely the valence and conduction bands. The valence band represents the region where electrons are bound in specific lattice sites in the crystal. The conduction band represents the regions where electrons are free to migrate within the crystal. These bands are separated by an energy gap, the size of the gap determines the electrical properties of the material. Figure 2.3 shows the band structure for metals, semiconductors and insulators.

Metals have either a partially filled valence band or overlapping valence and conduction bands. In both cases, electrons require only a very small energy to populate empty states. Consequently, metals have good conduction properties. Insulators have a full valence band and an energy gap that is too large to overcome, $>$ 5 eV, for conduction to occur. Semiconductors have an energy gap that is small enough, $\sim$ 1 eV, for some electrons to occupy the conduction band at room temperature. Electrons excited to the conduction band leave holes in the valence band. Conduction in a semiconductor is thought of in terms of the mobility of holes and electrons. At 0 K, with no

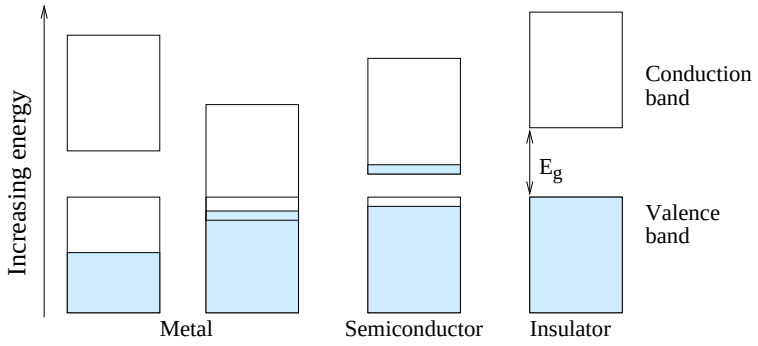

Figure 2.3: Band theory for metals, semiconductors and insulators at room temperature. The shaded areas represent energy levels that are filled with electrons.

thermal energy, semiconductors will have a full valence band and an empty conduction band, thus becoming an insulator.

Often in the band gap, the band structure can be greatly changed by doping the semiconductor material with an impurity. An impurity atom substitutes one of the semiconductor atoms in the lattice. The impurity atom will have an electron more or an electron less than the semiconductor atom it is replacing, this adds more electrons or holes into the semiconductor material. In an n-type semiconductor, the impurity atom has one electron more than the atom it is replacing. The extra electron will not form part of the lattice and can occupy energy levels within the band gap. These electrons are loosely bound and are easily excited to the conduction band. Impurity atoms of this type are called donor atoms. In a p-type semiconductor the impurity atom has one electron less than the atom it is replacing. When this atom replaces a lattice atom, it creates a vacancy or hole that can be filled. The electron that fills this hole will have a different energy to other lattice electrons because one of the atoms it is bonding with is the impurity atom. These impurity atoms are called acceptors and they provide acceptor levels near the bottom of the band gap. Figure 2.4 is an illustration of the donor and acceptor levels within the band gap.

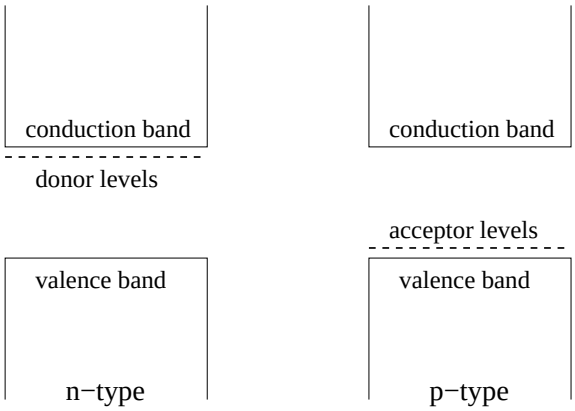

Figure 2.4: Donor and acceptor levels in n-type and p-type semiconductors.

2.2.2 The p-n junction

If n-type and p-type semiconductors are brought together with a good contact between the two, diffusion of the charge carriers occurs across the junction. Electrons diffuse from the n-type material migrating across the junction to combine with acceptor atoms. Holes diffuse from the p-type material across the junction and combine with donor atoms. The action of diffusion of both charge carriers creates a region surrounding the junction with no mobile charge carriers, a depleted region. The zones on either side of the this depletion region have an excess of charge. This diffusion of charge carriers is shown in Figure 2.5. An excess of electrons in the p-type material and an excess of holes in the n-type material creates an electric field across the depletion region. A small potential difference therefore exists across the depletion region acting to oppose the flow of electrons and holes across the junction.

In its present state, the p-n junction will operate as a radiation detector. The interaction of photons within the detector will produce electron-hole pairs, but the weak electric field is not large enough to move the charge carriers and recombination can occur. For the semiconductor to act as a detector a reverse bias has to be applied to increase the depletion region and electric field. A positive voltage is applied to the n^+ contact with respect to

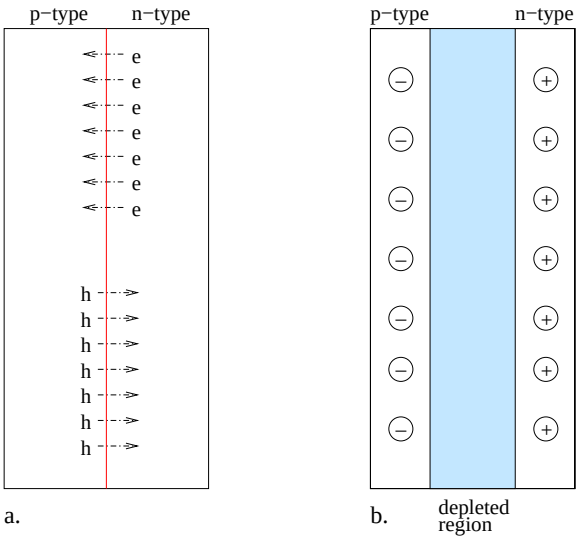

Figure 2.5: (a) shows the migration of holes and electrons across a junction. (b) shows the resulting depletion region and excess of charge beyond it.

the p^+ contact, attracting electrons away from the junction. This increases the depletion region and thus the detector's ability to detect radiation. A detector is normally operated with a full-depletion voltage, which is the voltage required to deplete the whole volume of the crystal. Semiconductor detectors are operated above this full-depletion voltage to ensure the electric field is strong enough throughout the crystal for full charge collection to occur. A full derivation of the depth of the depletion region can be found in [Sze02a]. A more generalized solution for the thickness d of the depletion region is given by [Kno00b]:

$$d \cong \left(\frac{2\epsilon V}{eN}\right)^{1/2} \tag{2.8}$$

Where N is the net impurity concentration in the semiconductor material, ϵ is the dielectric constant, e is the charge on an electron, and V is the applied voltage.

2.2.3 Germanium detectors

For many detector applications, germanium is the semiconductor material of choice. It is a group IV semiconductor with a crystalline diamond lattice structure (face centered cubic). The lattice is described as two interpenetrating sublattices and consequently has some characteristics that depend on the crystal orientation. A schematic of the diamond lattice and different crystal orientations can be seen in Figure 2.6. Germanium has the basic physical properties shown in Table 2.2.

Germanium is widely used in detector technology for a number of reasons. It has a larger atomic number than its competitor silicon (Z=14), and therefore a larger attenuation coefficient making it more useful for detecting higher energy gamma rays. In a germanium detector, the depletion region still has to be large enough to stop gamma rays fully ($\sim 25\,\text{mm}$ for $662\,\text{keV}$ gammas). From Equation 2.8 it can be seen that the depletion width is inversely proportional to the net number of impurity atoms. Reducing the number of impurity atoms and increasing the depletion width can be done in two ways. The first method is to introduce a dopant to balance out impurities and compensate the semiconductor material, lithium donor atoms are added to germanium. It is difficult to exactly match the dopant and impurities, so the resulting crystal is either n or p type. The other method of reducing the net impurity concentration is to refine the crystal to remove a large percentage of the impurities leaving a high purity crystal. While both of these methods increase the achievable depletion depth, the manufacturing of high purity germanium (HPGe) detectors has become more widespread because they are more robust and can be warmed without damaging the crystal.

2.2.4 Planar HPGe detectors

Planar HPGe detectors are limited in size to a few centimeters in depth by both the production process and by the achievable depletion depth. When fully depleted and operated at a sufficient over voltage, the electric field in the non-segmented planar detector is uncomplicated and preferable to that

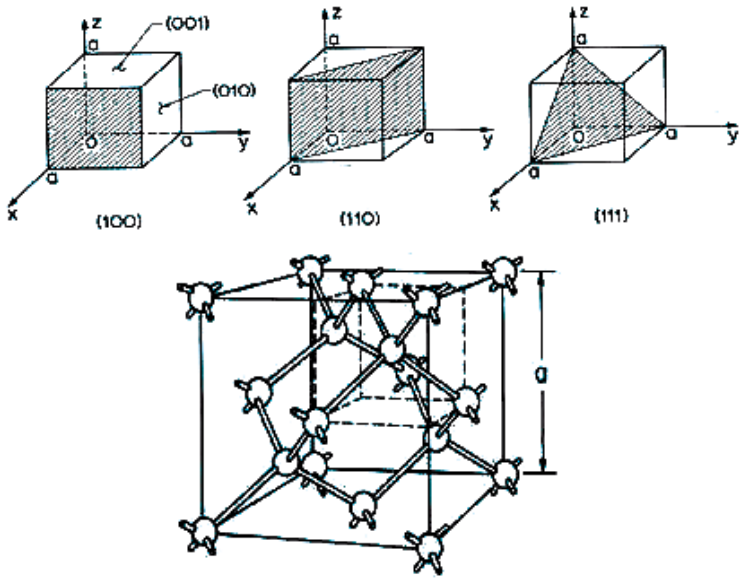

Figure 2.6: Top: Lattice planes described using Miller indices. Bottom: Diamond lattice structure.

Atomic number Z	32
Atomic weight A	72.6
Atoms	4.4 x 10^{22} cm^{-3}
Density	5.32 g/cm^3
Crystal structure	diamond (FCC)
Dielectric constant ϵ_r	16.2
Intrinsic carrier concentration (300 K)	2.0 x 10^{13} cm^{-3}
Intrinsic resistivity	46 Ω·cm
Energy gap (300 K)	0.67 eV
Energy gap (0K)	0.75 eV
Ionization energy (77 K) ϵ_{pair}	2.96 eV
Fano factor (77 K)	0.08
Electron mobility (300 K)	3900 $cm^2/V{\cdot}s$
Hole mobility (300 K)	1900 $cm^2/V{\cdot}s$

Table 2.2: The physical properties of germanium, [NSM]

produced by coaxial geometries. A planar germanium detector can have excellent low energy resolution and efficiency, ideal for detecting X-rays and low energy gamma rays.

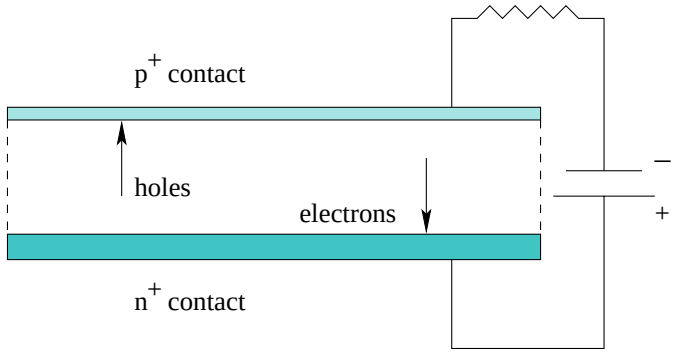

Figure 2.7: Schematic of a planar germanium detector.

2.3 The signal generation process

Signals are produced in semiconductor detectors following the interaction of a photon within the detector and consequently the production of charge carriers. A signal is induced in contacts by the movement of these charge carriers under the influence of an electric field.

2.3.1 The electric field

To determine the drift velocity of a charge carrier at any point the electric potential, $V(x)$, must be found for all points within the detector volume. For a planar geometry this is done by solving the Poisson equation in one dimension:

$$\frac{d^2V(x)}{dx^2} = -\frac{\rho(x)}{\epsilon_0\epsilon_r} \tag{2.9}$$

Where ρ is the charge density.

For a full depletion voltage the electric field can be calculated for any point by taking the gradient of the electric potential:

$$\mathcal{E}(x) = -\frac{dV(x)}{dx} \tag{2.10}$$

2.3.2 Production of charge carriers

The interactions of photons with matter excite atomic electrons by the processes outlined in section 2.1. These excited electrons then lose their energy in the material by further ionization and excitation of secondary charged particles (inelastic collisions), and by radiative losses (bremsstrahlung). The total energy loss for electrons is a sum of the collisional and radiative losses:

$$\left(\frac{dE}{dx}\right)_{tot} = \left(\frac{dE}{dx}\right)_{coll} + \left(\frac{dE}{dx}\right)_{rad} \tag{2.11}$$

Electrons follow a deviant path through a material colliding with many atomic electrons. The theory to calculate the mean energy loss caused by these collisions (collisional energy loss of light charged particles) was developed by Bohr, Bethe and Bloch as an adaptation of the theory for losses of heavy charged particles in a material. For small energies ($\beta < 0.5$, $E < 590\,\mathrm{keV}$ for electrons), this is given by [Knp65a]:

$$-\left(\frac{dE}{dx}\right)_{coll} = \frac{4\pi e^4 NZ}{m_0 v^2} \ln \frac{1.16 m_0 v^2}{2I} \tag{2.12}$$

N is the number of atoms per cm^3, I is the mean excitation energy of the atomic electrons and m_0 is the rest mass of the charged particle. For relativistic light charged particles this version of the Bethe-Bloch expression becomes [Knp65a]:

$$-\left(\frac{dE}{dx}\right) = 0.153\rho\frac{Z}{A}\beta^{-2}\left[\ln\frac{E(E+m_0c^2)^2\beta^2}{2I^2 m_0 c^2} + (1-\beta^2) - \right.$$

$$\left.(2\sqrt{1-\beta^2} - 1 + \beta^2)\ln 2 + \frac{1}{8}(1-\sqrt{1-\beta^2})^2 - \Delta_{pol}\right] \tag{2.13}$$

Z, A and ρ are specific to the absorber material and Δ_{pol} accounts for a reduction in the Coulomb field of the incident electron in high density materials due to the polarizability of the material.

Electrons can undergo large accelerations in the Coulomb field of nuclei because of their low mass, and consequently can emit bremsstrahlung radiation. The mean energy loss per cm path due to this radiation is given by [Knp65b]:

$$\left(\frac{dE}{dx}\right)_{rad} = Nr_0^2 \frac{Z^2}{137}(E + m_0c^2)\left[4\ln\frac{2(E + m_0c^2)}{m_0c^2} - \frac{4}{3}\right] \tag{2.14}$$

From equation 2.14, it can be seen that radiative losses are proportional to electron energy and the square of the atomic number of the absorber material. For typical electron energies, radiative losses are low and are reabsorbed close to the point of emission; only becoming dominant above tens of MeV.

The interaction of radiation produces electron-hole pairs within the semiconductor material. The number of pairs created depends on the energy deposited during the interaction. A quantity of interest is the ionization energy ϵ_{pair}, which is the energy required to form one electron-hole pair and is higher than the energy band gap in that material. The difference is due to a part of the deposited energy being dissipated as lattice vibrations. For germanium the difference between the two can be seen in table 2.2. The number of electron-hole pairs created when an energy E is deposited is:

$$\overline{N} = \frac{E}{\epsilon_{pair}} \tag{2.15}$$

The number of electron-hole pairs created is subject to statistical variations. The observed variance is smaller than that predicted by a Poisson variance and is taken into account by introducing the Fano factor (F).

$$\sigma_N^2 = F\overline{N} \tag{2.16}$$

2.3.3 Signal generation

According to [Dab89], there are two possible methods of describing the transport of charge carriers in the space-charge region. The first one treats the free charge carrier distributions as continuous functions of the space and

the time coordinates, and uses the transport equations. The second method considers each charge carrier individually according to Ramo's theorem, and the effects due to particular carriers are summed. As the currents observed in a detector are those from induced currents, the Ramo's theorem method is the one that is widely used to predict charge carrier transport and their associated induced currents within a semiconductor detector. The instantaneous value of the induced current due to the motion of a charge carrier was solved by both Shockley[Sho38] and Ramo[Ram39], and is generally known as Ramo's theorem given by:

$$i(t) = q\frac{E(x,t)v_d(x,t)}{V(x)} \tag{2.17}$$

v_d is the drift velocity of the carrier, E is the electric field intensity and V is the electric potential of the electrode. Shockley reduced Equation 2.17 for two infinite parallel planes a distance w apart and with a uniform electric field distribution:

$$i(t) = q\frac{v_d(t)}{w} \tag{2.18}$$

To calculate the current as a function of time, the concept of a weighting field, E_w, is introduced. The weighting field is a measure of the electrostatic coupling between the moving charge and the sensing electrode. For a segmented detector the weighting field is different from the electric field which only determines the charge trajectory and velocity. The weighting field is calculated by solving the Poisson equation for a potential of 1 V on the electrode of interest and placing all other electrodes at 0 V. For a planar configuration the shape of the weighting field can be shown by plotting the equipotential lines as shown in Figure 2.8.

The calculation of the induced charge is given by Radeka[Rad88a], who considers all electrodes to be grounded apart from the sensing electrode and an infinitesimal electrode, the moving charge. The potential applied to the sensing electrode induces a charge on the moving electrode and by the reciprocity theorem, the moving electrode has a potential that induces a charge on the sensing electrode.

$$\frac{Q_S}{V_m} = \frac{q_m}{V_S} = C_{Sm} \tag{2.19}$$

$$q_m.V_m = Q_S V_S \tag{2.20}$$

where Q_S is the charge induced on the sensing electrode, q_m is the charge induced on the moving electrode, V_S and V_m are the electrodes' potentials and C_{Sm} is the partial capacitance between the two electrodes. The induced current $i_S = dQ_S/dt$ is due to the motion of the charge q_m along a line dl, moving with velocity $v = dl/dt$,

$$i_S = \frac{d(q_m V_m)/dt}{V_S} = q_m \frac{(V_m/V_S)}{dl}.\frac{dl}{dt} \tag{2.21}$$

By considering a normalised potential at point m, we get a normalised field E_w and so the induced current in the sensing electrode is,

$$i_S = -q_m.E_w v \tag{2.22}$$

To get the total induced charge,

$$Q_S = \int i_S dt = -q \int_{m_1}^{m_2} E_w dl = q\left[V_w(m_1) - V_w(m_2)\right] \tag{2.23}$$

The induced charge in the sensing electrode is given by the difference in the weighting potentials V_w between two positions of the moving charge, m_1 and m_2.

2.3.4 The anisotropic nature of drift velocity within germanium

The crystalline structure of germanium results in a band structure that is anisotropic at low temperatures and electric fields above $\sim 10^2$ Vcm^{-1}. This leads to variations in the drift velocities of holes and electrons that depend on the direction of the applied field with respect to the direction of the lattice [Mih00]. The analysis of pulse shapes is dependent on the mobility/drift velocity of the charge carriers being known. In coaxial detector geometries, the interaction position of ionizing radiation could result in carriers moving along a fast or slow crystal orientation or somewhere in between. The only

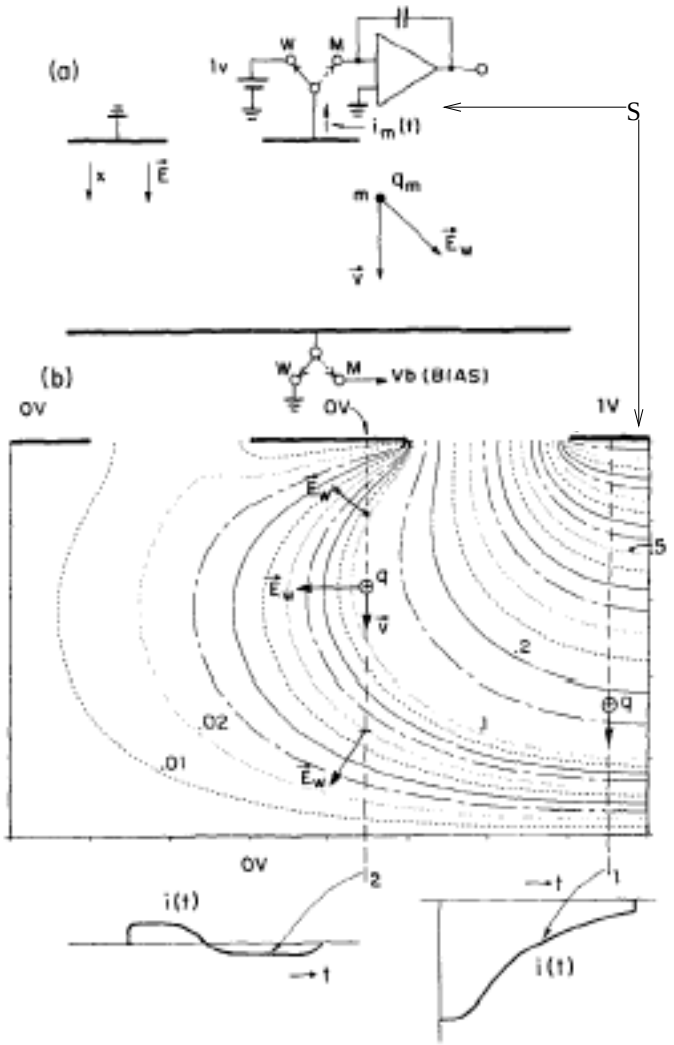

Figure 2.8: [Rad88b] (a) Determination of the weighting field concept for a planar strip configuration. The weighting field is the field for a potential of 1 V on the sensing electrode S and 0 V for all other electrodes. The weighting field is shown in (b) as a plot of equipotential lines. Two examples of charge transit are shown that result in two different types of charge pulses. One with a net charge collected on the sensing electrode and one with no net charge on the sensing electrode (a transient). In reality, the sensing electrode is connected to a charge amplifier and a uniform electric field is achieved by applying a bias to the opposite electrode.

consideration for a planar germanium detector is that the orientation of the germanium crystal along the detector depth is parallel to one of the slower crystal orientations and this orientation is known for simulation purposes.

2.4 Detector characteristics

Preamplifiers are an integral part of high purity germanium detection systems. The signal to be analysed is the output from the preamplifier and therefore the particular specifications of a preamplifier are important for the type of output required. The usefulness of the whole detection system for gamma-ray spectroscopy can be determined by a few simple characteristics, including detection efficiency and energy resolution. A description of these simple detector characteristics has been included.

2.4.1 Preamplifier

The aim of the preamplifier is to extract the output signals from the detector with as little degradation as possible and prepare them for signal processing. There are three basic types of preamplifier: the current sensitive preamplifier; the parasitic preamplifier; and the charge-sensitive preamplifier.

For HPGe detectors, where energy determination is essential, it is crucial for the preamplifier to have low noise and stable sensitivity. This is achieved by the use of a charge-sensitive preamplifier with a Field-Effect Transistor (FET). In an ideal situation, the least noise would be produced using a cooled FET which is usually placed inside the cryostat. This has an added advantage of keeping the preamplifier as close to the detector as possible reducing the input capacitance caused by cabling, thus reducing the risk of crosstalk. Crosstalk in this instance is the capacitive coupling from one part of the electronics/circuit to another and is discussed in more detail in Section 4.2.3.

The charge-sensitive preamplifier gets its stability from integrating the charge on a feedback capacitor, thus gain is not sensitive to changes in detec-

tor capacitance. It is then discharged through a feedback resistor producing the long pulse decay time. A schematic of the charge-sensitive preamplifier is shown in Figure 2.9. In an ideal case the rise time of the output pulse will be equal to the detector current pulse width.

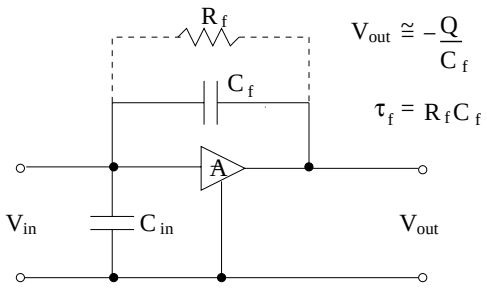

Figure 2.9: Simplified diagram of a resistive feedback charge-sensitive preamplifier configuration [Kno00c]. If the time constant is large compared with the charge collection time, then the output pulse will have an amplitude V_{out}.

2.4.2 Efficiency

The efficiency of a detector is a measure of detection sensitivity; how well it actually detects emitted or incident radiation. There are numerous ways to quote the efficiency, the following are just a few:

- Absolute efficiency is the number of detected events divided by the number of disintegrations of a source. It is therefore affected by the type of detector, source and source geometry.
- Relative efficiency of a germanium detector is quoted relative to the efficiency of a NaI(Tl) crystal. The NaI(Tl) efficiency is measured with a crystal 76 mm in diameter and 76 mm in length, and with the source placed at a distance of 25 cm from the front face.
- Intrinsic efficiency is a measurement independent of geometry. It is defined as the number of detected events divided by the number of particles incident on the detector.

2.4.3 Energy resolution

To determine the energy of a gamma ray interaction, the energy deposited in a detector must be quantified. How well a detecting system can distinguish between two interactions close in energy is referred to as the energy resolution, and is defined as the width of the energy peak at half its maximum height or full width half maximum (FWHM). There are a number of contributing factors that affect the total width of an energy distribution (W_T) and these are added together in quadrature to result in the observed energy resolution.

$$(W_T)^2 = (W_D)^2 + (W_X)^2 + (W_E)^2 \tag{2.24}$$

- W_D is an intrinsic value due to the statistical variation of charge carrier production in the detector. This is given by [Kno00d]:

  $$(W_D)^2 = (2.35)^2 F\epsilon E \tag{2.25}$$

  Where F is the Fano factor, ϵ is the energy required to form an electron-hole pair, and E is the gamma ray energy. All other width broadening contributions can be minimized by design, but this value is a basic characteristic that cannot be reduced.

- W_X is the width broadening from variations in charge collection efficiency. This incomplete charge collection is usually associated with low field regions within a detector. This contribution can be estimated by measuring the FWHM at different values of high voltage. A plot of FWHM versus HV^{-1} can be extrapolated back to zero, i.e. an infinitely large high voltage with no low field regions. The FWHM at this point has W_X removed and equals a sum of the other noise contributions.

- W_E is a contribution from random noise within the detector and instrumentation, i.e. electrical noise. The W_E contribution from the preamplifier can be determined by injecting a stepped pulse into the

preamplifier input and measuring the root-mean-square noise voltage at the output [Ort].

$$W_E = 2.35 \frac{E}{V_{pulse}} V_{rms} \tag{2.26}$$

E is the equivalent known energy of the charge injected into the input, V_{pulse} is the amplitude of the pulse resulting from the injected charge and V_{rms} is the root-mean-square noise voltage of the output.

- Gain drifting during measurement can also result in a broadening of the peaks. This contribution has not been added to Equation 2.24.

Chapter 3

Experimental Measurements

This chapter includes a detailed description of the detector, the acquisition system used for this research work, and also a description of the experimental procedures.

3.1 The *GREAT* planar detector

The prototype detector for the imaging project was the *GREAT* planar detector manufactured by Ametec(Ortec). It was delivered to the Oliver Lodge Laboratory in December 2002 on loan from the *GREAT* spectrometer[1]. A photograph showing the detector can be seen in Figure 3.1, while schematics can be seen in Figure 3.2. The detector is a high purity germanium (HPGe) orthogonal strip detector comprising a 130 mm x 70 mm HPGe tile instrumented with 5 mm readout strips. The rectangular anode which is connected to the polarization voltage has a 5 mm full perimeter safeguard ring. Similarly, the cathode which is connected to the ground has a 5 mm safeguard ring. The anode contact was created by lithium diffusion and is 0.7 mm deep. This contact has 12 horizontal strips, each of width 5 mm. The inter-strip distance is 0.7 mm. The cathode contact was created by boron ion implantation and is $0.3\text{x}10^{-3}$ mm deep. This contact has 24 vertical strips, each of width 5 mm. Here, the inter-strip distance is 0.1 mm.

[1]The *GREAT* spectrometer is a system of silicon, germanium and gas detectors designed to measure the radioactive decays of nuclei transported to the focal plane of the gas-filled separator RITU in Jyväskylä.

The strip contacts are orthogonal on either side of the 15 mm thick germanium slab. The impurity concentration varies across the 130 mm length of the crystal, having a concentration of 5 x 10^{+9} cm^{-3} N-type at channel 1, to 1 x 10^{+9} cm^{-3} at channel 24. The crystal is housed in 2 mm thick aluminium casing. The casing has a 0.5 mm thin beryllium window in front of the boron implanted contact (cathode); to allow low energy gamma rays and x-rays to penetrate through to the crystal, and a 1.1 mm thin aluminium window in front of the lithium diffused contact (anode); to allow higher energy photons to scatter into an analyser when used in *GREAT*. A view of crystal orientation is available in Appendix A.

The crystal is fully depleted at +600 V and an operating voltage of +800 V is applied to the lithium diffused contact. Each strip employs a Heidelberg-Cologne fast rise time preamplifier with warm FETs. The gain of the preamplifiers is ~500 mV/MeV into 100 Ω impedance. Both contacts, lithium(AC) and boron(DC), have post preamplifier signals of positive polarity.

3.2 Digital acquisition

Pulses from the preamplifiers are digitized to enable pulse shape analysis of the detector signals. An example of a digitized pulse can be seen in Figure 3.3. Analogue signals only give energy and time information, whereas digitized signals have many advantages including:

- the use of pulse shape analysis to give position information in addition to energy and time; E, t, x, y, z.
- improved gain stability from no longer needing to use a spectroscopy amplifier.
- digital systems offer high count rate abilities.
- digitized pulses can be corrected for effects i.e. deconvolving the decay to improve energy calculations.
- digital signals can be processed either online or offline.

Figure 3.1: Photograph of the *GREAT* planar detector

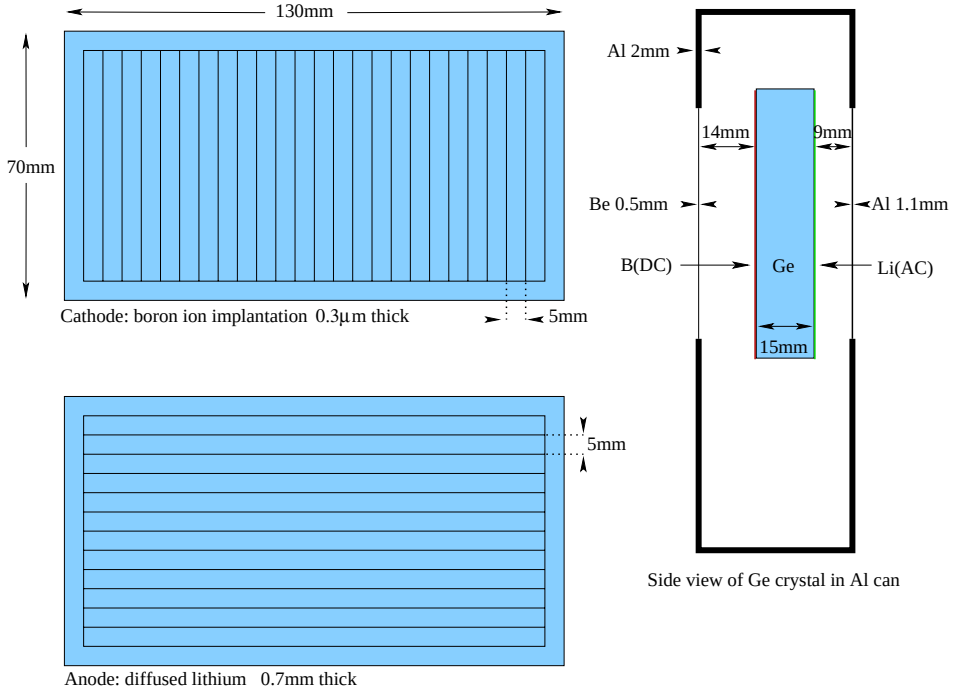

Figure 3.2: *GREAT* planar geometry showing the segmentation of the two contacts and a side view of the crystal inside its housing.

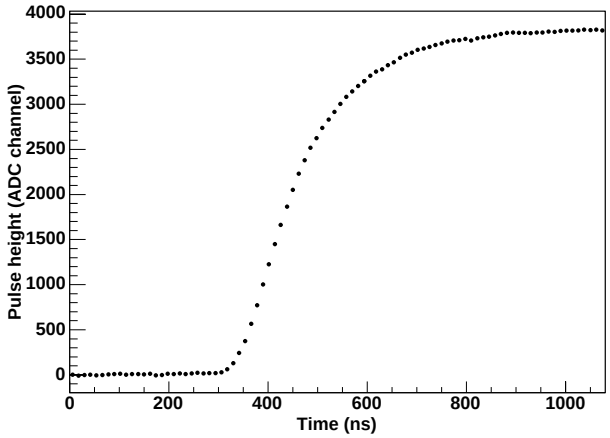

Figure 3.3: An example of a digitized pulse showing discrete pulse sampling.

3.2.1 Digital signal processing

Following the preamplifiers, the signals are passed to pulse processing cards. The cards used were Gamma-Ray Tracking 4 channel (GRT4) VME cards developed at Daresbury laboratory, UK [Laz03]. The cards were designed to process pulses in gamma-ray tracking arrays. These cards digitize and process the charge pulses from segmented germanium detectors and can be programmed with suitable algorithms to determine the interaction position and energy deposited in the detector, as well as time stamping the data to enable pulse comparison.

Each card includes:

- Four acquisition channels; operational in parallel.
- Each channel has a 14 bit 80 MHz flash analogue-to-digital converter (FADC); AD6645.
- Analogue inputs are filtered with a low pass filter and include an optional differential stage; ADC can accept a raw or differentiated input.

The processing of the ADC output is performed by two dedicated Xilinx Spartan field programmable gate arrays (FPGA). These can serve sev-

eral purposes: time-stamping data; programming a pre-trigger delay; digital tracking algorithm; energy determination algorithm; pulse timing, i.e. rise times and an interaction position algorithm. For this project, the FPGA's were largely unprogrammed giving the data only a time-stamp, this collection of unfiltered data is called oscilloscope mode. Readout occurs using a VME bus using the block transfer protocol. Pulses are stored over 512 samples that are read out to a PC for online analysis and to a storage device for offline analysis.

The GRT4 cards are 80 MHz giving a 12 ns time interval per sample. For the 512 samples recorded this results in a 6.4 μs sampling window. The choice of 512 samples was made to cover as much of the full pulse as possible to ensure algorithms could be improved, while limiting the amount of storage needed. The 14 bit dynamic y-range of the FADC's correspond to 16383 units of arbitrary magnitude digitized over -1 V to +1 V and giving a sensitivity scale of 0.12 mV per unit.

The cards were used with an external trigger provided by one of the twelve horizontal lithium strips. The trigger was set to above noise level and was achieved by routing the twelve signals through timing filter amplifiers (TFA) followed by constant fraction discriminators (CFD) and into a logical *OR*. This trigger was fed into the GRT4 cards where signals from all thirty-six channels were read. While the GRT4 cards were busy, an inhibit signal was sent to the trigger to stop any further signals being processed by the cards until all previous signals had been passed on to the CPU and to storage and sort. A schematic of the digital acquisition can be seen in Figure 3.4

3.2.2 The scan

The detector response as a function of the incident gamma-ray position has to be characterized. This was achieved by producing detailed scans of the response of the detector when collimated sources were moved in two dimensions across the detector surface. The detector dewar was not designed to be multi-positional, i.e. can only be used in an upright position and therefore the detector could not be turned on its side to be placed on

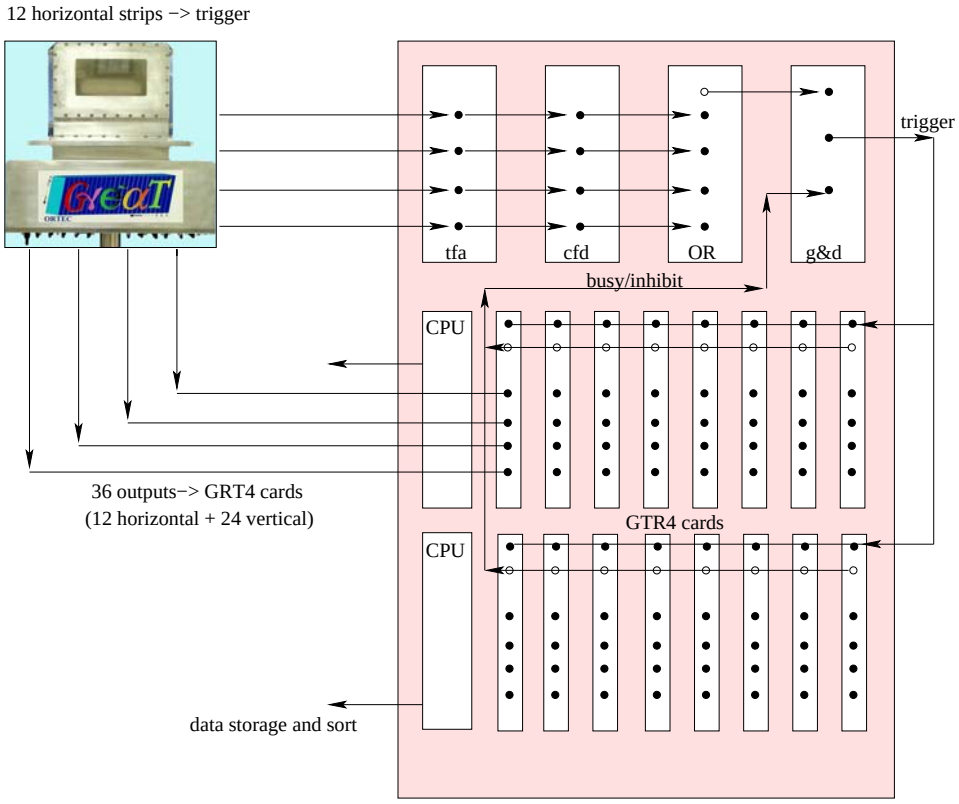

Figure 3.4: Acquisition system

the Liverpool x-y scanning apparatus. A schematic of the complete scanning apparatus used can be seen in Figure 3.5. To enable a scan of the detector surface, the y-direction of an automated x-y positioning table and a z-direction manual adjustment apparatus were used to pass the collimated sources across the detector surface.

3.3 Experimental details

A series of experiments was carried out on the detector. For all experiments the data were acquired using the digital acquisition system stated

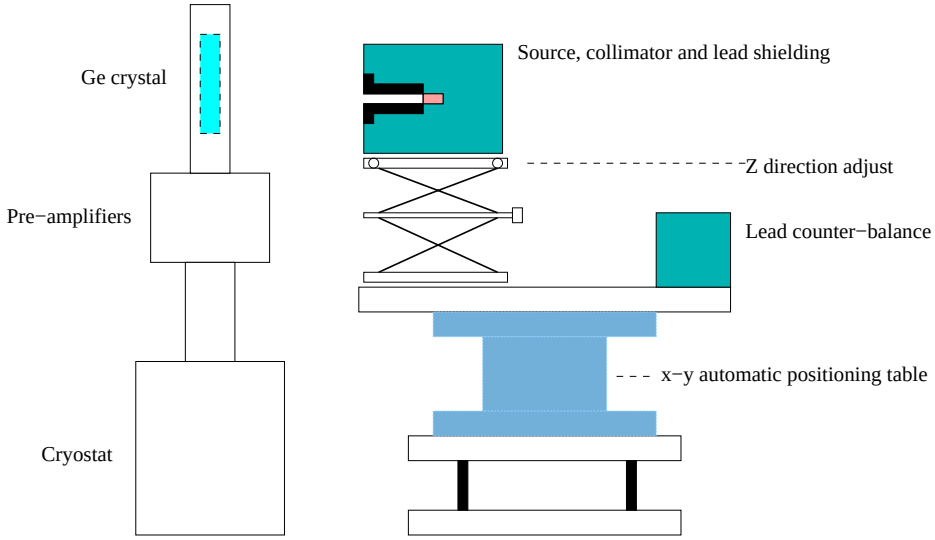

Figure 3.5: The complete scanning apparatus for the *GREAT* planar detector

and recorded on SDLT 160/320 tapes. The details of all experiments will be outlined:

1. Three uncollimated point sources placed together in front of the beryllium window on the boron(DC) side of the detector: Americium-241 0.181 MBq (0.005 mCi); Cobalt-57 0.007 MBq (0.2 μCi) and Caesium-137 0.327 MBq (0.009 mCi). A total of 23.5 GBytes of data were recorded to tape from all three sources.

2. A coarse scan of the full surface of the *GREAT* planar detector was performed using a collimated source incident on the boron(DC) surface at step intervals of 2 mm and staying at each position for 120 seconds. The collimator used was 80 mm in length and 2 mm in diameter. The source used was a 7.4 MBq (0.2 mCi) Co-57 source. Data from a total number of 2448 positions were collected with a count rate of 79 counts per second detected by the *GREAT* planar. A total of 1.4 TBytes of

data were recorded.

3. A finer scan of a smaller section of the surface of the detector was performed using the same Co-57 source as experiment 2. and this again was incident on the boron(DC) surface. The collimator was 40 mm long and had 1 mm diameter. The reduced length of the collimator was necessary to allow for a reasonable count rate. The collimated source stayed at each position for 300 seconds and the step interval was 1 mm. Data from a total number of 945 positions were collected with a count rate of $\lesssim$13 counts per second coming through the acquisition system, as illustrated in Figure 3.6. A total of 147 GBytes of data were recorded to tape.

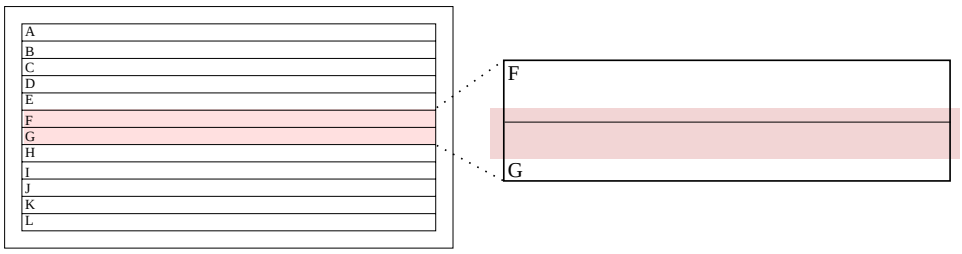

Figure 3.6: Experiment 3. On the right is a blow-up of the area of the detector where the 1 mm x 1 mm fine scan was performed. The shaded area shows the scanned region running from strip F, across a boundary and into strip G.

4. A collimated 11.1 MBq (0.3 mCi) liquid Caesium-137 source was placed at an angle to the boron(DC) surface of the detector to record depth of interaction of the 662 keV gamma ray. This would be done by measuring the number of photoelectric interactions occurring over more than one of the boron(DC) strips, but the lead block used in the collimation was a limiting factor to the size of the angle the collimated source made with the detector surface. This was determined to be insufficient

to give the desired results and therefore the data were not analysed for the measurement. The collimator used was 80 mm in length and 2 mm diameter. The collimator made an angle of 63 degrees with the y-z plane of the detector and the centre of the collimator was 29 mm from the crystal surface, pointing at boron(DC) 14 and lithium(AC) 7; a schematic of the set-up can be seen in Figure 3.7. A count rate of 63 counts per second and a total of 21 GBytes of data were recorded to tape.

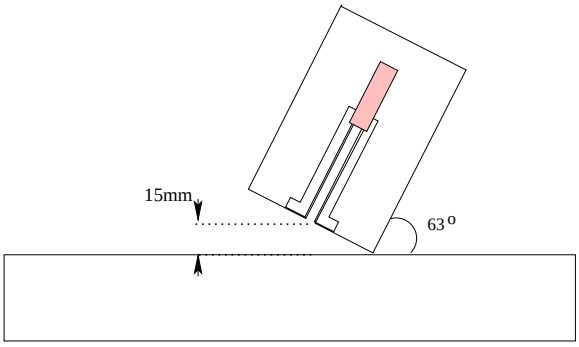

Figure 3.7: Schematic showing the collimated source at an angle with the plane of the detector. The liquid source is contained in a plastic phial of dimensions 15 mm length and 4 mm diameter.

5. An experiment was devised to record events scattered out of the planar detector into a larger volume detector. The large volume HPGe detector used was an EXOGAM Clover. The Clover has four segmented crystals encapsulated together, the basic dimensions can be seen in Figure 3.8. The characterization of this Clover is the work of S.Gros [Gro05] and will not be discussed further in this work. For all the following coincidence experiments the source used was 11.1 MBq (0.3 mCi) Cs-137 collimated with a 80 mm long, 5 mm diameter collimator placed 7 mm away from the boron(DC) face of the planar de-

tector. While in coincidence mode the acquisition system recorded 6 counts/second. The set-up of the planar plus clover can be seen in Figure 3.9.

(a) The distance between the two detectors was 18 mm. Data were collected in coincidence mode using a logical *AND* between any one of the four Clover central contacts and any of the twelve planar lithium strips. A course scan of step length 5 mm and duration 300 seconds/step, was performed over a limited area of the detectors covering 60 mm x 20 mm of the overlap region of the two detectors.

(b) The detectors were pushed together to a separation distance of 4 mm. Data were collected in coincidence mode with scan step length 5 mm and duration 300 seconds/step. The scan was performed over 60 mm x 15 mm of the overlap region of the two detectors.

(c) A long count was recorded at one position with the collimator pointing at the centre of the planar. Detectors had a separation of 4 mm. Data were collected for four hours with acquisition in singles mode.

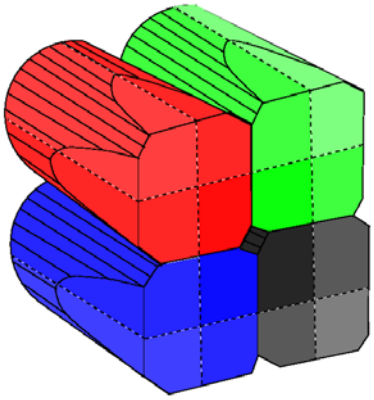

Figure 3.8: The EXOGAM Clover detector has four crystals that are each electrically segmented to have four outer contacts and one inner contact, making sixteen outer contacts and four inner contacts in total. The length of the crystals is 90 mm and the diameter of each crystal is 60 mm before shaping. The ends of the crystals have been tapered to allow close compacting with other similar detectors.

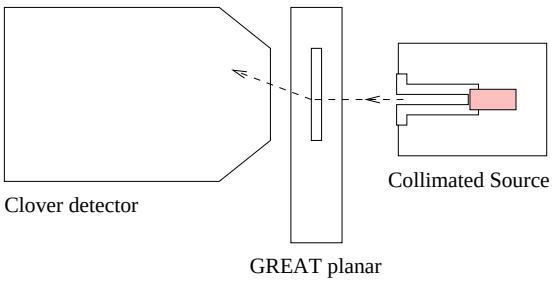

Figure 3.9: Experiment 5. Planar plus Clover basic configuration showing a photon entering the planar and scattering into the Clover. Distances between the two detectors and other specifics are indicated within the text for each separate experiment.

Experiment No.	**Source**	**Collimation**	**Step size**
1	Am-241 Co-57 Cs-137	none	none
2	Co-57	2 mm	2 mm
3	Co-57	1 mm	1 mm
4	Cs-137	2 mm at 63°	none
5a	Cs-137	5 mm	5 mm
5b	Cs-137	5 mm	5 mm
5c	Cs-137	5 mm	none

Table 3.1: Summary of experiments performed. Experiments 1 to 4 performed with the planar only, experiment 5 performed using both the planar and Clover detectors

Chapter 4

Detector Characteristics

This chapter reports the findings of the experimental measurements taken with the *GREAT* planar detector. It is concerned with the initial test data acquired using analogue and digital electronics and investigates the basic operational characteristics of the detector and its response to radiation events.

4.1 Operational characteristics

The successful operation of a detector relies on the knowledge of its performance qualities. Germanium detectors offer far superior energy resolution to scintillators, but their use comes at a cost of reduced efficiency. The energy resolution and efficiency of the *GREAT* planar detector are discussed in the following sections. An understanding of the depletion of the germanium crystal can be gained by examining the response of the detector to varying high voltage, the results of these tests are also presented here.

4.1.1 DC offset and measured noise

The DC offsets and noise were measured from the preamplifier outputs for each channel individually through a fast *HP Infinium* oscilloscope. The noise was measured peak-to-peak and had typical values of $\sim$5 mV. With the exception of boron(DC) 1, the DC offsets were typically $\lesssim$10 mV, and did not need to be corrected in later stages of acquisition. The DC offsets and noise for edge and centre strips can be seen in Table 4.1. The result for

all channels can be seen in Appendix A.

Contact	**DC offset (mV)**	**noise (mV)**
1	+100	5
12	+12	5
13	0	5
24	≤ -5	5
A	-5	3
F	+5	5
G	-8	5
L	-9	5

Table 4.1: DC offset and peak-to-peak noise measured from preamplifier outputs for edge and centre strips. Contacts 1-24 are the boron(DC) strips and contacts A-L are the lithium(AC) strips.

4.1.2 Preamplifier response

The preamplifiers were designed to give a gain of 500 mV/MeV when going into 1 MΩ. Post preamplifier signals were not amplified and typical amplitudes measured through the digital acquisition were ∼346 mV at 662 keV and ∼64 mV at 122 keV for the lithium(AC) strips and ∼456 mV at 662 keV and ∼82 mV at 122 keV for the boron(DC) strips.

The *GREAT* planar detector was supplied with two test inputs, lithium-(AC) B and boron(DC) 3, enabling the preamplifier response to be tested. The response was measured by injecting the test inputs with a pulse provided by a pulse generator supplying a step input with a height of 100 mV and a 5 ns leading edge. The pulse measured from the lithium(AC) B output had a magnitude of 270 mV and a rise time of 140 ns, measured between 10% and 90% of the pulse magnitude. The boron(DC) 3 output had a pulse of magnitude 325 mV and the rise time for this output was 341 ns. The decay time of the pulses was measured to be $40 \pm 2\,\mu$s.

The strips adjacent to those tested were observed for presence of crosstalk. Lithium(AC) C had a baseline difference of ~10 mV attributed to crosstalk. Boron(DC) 4 did not show any observable crosstalk. Section 4.2.3 will discuss crosstalk across all the strips.

4.1.3 Energy resolution measurements and noise evaluation

The energy resolution for the detector was found by measuring the FWHM from the photopeaks of several radioactive sources. Analogue electronics were used to measure the energy resolution of the detector at different energies. The sources used simultaneously were Am-241 and Co-57, giving photopeaks of energies 60 keV and 122 keV respectively. The detector output was amplified and shaped using a spectroscopy amplifier. The spectroscopy amplifier was set to Gaussian shaping mode with a time constant of 3 μs. The detector is susceptible to microphonics, therefore baseline restore was set to high. A sample of the analogue energy resolution results can be seen in Table 4.2, and the full results can be seen in Appendix A. The analogue resolutions were measured by connecting one channel at a time. On one of the boron(DC) edge strips (24) a poorer resolution was observed, all other strips on this contact have resolutions between ~1.5 keV to ~1.8 keV at energies of 60 and 122 keV. It should be noted that energy resolutions at 60 keV are higher than those at 122 keV for this contact, the reason for this is unknown. The inner lithium(AC) strips have resolutions between ~1.4 keV and ~1.8 keV, and on this contact the two edge strips A and L have poorer resolutions of ~2.0 keV and ~2.2 keV at 60 and 122 keV. The electric field is weak near the edges of the detector affecting the charge collection and hence the energy resolution in these regions.

The resolutions of the data acquired using the digital system also include Cs-137 with its 662 keV photopeak. A sample of the results can be seen in Table 4.3, and full results can be seen in Appendix A. Resolutions were measured with all channels connected and in oscilloscope mode with no attempt to use algorithms to improve the resolution using the digital system. Several of the boron(DC) strips show double peaking, producing poor resolutions for the 662 keV peak. All peaks in spectra collected in strips on this side of

	60 keV		122 keV	
Contact	**FWHM (keV)**	**FWTM (keV)**	**FWHM (keV)**	**FWTM (keV)**
1	1.73	5.97	1.64	4.36
12	1.75	3.83	1.68	3.38
13	1.76	3.90	1.65	3.55
24	2.17	5.03	2.05	4.92
A	2.02	4.05	2.09	3.98
F	1.56	2.94	1.70	2.96
G	1.58	3.09	1.67	3.14
L	2.22	4.15	2.24	4.13

Table 4.2: Analogue energy resolution results at 60 and 122 keV for edge and centre strips. Contacts 1-24 are the boron(DC) strips and contacts A-L are the lithium(AC) strips.

the detector suffer low energy tailing, and resolutions are between ~4.5 keV to ~5.2 keV taken at energies of 60 and 122 keV. The lithium(AC) contacts have a slight improvement in the strip resolutions of ~3.7 keV to ~4.5 keV taken at energies of 60 and 122 keV. The peaks in spectra from this contact also show low energy tailing.

Energy resolution results for both analogue and digitally acquired data are displayed in Figure 4.1. The degradation in energy resolution from analogue to digital electronics is severe. This is partly due to the baseline difference method used to measure the height of a pulse. The maximum height of a pulse is calculated by averaging the samples at the pulse top, but this includes using samples that are part of the decaying pulse. The decay of the pulse can be removed with the implementation of an algorithm, for example, moving window deconvolution.

A noise pulse taken from the digital data has been examined, the pulse is shown in Figure 4.2. The peak-to-peak noise voltage is measured to be 10.5 keV, giving an RMS noise voltage of 3.7 keV assuming a sine wave.

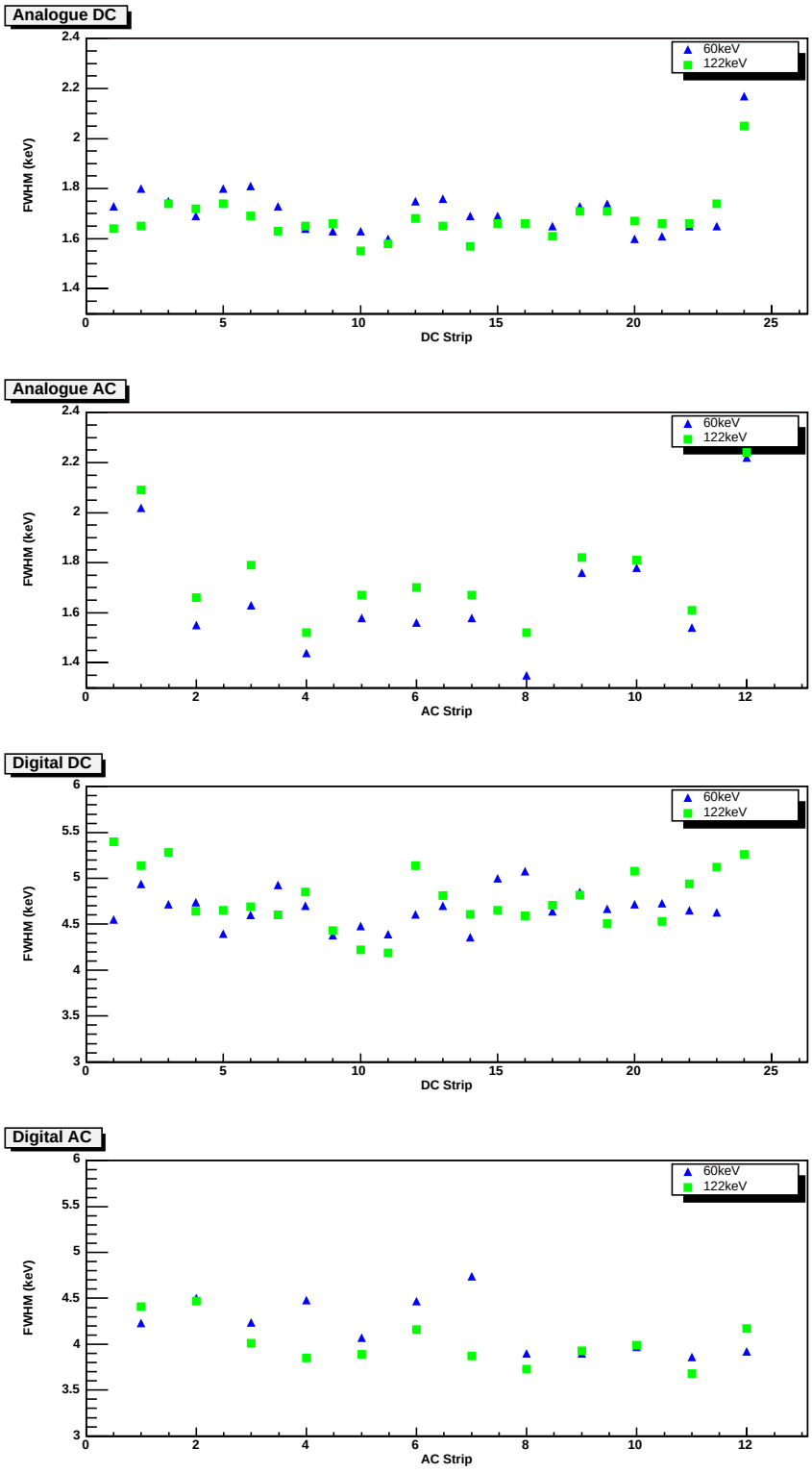

Figure 4.1: Energy resolutions at 60 and 122 keV for analogue and digital acquisition. Lithium(AC) strips A to L are numbered 1 to 12 here.

	60 keV	**122 keV**	**662 keV**
Contact	**FWHM (keV)**	**FWHM (keV)**	**FWHM (keV)**
1	4.55	5.40	6.4
12	4.61	5.14	7.21
13	4.70	4.81	7.46
24	5.73	5.26	6.54
A	4.23	4.41	4.63
F	4.47	4.16	5.75
G	4.74	3.87	4.89
L	3.92	4.17	5.23

Table 4.3: Digital energy resolutions at 60, 122 and 662 keV for edge and centre strips. Contacts 1-24 are the boron(DC) strips and contacts A-L are the lithium(AC) strips.

Some of the contributions to the noise have been estimated by the methods discussed in Section 2.4.3. The best achievable FWHM due to the fluctuation of charge carriers, W_D, has been calculated to be 0.4 keV at 122 keV. An estimate of the contribution from charge collection inefficiencies, W_X, has been made by varying the high voltage above full depletion voltage and measuring the FWHM of a chosen channel at each high voltage. The inverse of the high voltage has been plotted against the FWHM and the fit has been extrapolated back to an infinitely high voltage as shown in Figure 4.3. From this, at the operating voltage, W_X is estimated to be 1.0 keV on the lithium(AC) contact and 0.9 keV on the boron(DC) contact, both at 122 keV. The FWHM at infinitely high voltage is estimated to be 3.0 keV at 122 keV for the lithium(AC) contact, and 4.1 keV at 122 keV for the boron(DC) contact. These come from the remaining contributions to the observed FWHM. The remaining contributions to the FWHM include W_E from noise, and peak broadening due to the method of pulse height calculation.

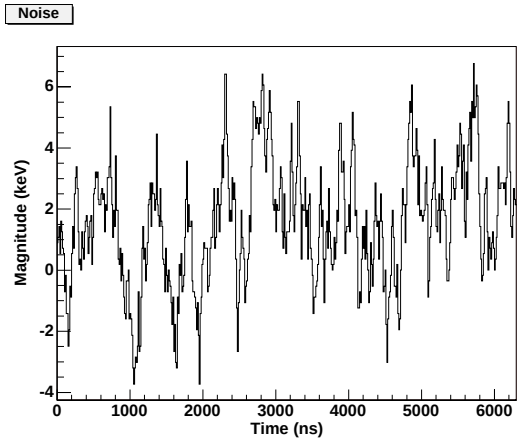

Figure 4.2: Noise pulse from a typical boron(DC) strip

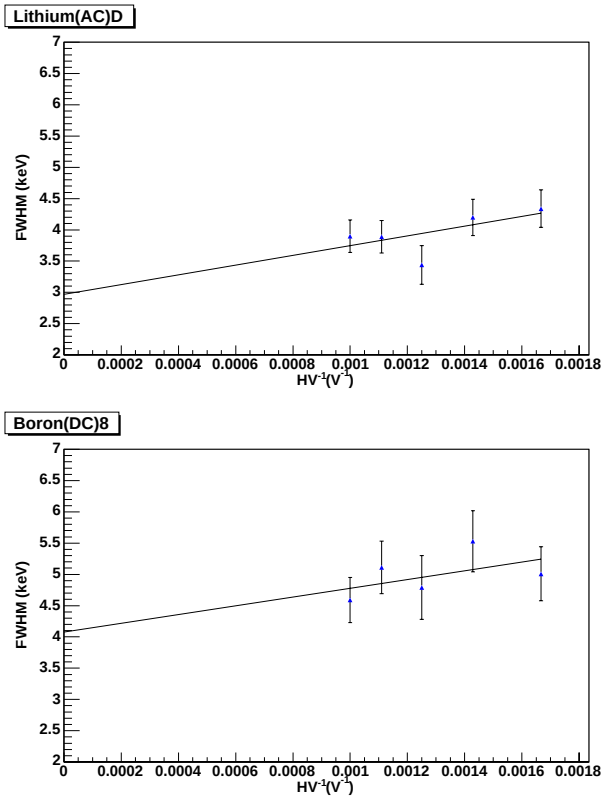

Figure 4.3: Charge collection noise contributions

4.1.4 Efficiency measurements

The absolute efficiency of the planar detector has been found for both the boron(DC) and lithium(AC) contacts. The source used was a 27 kBq barium-133 source, placed at a distance of 149 mm from the centre of each of the crystal faces [Her05]. The lithium(AC) contact is 0.7 mm thick and produces a tail-off in efficiency below ~80 keV due to absorption in the contact of the lower energy photons. In contrast, the boron(DC) contact is a $0.3\text{x}10^{-3}$ mm thin contact and has a efficiency plateau below ~50 keV. The absolute efficiencies can be seen in Figure 4.4.

4.1.5 Detector response to varying high voltage

The high voltage of the detector was varied from 200 V through the full depletion voltage of 600 V, to an over-operational bias (by +200 V) of 1000 V. The energy recorded on a strip on one side of the detector compared with that recorded on the opposite side has been investigated to gain an understanding of the depletion in different regions of the detector. The only events considered are fold 1 events, i.e. only one strip on each side of the detector has fired and collected a real energy.

The ratios of energies collected can be seen in Figure 4.5. As the high voltage is increased, the depletion region extends from the boron(DC) contact. The impurity concentration difference across the crystal also affects the depletion region. The depletion depth is at a maximum in the regions with the least impurity concentration. The impurity concentration ranges from 5 x 10^{+9} cm^{-3} at boron(DC) 1, to 1 x 10^{+9} cm^{-3} at boron(DC) 24. At 200 V the boron(DC) plot shows double the energy being collected on the boron(DC) centre strips to the lithium(AC) contact. Also on the boron(DC) plot, neglecting the edges, the effect of the impurity concentration difference across the crystal is observable at 200 V. The lower concentration end of the detector being depleted more has more energy collected on the lithium(AC) contact than the higher concentration end, and this is shown as a decrease in DC/AC ratio. As the high voltage is increased and the depletion region extends more into the depth of the crystal, more charge is being collected by

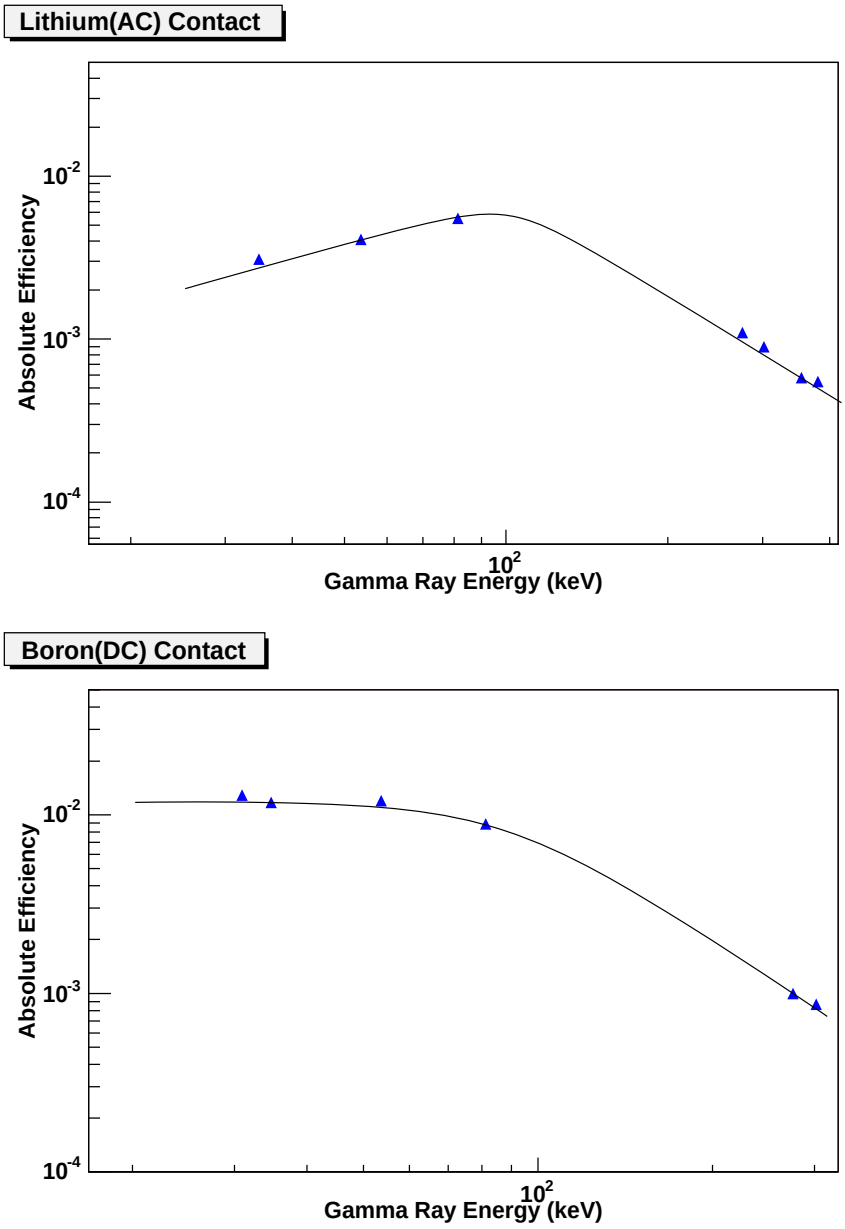

Figure 4.4: Top: Efficiency of lithium(AC) contact. Bottom: Efficiency of boron(DC) contact. Fits have not been made to the efficiencies, but lines have been added to guide the eye.

the lithium(AC) contact and the ratio approaches one. The edge strips on both contacts of the detector show weak field regions, with the boron(DC) edge strips collecting up to three times more charge than the lithium(AC) contact.

4.2 Detector response to radiation events

Calibrating the detector volume starts with the investigation of any differences in fold between the two planar contacts. Once this has been established any minor differences in the crystal or individual strip collection can be ascertained by examining the intensity per position from a controlled scan of the surface of the detector. Also included in this section are crosstalk calculations and an investigation of observed energy losses within the detector.

4.2.1 Fold

The fold discussed here is defined as the number of readout strips that fire in coincidence on one contact, whether it be lithium(AC) or boron(DC). Fold histograms for the two contacts are shown in Figure 4.6. They were incremented each time real interactions[1] were responsible for triggering the acquisition and show the highest fold frequency within this detector is fold 1 (from experiment 3 data). The mean free paths for Compton scattering of 122 keV and 662 keV gamma rays are 1.3 cm and 2.4 cm respectively. For this work fold 1 full energy events are considered as photoelectric interactions or Compton scatters followed by photoelectric interactions, depositing full energy within a 5 mm strip. Fold 2 events are considered to be interactions that have Compton scattered at least once before photoelectric absorption, and are collected by two neighbouring strips. Only data from folds 1 and 2 are presented, to exclude the necessity of considering gamma-ray tracking which is beyond the scope of this work.

[1] An algorithm determines whether a pulse is bad, real energy or a transient. Real energies are those that have a baseline difference greater than three standard deviations of the noise. The method of extracting transients from the noise is described in Section 5.2.3.

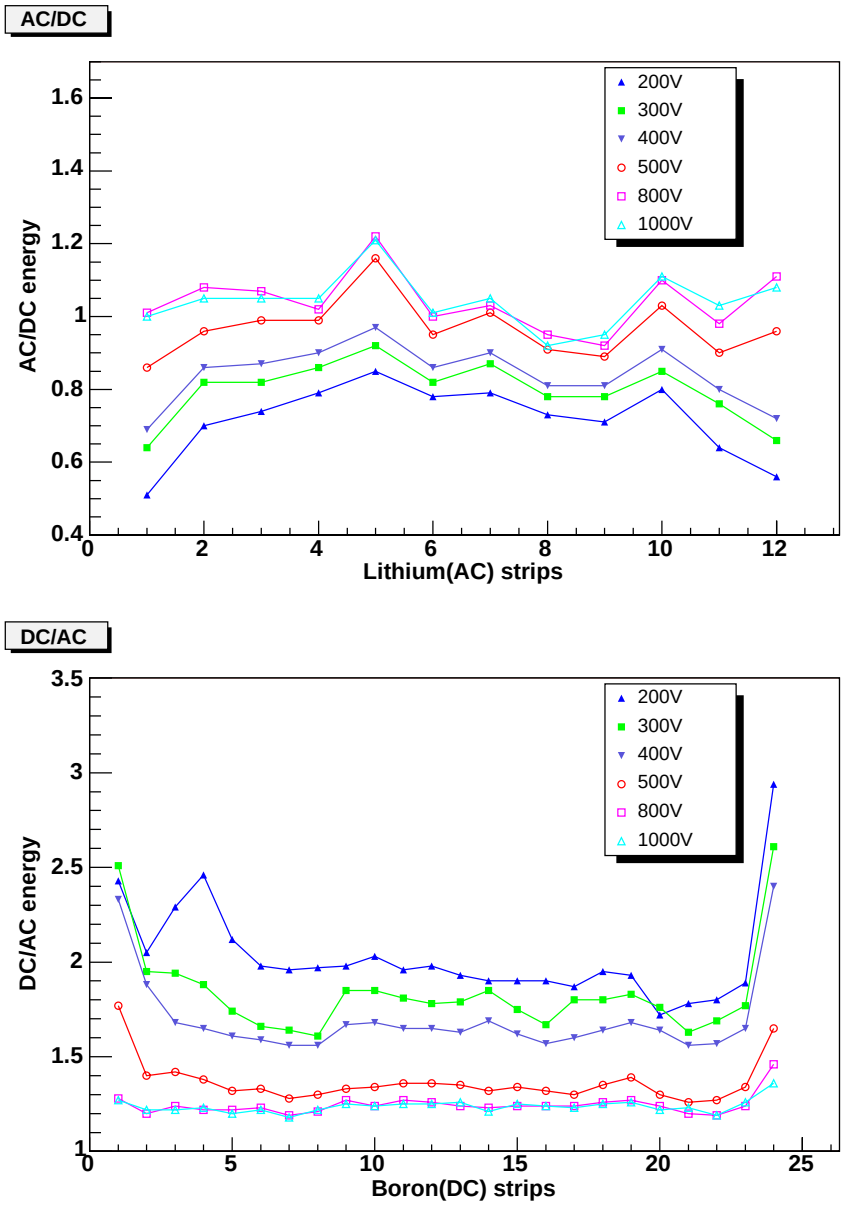

Figure 4.5: Energy collected on strips shown as a ratio with the energy collected on the opposite contact for various values of high voltage. Uncertainties are small, $\sim 2\%$, and are the statistical error associated with energy collection. Lithium(AC) strips A to L are numbered 1 to 12 here.

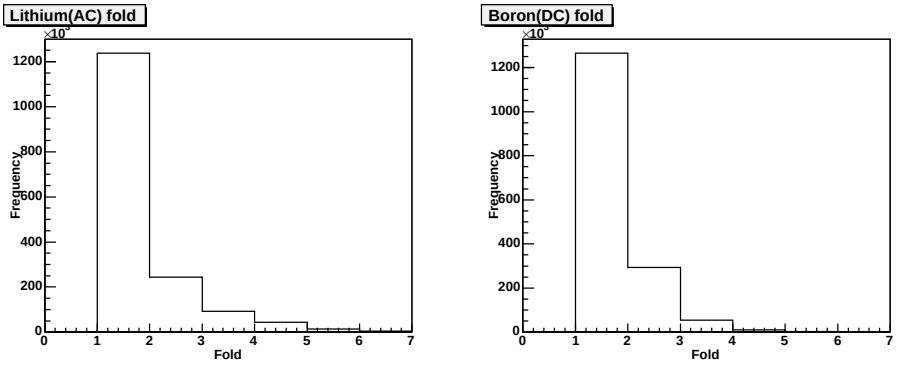

Figure 4.6: The strip fold for each contact from uncollimated data (experiment1)

4.2.2 Intensity per position

The sensitivity of the detector to radiation events is investigated by recording the number of events at each of the coarse scan positions across the detector surface (experiment 2 - 2mm collimator, 2mm steps, Co-57 source). Differences in intensity are a combination of crystal abnormalities and inefficient charge collection. As the number of counts recorded are per position, even when the collimator is positioned away from the crystal surface a background is being collected by the detector from environmental radiation and from bad collimation/poor shielding. The contrast between the collimator being positioned in the background and on the crystal is visible on Figure 4.7. This is useful for synchronizing position information with the edge of the crystal. No energy restrictions were placed on the intensity/position map shown in Figure 4.7 (a). The acquisition was set to trigger on any interaction occurring above noise, resulting in high background rates. Detection rates here are ∼75 counts/second for the background and ∼80 counts/second within the crystal area.

The response of the detector to 122 keV full energy gamma rays can be seen in Figure 4.7 (b) and (c). The collimator used for this scan was 2 mm diameter and no demands have been made on the fold. This produces an odd looking intensity profile for the lithium(AC) contact due to the collimator

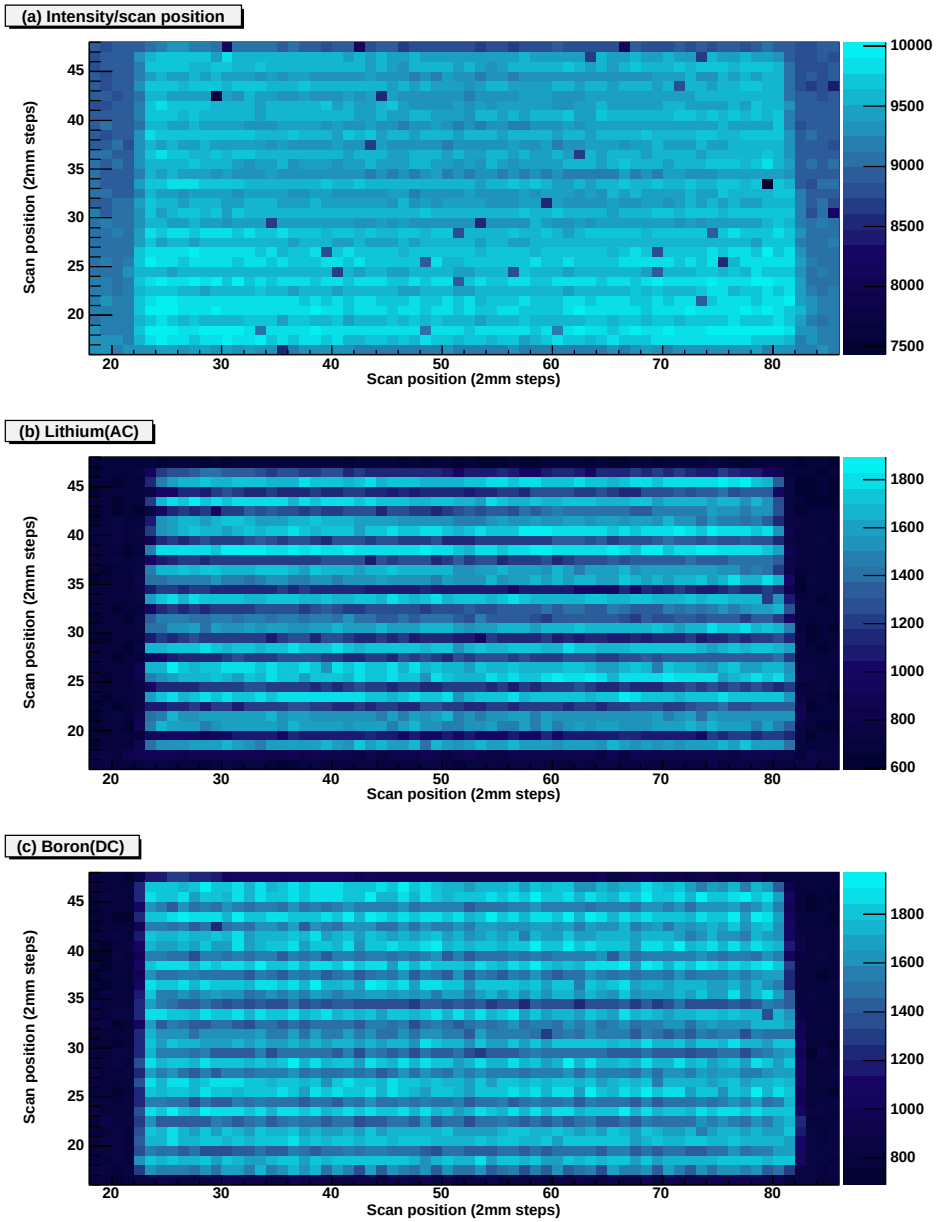

Figure 4.7: (a) Intensity of detected gamma rays at each scan position, for any energy and all contacts. (b) Intensity of detected 122 keV gamma rays per scan position, on the lithium(AC) contact. (c) Intensity of detected 122 keV gamma rays per scan position, on the boron(DC) contact.

glancing over the large inter-strip distances of 0.7 mm. The background has been reduced to 7 counts/second and 15 counts/second within the crystal area, giving a ratio of 2:1 for events detected with the collimator positioned in front of the crystal and those where it is positioned away from it. The intensity profile on the boron(DC) contact shows the strips on this contact are also not visible. It is not possible to resolve the strips while using this collimator.

The fine scan (experiment3) used a 1 mm collimator with 1 mm steps in a raster pattern. The scan was only performed over a small area of the detector because of the difficulties encountered in scanning this detector. One of the 1 mm raster lines scanned was positioned over the centre of a lithium(AC) strip (strip G). This strip is in the centre of the detector and should not have the electric field problems encountered near the edge of the crystal and as such, this region is considered a representative of the detector. The 1 mm line scan passed across all 24 of the boron(DC) strips.

From the line scan, the intensity/position for 122 keV fold 1 events collected on one of the boron(DC) strips (7) has been plotted in Figure 4.8. The plot is a good illustration of the background collected on a strip while the collimated source is not pointing at that strip and shows clearly the increase in intensity as the collimator passes in front of the strip. To compare the intensity across all of the boron(DC) strips, the background on each strip has been averaged and removed. An integral of the background-removed intensity profile for each strip has been calculated and plotted in Figure 4.9 and shows a slight decrease in integrated counts from boron(DC) 1 to 24.

Losses due to charge collection become apparent when the energy measured on one contact is plotted against the energy measured on the other contact. If all charge is collected on both contacts for all energies, there should be a linear relationship between the two with a gradient of 1. Figure 4.10 depicts fold 1 energies plotted for interactions during the coarse scan (experiment2). The coincident energies collected show a gradient of 1, but some coincidences are to the left of the expected linear relationship

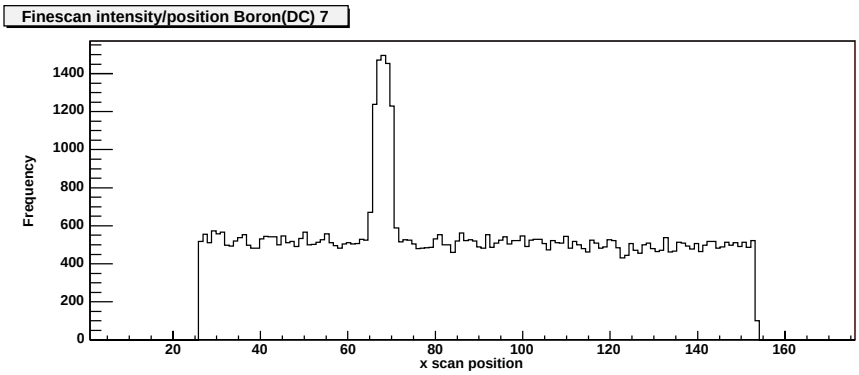

Figure 4.8: Intensity per fine scan position on boron(DC) 7.

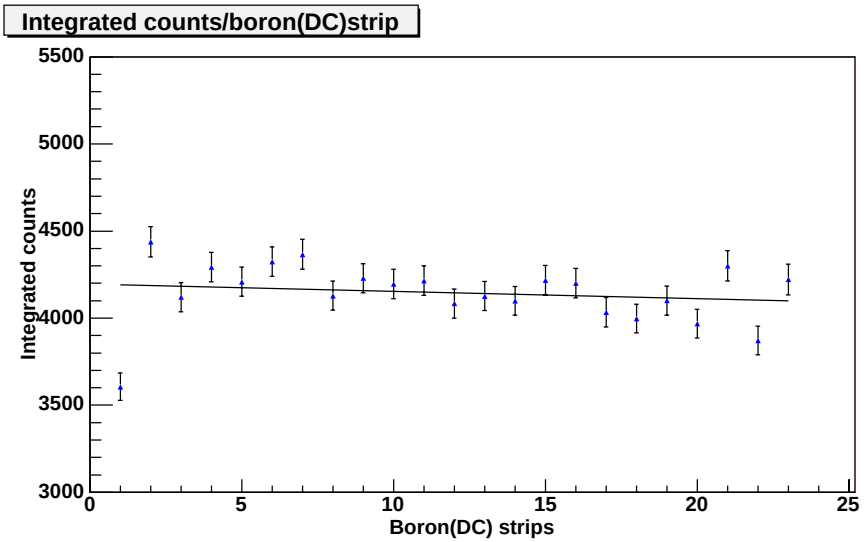

Figure 4.9: Integral of counts in each boron(DC) strip from a 1 mm collimated , 1 mm run across the detector face. A linear fit has been added giving a gradient of -12 ±3 counts/strip or a 2.5% drop in intensity from strip 1 to 24.

showing charge losses on the boron(DC) contact.

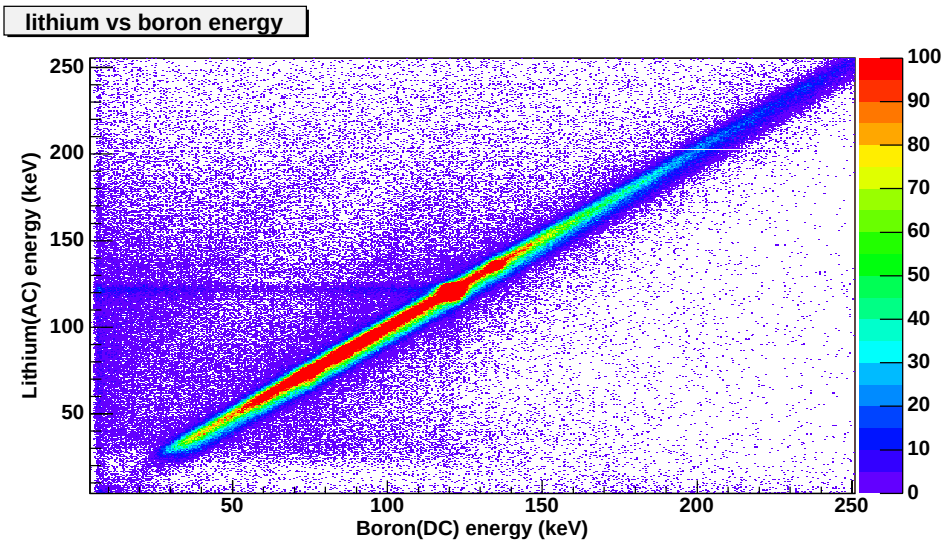

Figure 4.10: The energy measured on one contact compared with that collected on the opposite contact.

4.2.3 Crosstalk

As mentioned in Section 2.4.1, crosstalk is the undesired capacitive, inductive or conductive coupling from one circuit, part of a circuit, or channel, to another. The effects of crosstalk appear as a baseline shift on the signals that adds or subtracts from any energy collected. This can be observed using the add-back technique. In this work add back refers to the energy from fold 2 events, two strips fired and collected an energy, added together to regain useful information from scattered events. The fold 2 events considered here are adjacent strips firing and non-adjacent strips firing (Figure 4.11). For the non-adjacent strips, only next-but-one neighbours are considered for both 122 keV and 662 keV gamma rays. This is because of the short mean distance the scattered 122 keV gamma rays are expected to travel in germanium (the greatest distance travelled after the first Compton event will follow a small energy deposited) and to be consistent between the analysis of the two energies of interest.

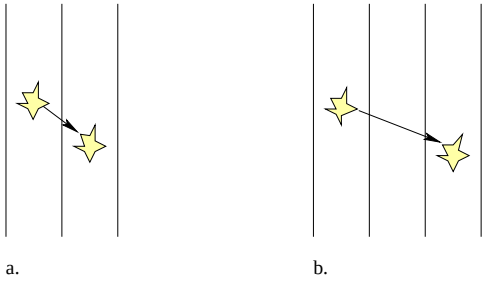

Figure 4.11: Fold 2 events with interactions in (a) adjacent (neighbouring strips) and (b) non-adjacent (next-but-one neighbours only) strips.

Three spectra are compared in Figure 4.12 for each contact, focusing on the 662 keV photopeak. The three spectra being compared are from the uncollimated data (experiment1 - Am-241, Co-57 and Cs-137) and are: an ungated singles spectrum summed for all strips on each contact (all); energies from any two adjacent strips added (662adj), only fold 2 events whose sum falls in an energy window (gate) of 654 keV to 668 keV are included; and energies added from any non-adjacent strips (662nonadj), also fold 2 with same 662 keV energy gate.

The boron(DC) adjacent add-back spectrum shows a positive shift in the 662 keV peak. This peak shift is not apparent in the non-adjacent add-back spectrum and so it can be concluded that the shift was due to crosstalk. The peak shift shown is 0.5% on the 662 keV peak and has been measured for all strips individually with a range of 0.3% to 1.9% on the 662 keV peak being observed. The lithium(AC) adjacent add-back spectrum shows a double peak, with one peak at 662 keV and the other at 672 keV. Even though the spectrum shown is a sum of all adjacent add-back events, the double peaking is observed on individual strip add backs between a number of the lithium(AC) strips. As crosstalk is not expected to be an intermittent problem, the individual energies being added were plotted for both adjacent add-back peaks. This shows that the higher energy peak is an addition of 662 keV and 10 keV energies and therefore the higher energy peak is not considered for the crosstalk calculation. Excluding the higher peak, there is no observ-

able crosstalk on the lithium(AC) strips. It was reported in Section 4.1.2 that crosstalk was observed on a lithium(AC) strip and not on a boron(DC) strip after a pulse was injected into the preamplifiers, this is the opposite to the results here. Different crosstalk from different parts of the detection system can add to give the two contradicting results. [Kro95a] showed a larger crosstalk occurring as a result of coupling between strips of smaller interstrip distances. The crosstalk observed in the spectra but not in the pulsar measurements are likely to have come from coupling between the strips. This would explain why a coupling is observed between the boron(DC) strips of small interstrip distance and not between the lithium(AC) strips of large interstrip distances.

4.2.4 Energy losses

The two energies added together in fold 2 adjacent add-back and non-adjacent add-back spectra have been plotted against each other as gamma/gamma energy matrices shown in Figure 4.13. Energies that add back to the photopeak energies are seen as diagonal lines between the 60 keV, 122 keV and 662 keV energies. The plots show energy losses in the lithium(AC) adjacent matrix, seen as arcs below the main diagonals. These are not present in the lithium(AC) non-adjacent matrix or in either of the boron(DC) matrices. To investigate how these energy losses affect the lithium(AC) adjacent add-back spectrum, gamma/gamma energy selections (polygates) have been made on all the matrices for comparison, and the two energies then added together and plotted as spectra. Two examples of the polygates are shown in Figure 4.14 on the lithium(AC) adjacent matrix around the 122 keV line and its associated energy loss arc. The spectra resulting from all polygates around the photopeak lines and the energy loss regions can be seen in Figure 4.15, and are plotted with ungated fold 2 adjacent add-back spectra for comparison. The polygates around the energy loss regions are seen to compare with the tails to the lithium(AC) ungated add-back spectra. It should be noted that even though the boron(DC) ungated add-back spectrum shows low energy tailing on the photopeaks, they are not evident as energy losses in the gamma/gamma matrices. It can be concluded that the tailing on

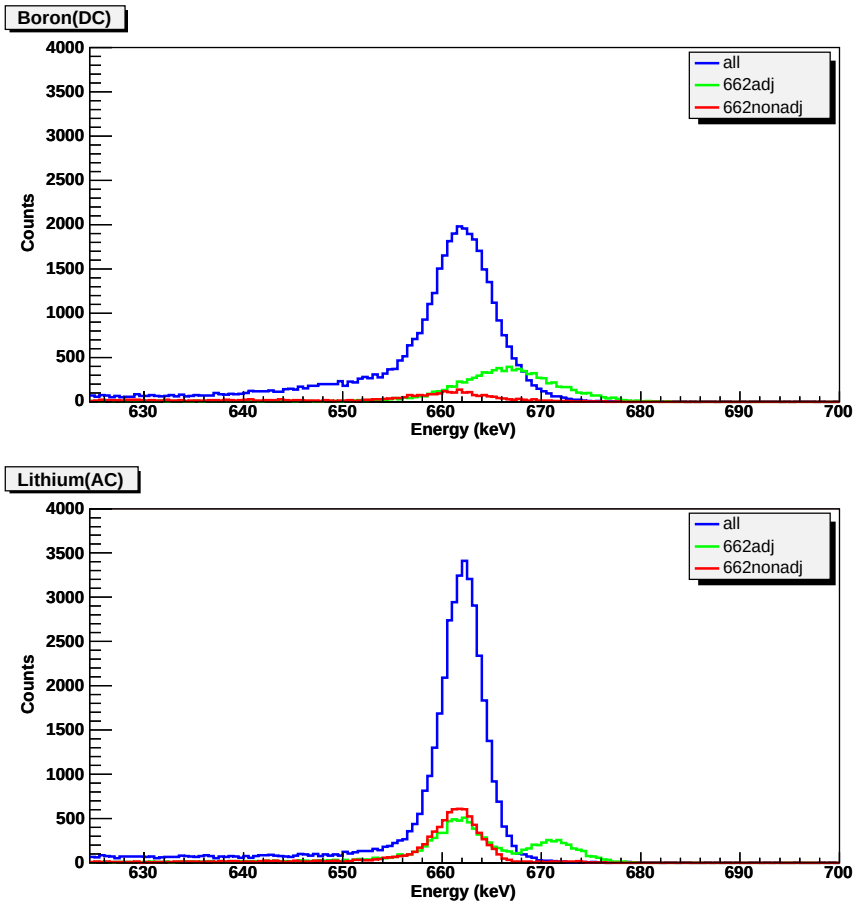

Figure 4.12: Ungated (all), adjacent add-back (662adj) and non-adjacent add-back spectra for the boron(DC) and lithium(AC) contacts.

the boron(DC) peaks is a different effect to the tailing on the lithium(AC) peaks. Charges collecting for events between two strips can either be collected completely on one of the strips or charge can be shared between the two strips or charges can be collected at the surface between the two strips. It can be speculated that the large interstrip distances on the lithium(AC) contact could be contributing to charges collecting at the surface between two strips, resulting in the energy losses seen in adjacent add-back spectra. It can also be speculated that the tailing on the boron(DC) add-back photopeaks is due to poor charge collection of holes.

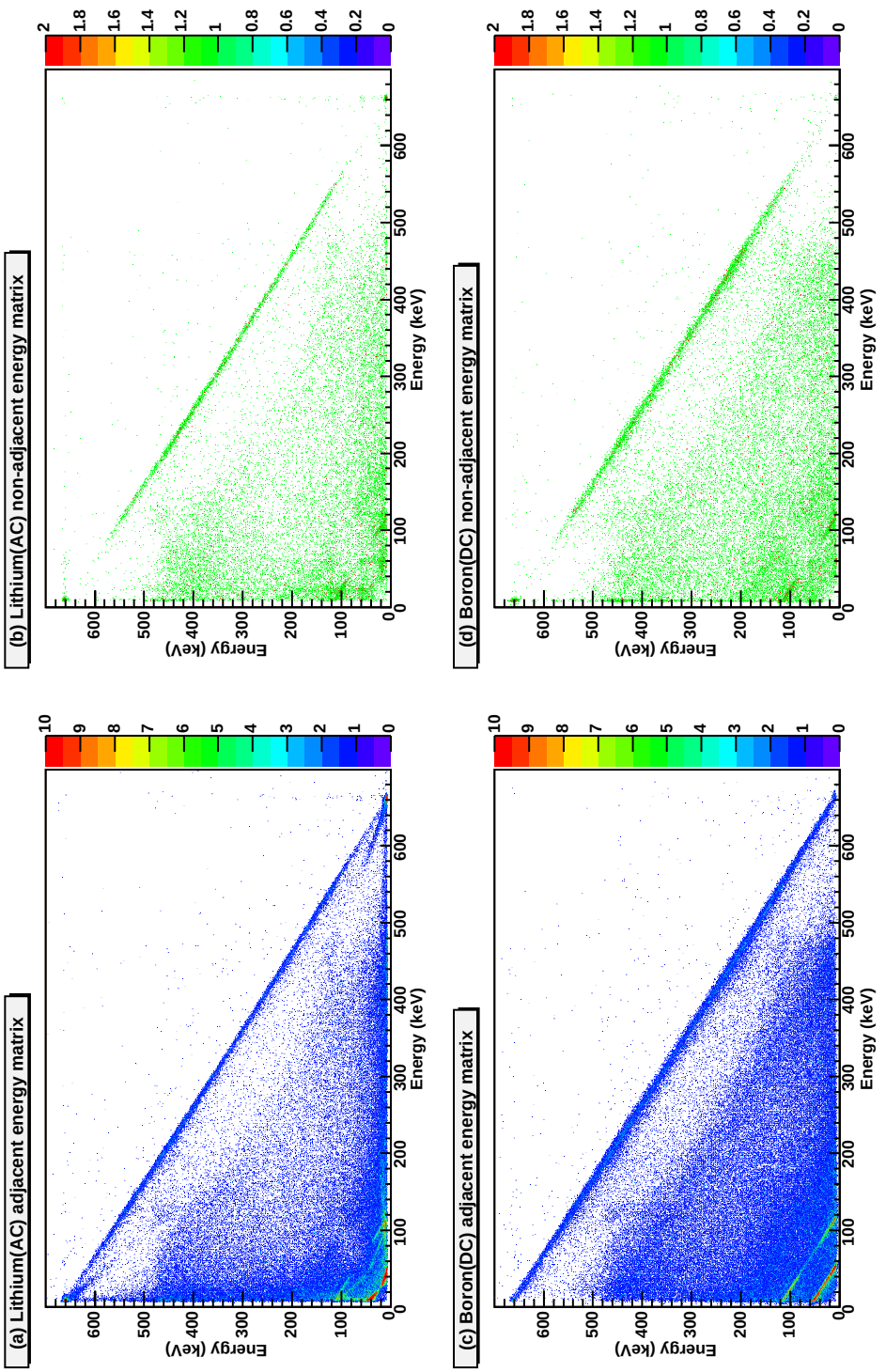

Figure 4.13: Fold 2 energy matrices showing energies, if added together, would sum to 60 keV, 122 keV and 662 keV. These are visible as diagonal lines across the plots.

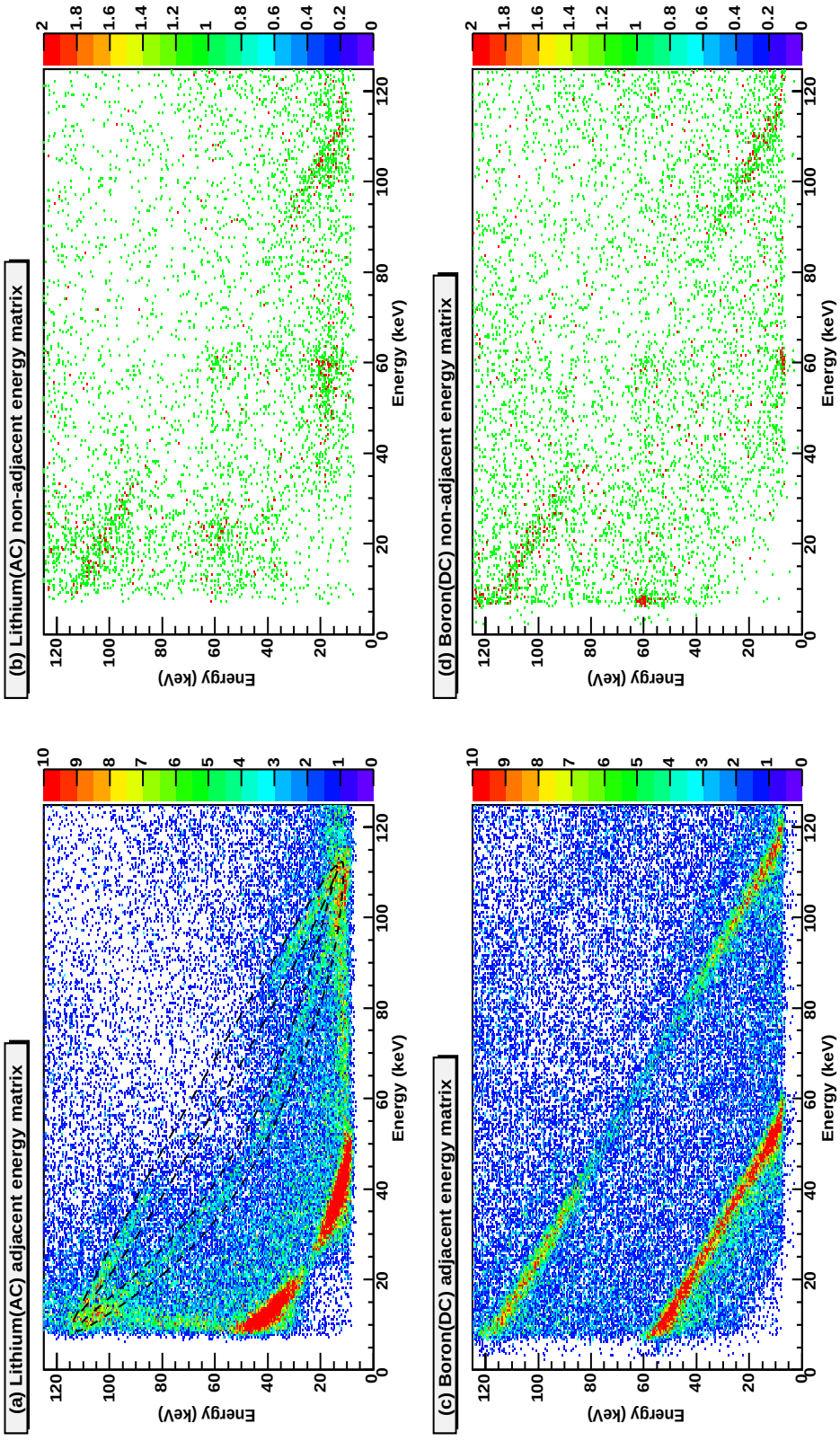

Figure 4.14: Energy matrices zoomed around the lower energy region; showing 60 keV and 122 keV fold 2 events. Examples of selections made are shown on the lithium(AC) adjacent fold 2 matrix.

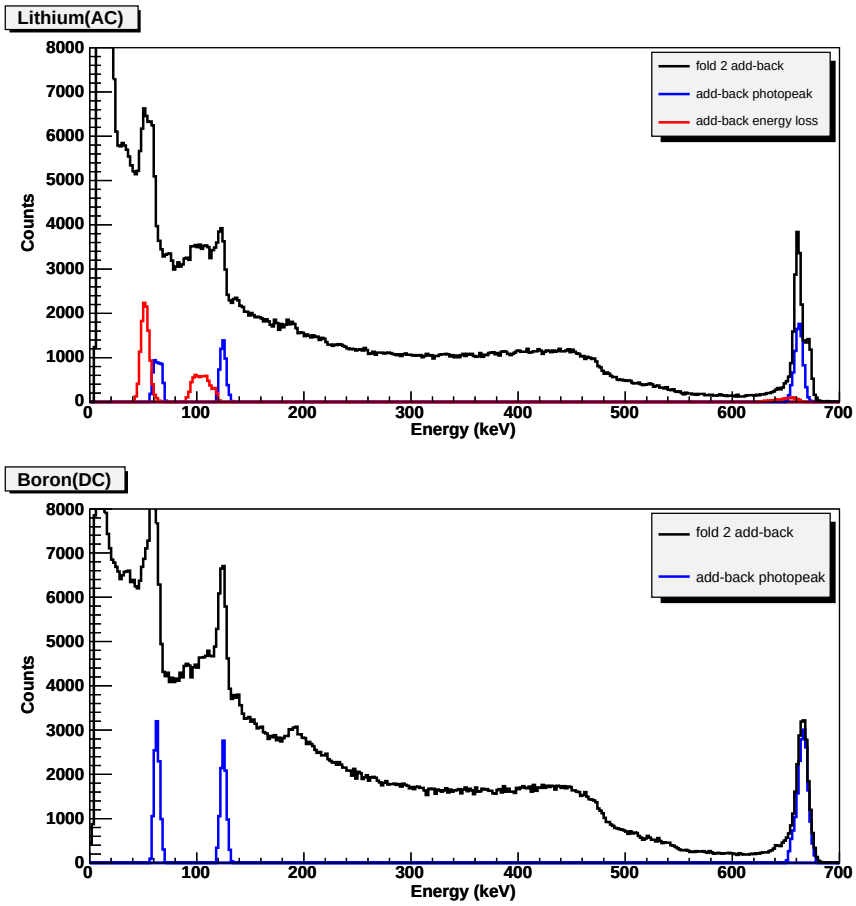

Figure 4.15: Fold 2 adjacent add-back spectra summed for all channels on each contact. Added to the spectra are the resulting peaks from polygate selections made on the energy matrices (Figure 4.13). Selections for the lithium(AC) matrix are cut around the adjacent added-back photopeaks (60 keV, 122 keV, 662 keV) and the adjacent energy loss regions as shown in Figure 4.14. The energy loss regions can be seen as tails to the photopeaks. For the boron(DC) contact selections have been made from the adjacent added-back photopeaks only.

Chapter 5

Pulse Shape Analysis

Analogue pulse shape analysers are widely available for uses such as discriminating between pulses from different types of radiation, for example, the difference between neutrons and gamma rays detected by some scintillators. They are also used for determining the position of interaction in position-sensitive proportional counters. The advances in digital electronics allow pulse shape analysis techniques to be refined and used more widely with other types of detectors. As a result of digitization, pulses can now be analysed in part or full, online or offline, and pulses can even be parameterized.

The use of pulse shape analysis in this work has been to improve the position sensitivity of the detector beyond its physical and contact segmentation. This has been attempted by extracting a number of parameters from the pulses in addition to energy and using them to determine x, y, and z interaction position.

This chapter discusses the principles behind pulses shape analysis as a method of interaction position determination in a planar detector geometry. The application of these principles to the *GREAT* planar detector is presented along with any operational characteristics observed in the rise time analysis.

5.1 Pulse shape analysis concepts

There are two basic types of pulses observed following an interaction, a real charge where a net charge is collected, and a transient charge where a neighbouring strip will sense the movement of charges and produce a small pulse that has no net charge (Section 2.3.3, Figure 2.8). The two types of pulse vary in shape with varying interaction position. Pulse shape analysis attempts to use these properties to extract interaction position information that is superior to that of the detector segmentation alone. The following sections will outline the reasoning for using these pulses for interaction position information.

5.1.1 Rise time

When a radiation event occurs in the detector, electron-hole pairs are created and mobilized by the electric field. In a segmented planar detector, these electron-hole pairs drift under the influence of the electric field towards the opposite segmented contacts (strips). The induced real charges on the strips are a result of all the moving charges within the detector volume. Depending upon the depth of interaction, the holes and electrons moving in opposite directions will have different distances to travel to their respective contacts and this results in a position dependent pulse shape. This is demonstrated for a planar detector geometry in Figure 5.1.

Another factor affecting the pulse shapes is the small electrode effect as shown in Figure 5.2. For detectors like the *GREAT* planar, whose strip width and pitch are small compared to their thickness, the weighting field can drop by a factor of two at a distance that is comparable to the strip width [Ham96]. For strips of width 5 mm it can be said that the weighting field is high up to a distance of 5 mm away and low beyond this. In a strip or pixel detector, the large differences in the weighting field through the depth can change the shape of the time dependent charge pulse. Charges moving outside the high weighting field region induce a much smaller charge than those moving within the high region, and therefore charges induced on a sensing strip will be small until the charge it is collecting arrives in the

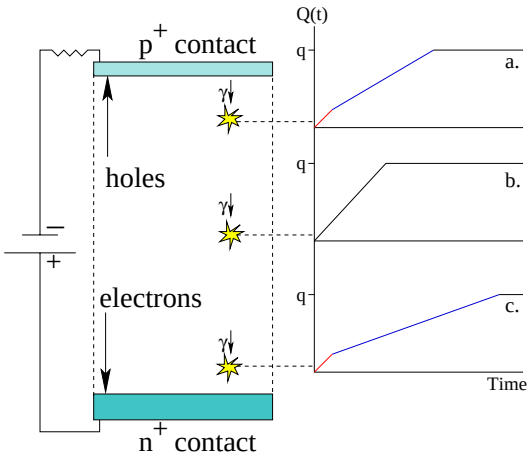

Figure 5.1: The variation of the leading edge of a charge pulse in the p^+ contact, for three interaction depths in a planar germanium detector. (a) the holes have a short distance to travel and the charge pulse shape is dominated by the electron collection time. (b) holes and electrons have the same distance to travel, pulse shape is not dominated by either. (c) the electrons have a short distance to travel and the charge pulse shape is dominated by the longer hole collection time.

immediate vicinity. This is observable in the charge pulse shape as a very slow-rising start for interactions outside of the high weighting field region. The small electrode effect produces a difference in time response on the opposite sensing strips, which can possibly be used to measure the depth of interaction.

The different shaped pulses can be distinguished from one another by means of a number of parameters, T30, T60 and T90. These parameters are the time the charge pulse takes to get from 10% to a larger percentage of its full height, 30%, 60% and 90%. They are known as rise times, the parameters are shown in Figure 5.3.

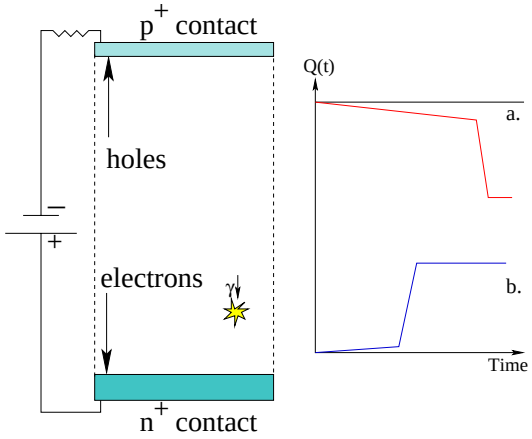

Figure 5.2: The small electrode effect. (a) signal from boron(DC) is dominated by hole movement in the immediate strip vicinity. (b) signal from lithium(AC) is dominated by electron movement in its immediate strip vicinity.

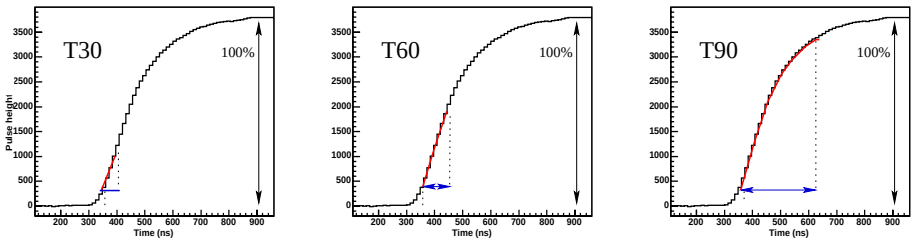

Figure 5.3: The parameters used to compare pulse shapes. They are the time it takes for the charge pulse to reach a % of its maximum height. T30 is the time from 10% to 30% of pulse height, T60 is 10% to 60% and T90 is 10% to 90%.

5.1.2 Transient charges

Transient signals, also called spectator or image charges, are induced by moving charges in a similar manner to real charges, but they occur on neighbouring electrodes/strips to those collecting real charge. As shown in Figure 2.8, a transient pulse is produced in a strip by a charge moving through the extended weighting field of that strip. As no charge collection is occur-

ring on this strip, there is a net charge of zero. In a planar detector, the interaction depth changes the shape of the transient charge. Interactions at different depths result in the opposite sign charges moving through different distances and different intensities of the weighting field. The strip sensing the moving charges senses the movement of both sign charge carriers and subsequently the shape of the transient signal is produced by all moving charges. An example of a real charge in one strip and transients in the adjacent strips is shown in Figure 5.4.

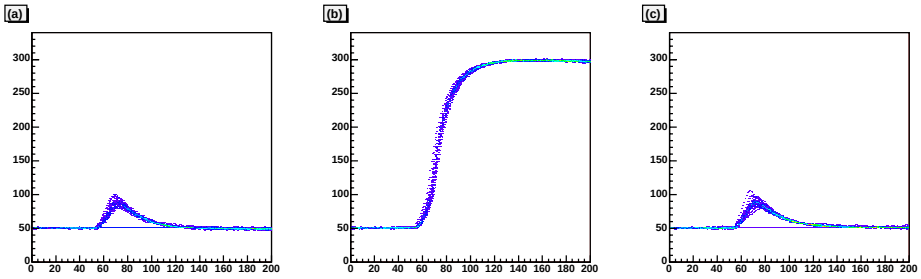

Figure 5.4: The real charge pulse of a 662 keV gamma-ray interaction, (b) , and the transients observed in the two adjacent strips, (a) and (c), are shown. Units for charge and time are arbitrary.

For the *GREAT* planar detector, the size of a transient observed in a strip next to the one collecting real charge is typically less than 20% of the real charge pulse height. Transient heights depend on their lateral distance away from the real charge collection. The height of a transient will be at its largest when the interaction is close in lateral position to that strip. Measuring the height of transients in neighbouring strips can give extra position information within a strip, leading to a lateral spatial resolution beyond the width of the strips. This has been achieved by [Des02], who uses an asymmetry term, $A_{m,n}$, to quantify the differences in transients in both adjacent electrodes, adjacent strips for the planar detector.

$$A_{m,n} = \frac{Q_m - Q_n}{Q_m + Q_n} \tag{5.1}$$

Q_m and Q_n are the maximum heights of the transients on the adjacent strips to the real charge collection.

5.2 Pulse shape analysis of the *GREAT* planar detector

Data from the scans are used to calibrate pulse shapes as a function of interaction position. The general response of the detector volume is presented along with attempts to determine interaction depth from variations in pulse shapes and to determine interaction position beyond strip width (a direction perpendicular to depth) using transient charges. Where possible, experimental data have been compared with simulation data. The simulation package used was developed at the Institut de Recherche Subatomique (IReS), Strasbourg, France. A description of the package has been included in Appendix B.

5.2.1 Rise time distributions

Before any pulse shape analysis was performed, an average rise time per scan position was determined to show any basic differences across the crystal or between strips' electronics. It is expected that the rise time varies with impurity concentration; mobility reaches a maximum at lower impurity concentrations. There are two main mechanisms that slow charge drift velocity [Sze02b], lattice scattering and impurity scattering. Thermal vibrations in the lattice allow energy to be transferred between the carriers and the lattice, resulting in lattice scattering. Lattice scattering will be constant for constant temperature and the effects should not be seen while the crystal is kept at liquid nitrogen temperature. Ionized impurity atoms deflect charge carriers by the Coulomb force. This is called impurity scattering and the probability of it occurring increases with increasing impurity concentration. Hence, drift velocity decreases with increasing impurity concentration for a constant temperature.

The rise time parameters T30, T60 and T90 have been plotted for the coarse scan data (experiment 2: Co-57, 2mm collimator, 2mm steps) as an intensity per position map of each contact. The results for the lithium(AC) contact can be seen in Figure 5.5 which shows T30 rise times on this contact varying between ∼47 ns and 55 ns. T60 rise times vary between ∼110 ns and 130 ns and T90 rise times vary between ∼220 ns and 400 ns. Upon inspection of the distributions for each strip, the T90 rise times are found to be between ∼220 ns to 250 ns. The bright area at the top of each rise time map corresponds to strip A which has a skewed rise time distribution that has a very long rise time tail. This is contributing to the larger average rise time on this strip and indeed the very long T90 average rise time observed. The reason for the large spread in the rise time distribution is unknown. On the T30 and T60 plots it is possible to see the variation in rise times with impurity concentration; rises times are slower in the high impurity region. It is not possible to show this on the T90 plot because of the sensitivity scale displayed.

The average rise times for the boron(DC) contact can be seen in Figure 5.6. The T30 rise times on this contact vary from ∼53 ns to 60 ns. T60 rise times vary from ∼125 ns to 135 ns and the T90 rise times vary from ∼280 ns to 330 ns. There are small differences in rise time that are apparent on the T30 plot, with the edges showing faster average rise times than the centre of the detector. Any differences in rise time due to impurity concentration are not visible on this scale. The differences in strip-to-strip average rise times are due to individual strips' electronics and can clearly be seen in the T60 and T90 plots.

5.2.2 Interaction depth determination

The determination of interaction depth is dependent on an excellent knowledge of the mechanisms that change the pulse shapes with depth and a way to parameterize the pulse shapes for identification and comparison. Fundamentally, the pulse shape is a function of the charge movement/collection time and the variety of pulse shapes observed are parameterized by measuring the time at certain intervals along the pulse. Interactions near the

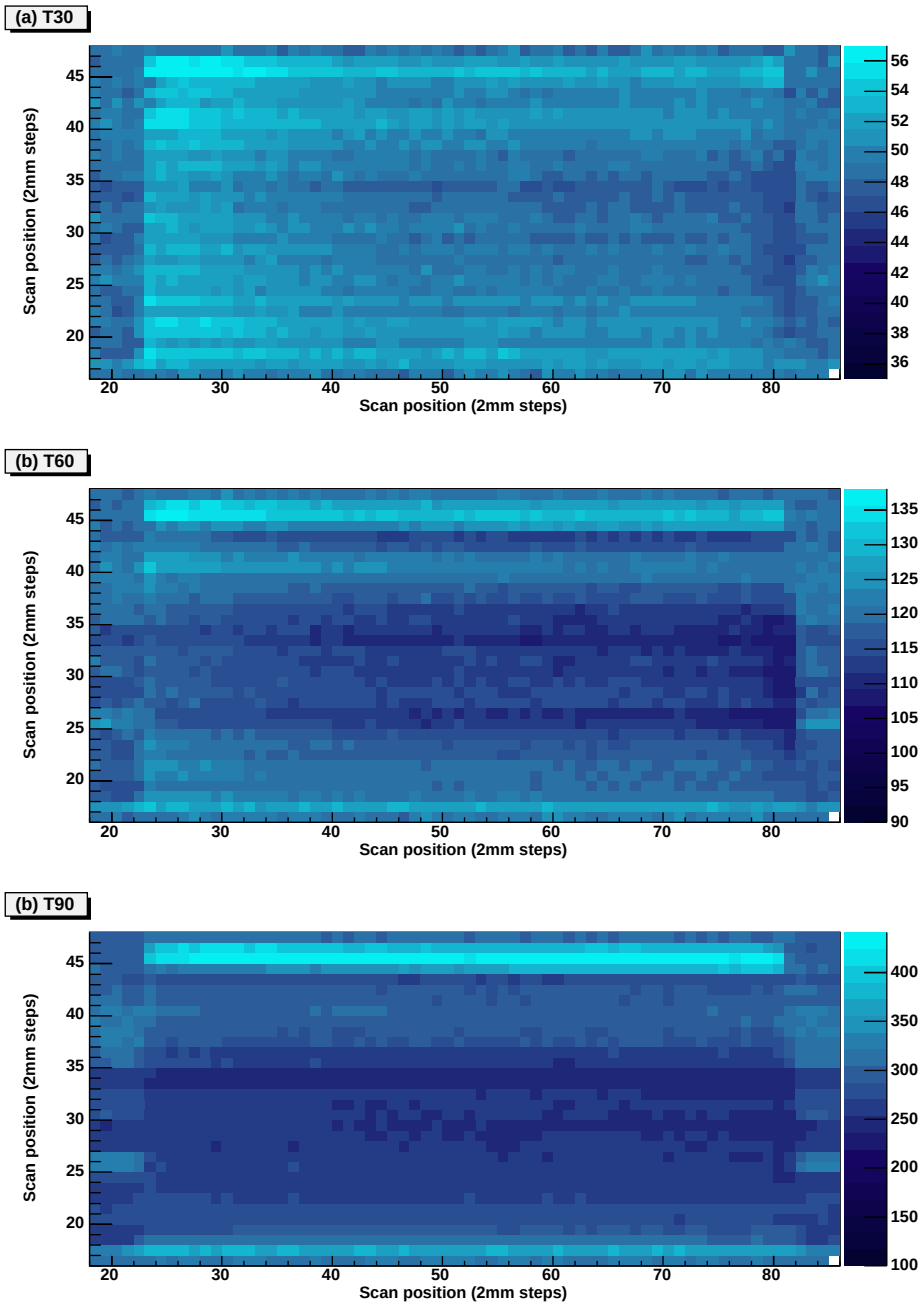

Figure 5.5: Lithium(AC) T30, T60 and T90 average rise time per scan position. Intensity at each scan position is measured in nanoseconds. Impurity concentration is decreasing from left to right.

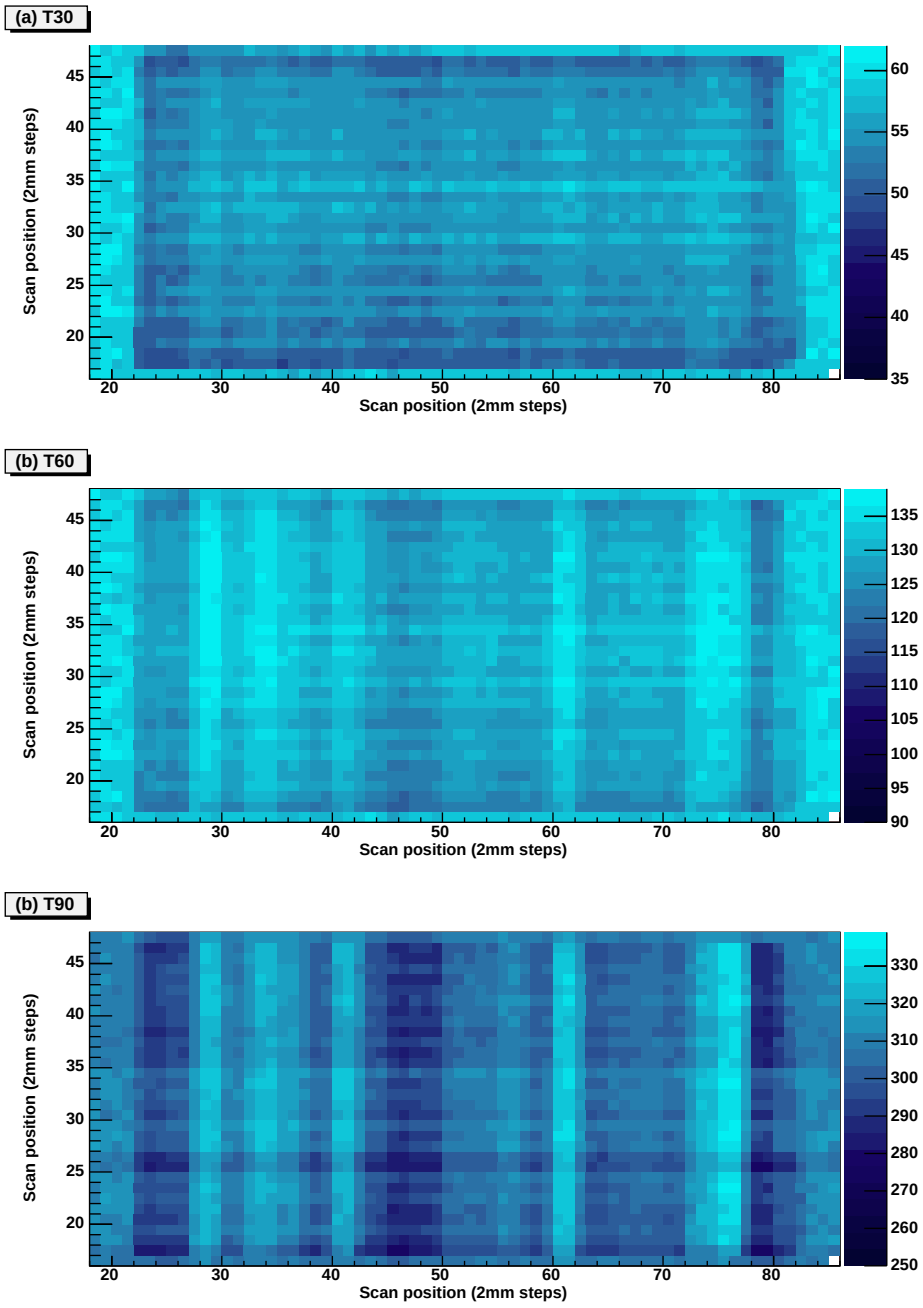

Figure 5.6: Boron(DC) T30, T60 and T90 average rise time per scan position. Intensity at each scan position is measured in nanoseconds. Impurity concentration is decreasing from left to right.

opposite contacts of the detector should produce the longest rise times of the pulses, since one of the charge carriers alway has to traverse the full detector depth. As an indication of the time it takes for electrons and holes to travel 15 mm in the same conditions as the detector, a calculation has been made based on electron and hole mobility in a field of 533 Vcm^{-1}. According to this calculation, electrons will take ∼80 ns to travel the 15 mm depth of the detector and holes ∼120 ns. For a detector to be capable of measuring differences in rise times that are less than the time of travel of the charge carriers to the contacts, it would need to have an excellent preamplifier response. The response of the preamplifiers in the *GREAT* planar detector have already been reported as ∼140 ns for the lithium(AC) contact and ∼340 ns for the boron(DC) contact, making it unlikely that timing differences in the pulse shapes will be clearly identifiable.

Ideally, the pulse shapes at different depths of interaction should be calibrated in some way. This was not accomplished for the *GREAT* planar detector because of experimental difficulties. The rise time distributions for two representative strips on the lithium(AC) contact for uncollimated 662 keV photoelectric interactions are presented and compared with simulations in Figure 5.7. The preamplifier response has not been added to the simulation, and so the rise times are considerably less than the experimental data, although a relative scale has been plotted for both T30 and T90 rise times for comparison with the experimental data. The points plotted show the variation of T30 and T90 with depth of interaction. For all the simulations, the depth of interaction is defined as 1 mm near the lithium(AC) contact through to 14 mm near to the boron(DC) contact. The simulation in Figure 5.7 shows T30 having very little variation near the lithium(AC) contact through to a depth of 7 mm; halfway through the detector depth. T90 is getting shorter in this first 7 mm. T90 is sensitive to the collection time of both charge carriers and as the interaction nears the halfway point, both charge carriers have equal distances to travel. The shortest T90 is therefore the centre of the depth of the detector. From 7 mm to 14 mm, the electrons moving towards the lithium(AC) contact are outside the contact high weighting field, and have progressively longer distances to travel

until they are in the high weighting field region. This is apparent in the simulated T30 values in this region of the detector depth as T30 values get longer with depth in this region. Although holes now have a short distance to travel to the boron(DC) contact, the longer T90 values are due to the longer distance the electrons have to travel to the lithium(AC) contact. The two lithium(AC) strips distributions shown are two centre strips, E and F. The distribution shown by strip E is typical of a lithium(AC) strip while that shown by strip F has a shape more like that seen in the simulation. By comparison with the simulation, strip F has more sensitivity in T30 and T90 for deep interactions than the other lithium(AC) strips. Without a depth calibration it is unclear where in the distribution the rise times lie for the deeper interactions on the less sensitive strips.

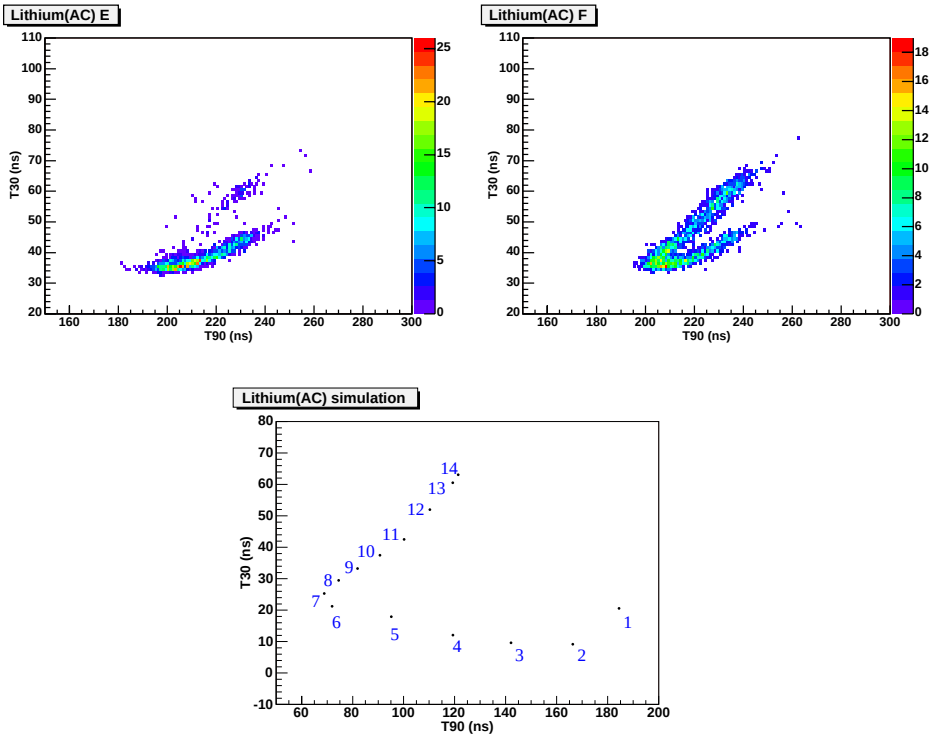

Figure 5.7: Lithium(AC) experimental rise time distributions; T30 against T90. The simulated data also show how the distributions vary with depth in 1 mm steps numbered 1 to 14 on the figure, with 1 mm being close to the lithium(AC) contact and 14 mm being near to the boron(DC) contact.

The rise time distributions for two representative boron(DC) strips and for the boron(DC) simulation are shown in Figure 5.8. The pulse shape and hence rise times are expected to change with depth of interaction. The variation of rise times with depth are shown on the simulation plot, with a depth of 1 mm being interactions near the lithium(AC) contact and 14 mm being interactions near to the boron(DC) contact. In the simulation, interactions near the boron(DC) contact have fast T30 rise times corresponding to the short distance the holes have to travel to be collected. The T90 rise times are longer because the charge pulse is induced until all moving charges have stopped; at these depths electrons are travelling and collecting long after the holes have collected on the boron(DC) contact. The T90 value decreases until 4 mm and increases at depths beyond this, as the longer hole collection time dominates the T90 value. The T30 value, corresponding to the hole collection, increases with increasing depth. In Figure 5.8 the rise time distributions shown for boron(DC) strips 4 and 10 have only a part of the distribution of the simulation. None of the boron(DC) strips have the T30, T90 distribution that is identified in the simulation as interactions near to the boron(DC) contact. The experimental data are again for 662 keV photoelectric interactions that are expected to interact throughout the entire depth of the detector. From the experimental data, once more for interactions near to the boron(DC) contact, it is not clear where this part of the rise time distribution lies, and a depth calibration is necessary to identify the differences between the experimental and simulation data.

Transient charges[1] also change shape with the depth of interaction and therefore calibration is necessary for a full transient analysis to be performed. Simulations have been made of the varying transient shape with interaction depth where no experimental data are available. However, it has been possible to extract some transient results from the data for use with lateral interaction position analysis (Section 5.2.3), and some comparisons

[1]With real charges already extracted, an algorithm has been used to distinguish transient charges from noise. An average noise is determined from the last 350 samples in a signal. The pulse is a transient if the absolute maximum value (transients can be negative too) is greater than three standard deviations of the average noise.

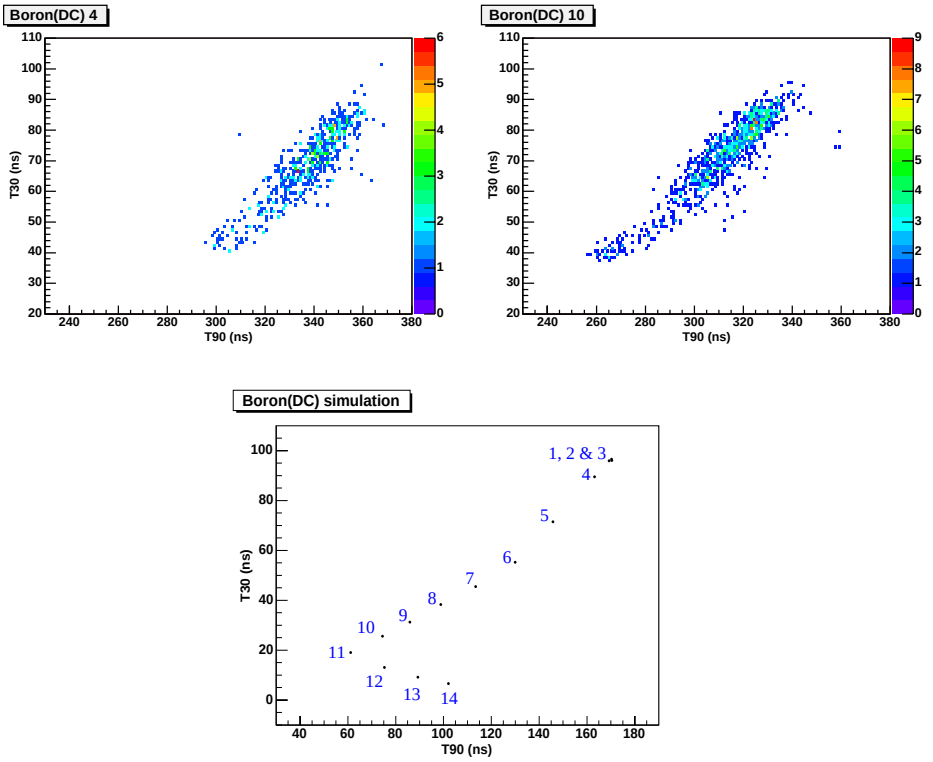

Figure 5.8: Boron(DC) experimental rise time distributions; T30 against T90. The simulated data also show how the distributions vary with depth in 1 mm steps numbered 1 to 14 on the figure, with 1 mm being close to the lithium(AC) contact and 14 mm being near to the boron(DC) contact.

have been made between experimental and simulated transients.

The simulation has been used to produce pulse shapes and adjacent strip transients for strips on both contacts. The simulated real charge pulses on boron(DC) 8 and their corresponding transients on boron(DC) 7 are displayed for many interaction depths in Figure 5.9. The *GREAT* planar detector has inverting preamplifiers on the boron(DC) strips, therefore all simulated real charges and transients are of opposite polarity to those seen in the experimental data. Real charges for interactions far away from the boron(DC) contact (1 mm) show the long T30 rise time discussed earlier and their transients also reflect this long rise time. On the simulation, the

transients are fully negative until an interaction depth of 10 mm which is 5 mm from the boron(DC) contact. At this interaction depth of 10 mm the transients become bipolar and gradually become more positive as the interaction gets closer to the boron(DC) contact. In the experimental data for the boron(DC) strips, remembering polarities are inverted, no negative transient pulses are observed at all. Negative transients on this contact would correspond to interaction depths near to the contact. It has already been shown in the rise time plots in Figure 5.8, that the detector appears to be insensitive in this region; with rise times for interaction depths near to the contact not behaving in the same way as the simulation. It can be concluded that for interactions close to the boron(DC) contact, pulses, real and transient, do not behave as expected and the reasons are unknown.

As it is important for lateral interaction position analysis that the depth of interaction is known, the simulation has been used to show how transient height varies as a function of interaction depth in the detector for both contacts (Figure 5.10). Even though the boron(DC) contact transients did not change polarity in the experimental data, the lithium(AC) contact did have a small percentage of transients with at least some negative component. By comparing the interaction depths with the transient heights, it was possible to choose rise times from the experimental data that had the largest transients, therefore some lateral interaction position analysis was performed.

5.2.3 Lateral interaction position

If an interaction occurs near the edge of a strip, the transient induced on the nearest adjacent strip will be at its largest. Conversely, if the interaction occurs near the opposite edge of a strip and the same adjacent strip as before is observed, the transient induced on this adjacent strip will be at its smallest. This theory can be tested for a detector by moving a collimator across a strip and observing the induced transient heights in the neighbouring strips. As transient height is dependent on pulse height, a higher energy interaction is preferable to produce the largest transients possible. Unfortunately, the finely collimated data acquired for this detector used a cobalt-57 source with

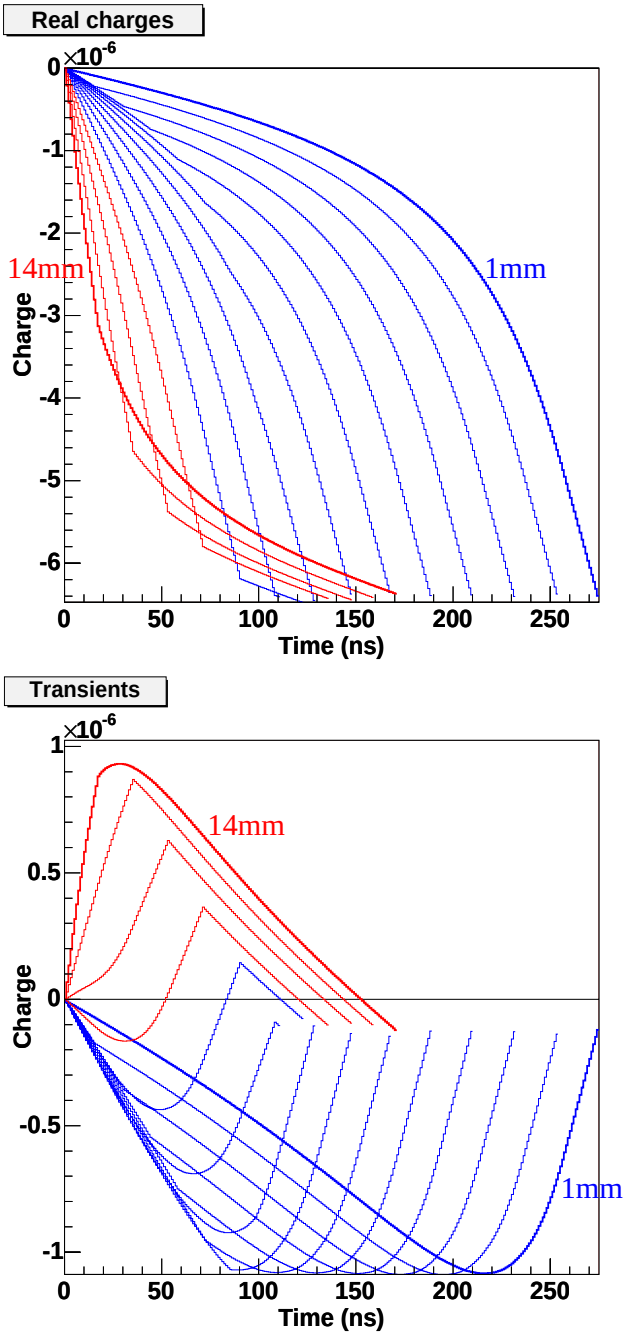

Figure 5.9: Simulated real charges and their associated transients as a function of interaction depth in the detector, where 1 mm is close to the lithium(AC) contact and 14 mm is close to the boron(DC) contact. All simulated interactions occur in the same lateral position and are 122 keV in energy. The real charges shown are induced on boron(DC)8 and the transients on boron(DC)7.

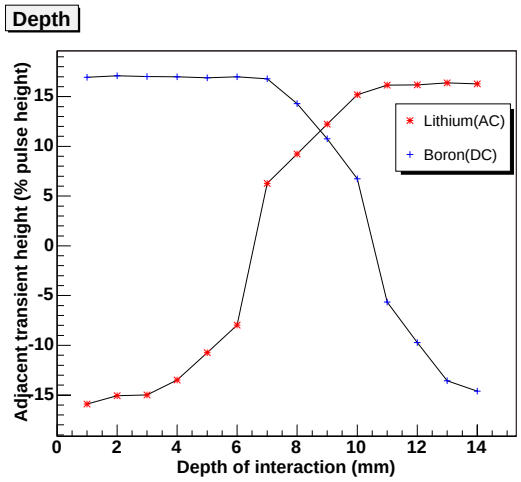

Figure 5.10: Transient heights as a percentage of real charge pulse height, varying with interaction depth for both lithium(AC) and boron(DC) contacts.

its 122 keV gamma ray (experiment 3). The transients induced were small and close to the noise. Typical transients induced on a boron(DC) strip from a 122 keV photoelectric gamma-ray interaction, are shown in Figure 5.11. The noise on each signal is ∼11 mV peak-to-peak. If the transients' heights are measured from the centre of the noise distribution to the centre of the transient height distributions, they have heights of ∼7 mV. The transients shown in this figure should vary in height with (a) being the smallest and (d) the biggest, to coincide with the different lateral collimator positions. Any differences are small and hidden by the noise and consequently this data set cannot be used to improve the lateral position sensitivity of the *GREAT* planar detector.

A simulation has been performed that varies the interaction position across a strip to gauge the difference in transient heights with varying lateral position. Two energies have been simulated at different depths of interaction, 122 keV with a shallow interaction near to the boron(DC) contact, and 662 keV with a deep interaction near to the lithium(AC) contact. The results for the 122 keV interactions can be seen in Figure 5.12. For the 122 keV

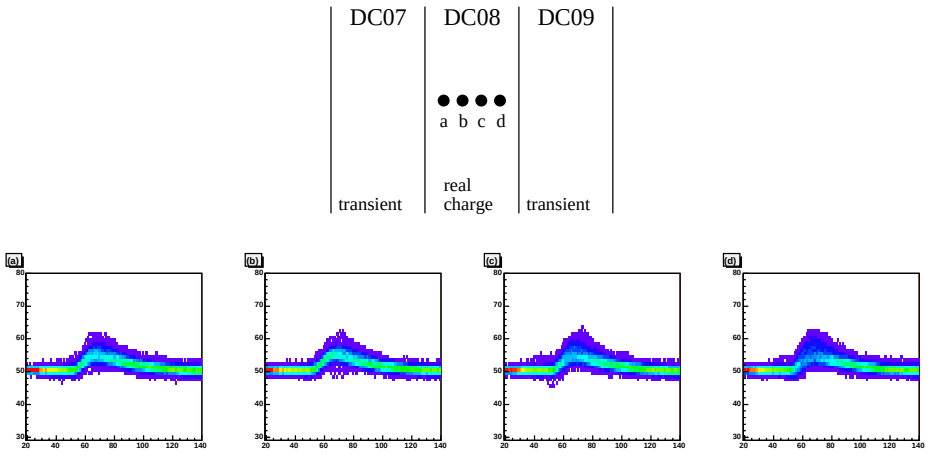

Figure 5.11: A finely collimated source positioned at four lateral positions a, b, c and d, in front of boron(DC)8. Transients are observed in adjacent strips boron(DC)7 and boron(DC)9. Transients shown are those induced on boron(DC)9 while the collimator is at each of the four positions, a to d.

interactions shown, the two contacts show differing sensitivity of transient height to lateral interaction position. The lithium(AC) strips have a 14% difference in height for interactions happening 3 mm away from each other, while the boron(DC) strips only show a 6% change in height over the same distance and for the same interactions. The simulated 662 keV interactions show the same effect with the contact nearest to the interaction, showing low sensitivity to changes in lateral position. Again, it is important to calibrate the depth of a planar detector if lateral position sensitivity is to be improved beyond strip width. The asymmetry term has been calculated for the simulated data at each lateral position shown in Figure 5.12, giving results that allow us to speculate that the asymmetry term follows a linear relationship with lateral distance, and is possibly not dependent on energy or contact.

Although a lateral position dependence could not be shown for transients in adjacent strips using the collimated data, it was clear from the uncollimated data (experiment 1) that higher energy interactions produced visibly

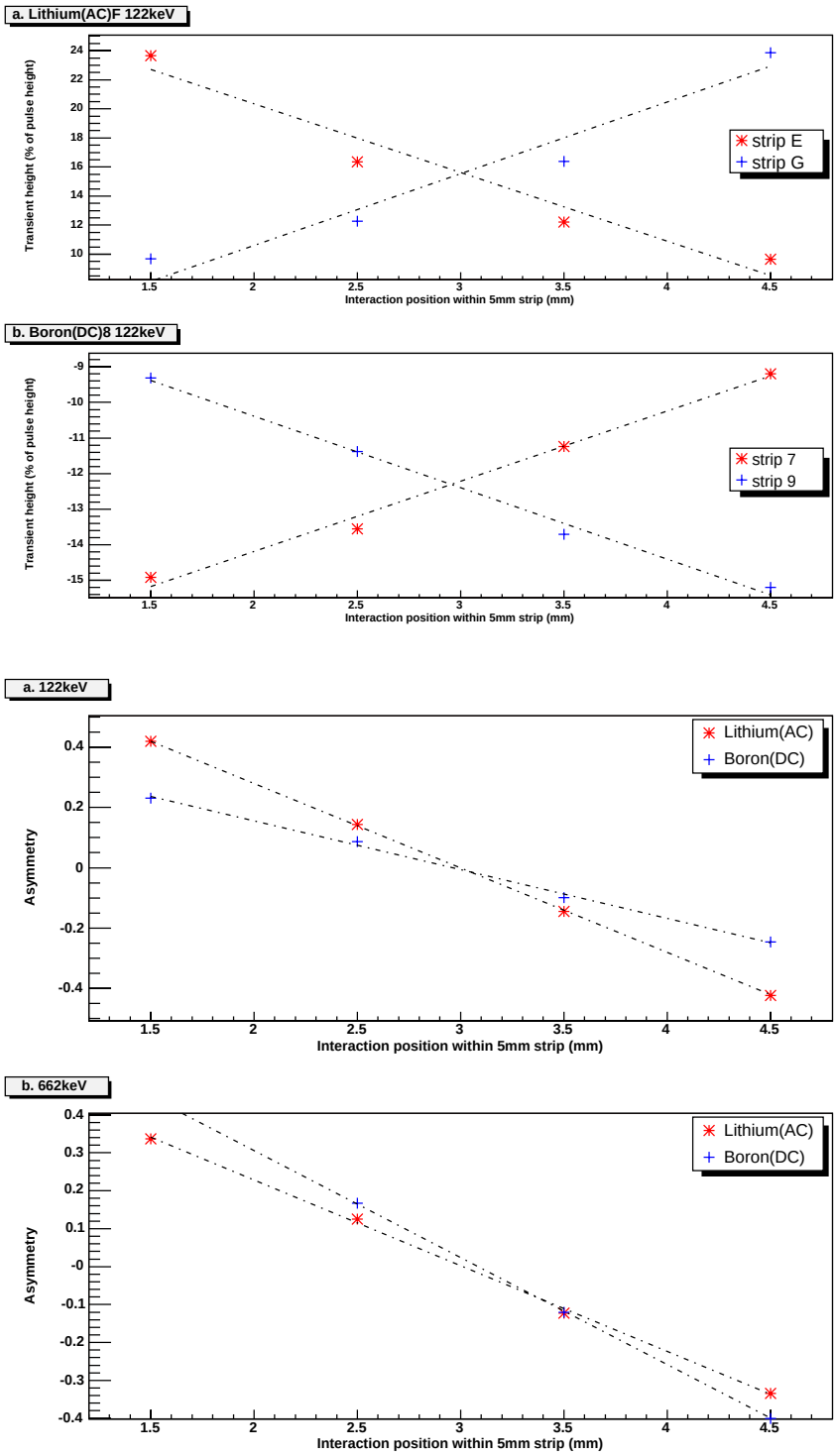

Figure 5.12: Top plots: A simulation of the varying interaction position across a 5mm strip shows a corresponding change in transient height on the two adjacent strips. Bottom plots: The asymmetry calculated from the simulation data and plotted for two different energies, on both contacts.

different sized transients in strips further away from the strip containing the interaction. The heights of transients in adjacent, next-but-one and next-but-two strips have been measured to determine the large scale lateral position dependence of transients in this detector and compared with the same measurements made using the simulated data. Two data sets have been used for these measurements: 1 mm collimated Co-57 positioned over the centre of strips and uncollimated Cs-137.

It has already been shown that the transients shape and height varies with interaction depth. The transients measured were selected by attempting to limit the region in depth that the real interaction occurs. This was achieved in most cases by selecting a T30 rise time for each energy, on each contact, that gave the largest transients. A separate selection criterion was used for the lithium(AC) 662 keV measurement, as the transients had a large height distribution that could not be refined by selecting one particular T30 rise time. Instead, a transient height was chosen on one of the adjacent strips as a selection gate, and the transient heights were measured on all other neighbours that corresponded to the same interaction.

Contact	**Energy (keV)**	**T30 gate (ns)**	**T30 position in distribution**
lithium(AC) F	122	58 - 62	long
boron(DC) 8	122	45 - 49	short
lithium(AC) F	662	n/a	n/a
boron(DC) 8	662	79 - 83	long

Table 5.1: T30 rise-time gates used for large scale lateral position sensitivity measurements.

The transients on six strips, three each side of the real interaction strip, have been measured and plotted in Figure 5.13. For analysis of the uncollimated results, the interaction was assumed to be at the centre of the real charge strip, and differences in lateral positioning on that strip considered as an error in transient distance from the interaction. For both energies and

contacts, a distance dependent transient height can now be observed. To quantify this dependence a fit has been made to the plots. The plots look far from linear, but the only fit that could be made across all plots was a linear one, which has been used for direct comparison between the different energies and contacts. Even though lateral position sensitivity could not be shown across a strip on the *GREAT* planar detector, by using the fitted linear relationship it can be predicted that the sensitivity exists, although hidden by noise, and that sensitivity across a 5 mm strip causes between 4 and 8% transient height difference. Linear fits have been made to the simulated data that show between 5 and 8% difference in transient height for interactions 5 mm apart in the lateral direction.

From the transient pulse height analysis it can be concluded that experimental and simulated data compare well. Using a linear fit to the simulated data plots it can be deduced that differences of transient pulse heights corresponding to varying interaction positions across the 5 mm strips, are 1.5 keV\mm for 122 keV gamma rays and 7.9 keV\mm for 662 keV gamma rays. Hence noise levels in a future detector would need to be less than these values for a 1 mm position resolution to be achieved.

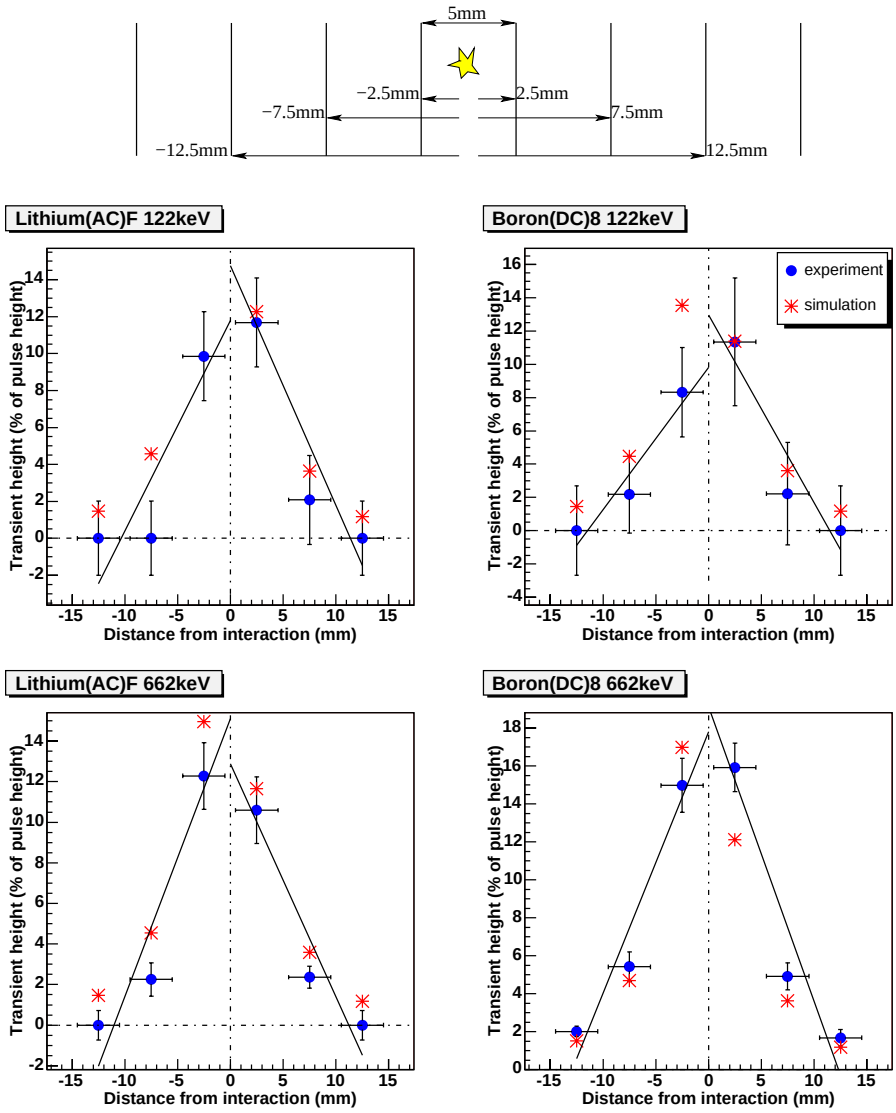

Figure 5.13: Transient heights as a function of distance from interaction strip. As the 662 keV data is uncollimated, the interaction position is assumed to be in the centre ±2.5 mm of a strip.

Chapter 6

Conclusion and Discussion

6.1 Conclusion

To enable imaging of small animals, new detection techniques are required to improve medical imaging to beyond the position resolution achieved today. The proposed new positron emission tomography imaging system will consist of two planar germanium strip detectors in a rotating gantry around the patient. Improvements to existing systems will be made by using and not rejecting scattered gamma rays. This is achievable by utilising the excellent energy resolution offered by germanium detectors and applying gamma-ray tracking techniques to reconstruct scatters within the detector. A requirement of gamma-ray tracking is the location of interactions within the detector volume. This work presents the characterisation of a planar germanium detector and the feasibility to locate interactions in three dimensions within such a detector for use as an imaging tool.

The characterisation is a calibration of the response of the detector to radiation events throughout its volume. Scanning a finely collimated beam of gamma rays over the detector surface provides a large grid of positions for which charge pulses can be investigated. A digital acquisition system was employed to facilitate the analysis of charge pulse shapes to provide an effective granularity beyond the detector segmentation.

The initial tests of the *GREAT* planar detector showed the preamplifiers have been configured with rise times much greater than the time the charge carriers would take to traverse the detector and be collected. Nevertheless, the T30 and T90 pulse shape parameters were investigated to gauge the distribution of pulse shapes from interactions throughout the depth of the crystal. These distributions were compared to those from simulations and were sufficiently different from the simulations that it was apparent a calibration of the depth of the detector is necessary to enable pulse shape analysis to be used for location of interaction within the depth of the crystal.

Determination of lateral interaction position involves the analysis of transient pulses on neighbouring strips. The collimated beam used for the scans had 122 keV gamma rays. The height of transient pulses were found to be $\lesssim$15% percent of the real charge pulse and from extrapolation this is expected to change by a further $\sim$4 to 8% of the real charge pulse height over a 5 mm change in lateral interaction position. For the 122 keV interactions used in the scan, this meant the difference in transient height with changing lateral position was small and hidden by the noise. However, the lateral position plots did show the detector has the potential to use transient pulses for position information and this could have been demonstrated if a larger energy gamma ray had been used for the scan. The success of the imaging project depends upon scattered gamma rays being used. For an interaction of 122 keV to be located in a lateral position to less than 5 mm, the noise in the *GREAT* planar detector would need to be halved. From a comparison between experimental and simulated data, the *GREAT* planar detector has a position resolution of $\sim$1 mm to 2 mm for 662 keV gamma-ray interactions.

6.2 Discussion

The *GREAT* planar detector was not designed for the imaging project or indeed for pulse shape analysis ensuring experimentation was challenging. The dewar designed for the *GREAT* planar is not multi-positional and therefore the detector was not suitable for the Liverpool scanning apparatus. For future detectors to be scanned and data collection maximised within time

constraints, the fully automated positioning table at Liverpool should be used to its full capabilities and this is only possible if detector systems are multi-positional.

There are other considerations for planar detector design for use with pulse shape analysis and gamma-ray tracking. The importance of calibrating the depth of the crystal for a full characterisation has been realised and this can be done by scanning the side of the detector to produce a data base of pulse shapes at defined depths. Calibration of depth in this manner is best achieved if one of the crystal edges is near to the detector housing. Two SmartPET planar detectors are now being characterised for the project. Scans of the surface and side of one of the detectors are now complete. Several surface scans have been made with differing energy collimated beams. The results shown in Figure 6.1 are average pulse shapes at 1 mm intervals through the depth of the planar showing a depth position resolution of 1 mm is attainable in this detector. The new generation SmartPET detectors have fast preamplifiers and low noise levels. Based on calculations made with the *GREAT* planar detector, lateral position resolution will be 1.5 mm for 122 keV gamma rays and 0.5 mm for 662 keV gamma-ray interactions. Therefore, the 1 mm position resolution required for the PET project is feasible with these detectors.

The energy resolution for data acquired through digital electronics was poor. No algorithms were implemented within the GRT4 cards. This has now changed and a moving window algorithm has been implemented in the cards. Energy resolutions are nearer to those of data acquired with analogue electronics. Energy determination is important especially when adding back scattered gamma rays for tracking gamma rays successfully. Crosstalk should be either minimised by design or fully investigated at all energies and corrected for. Energy resolution also depends on charge collection; problems with the *GREAT* planar have been highlighted in this work. A full three dimensional position resolution relies on charge collection on both contacts being optimised in future designs.

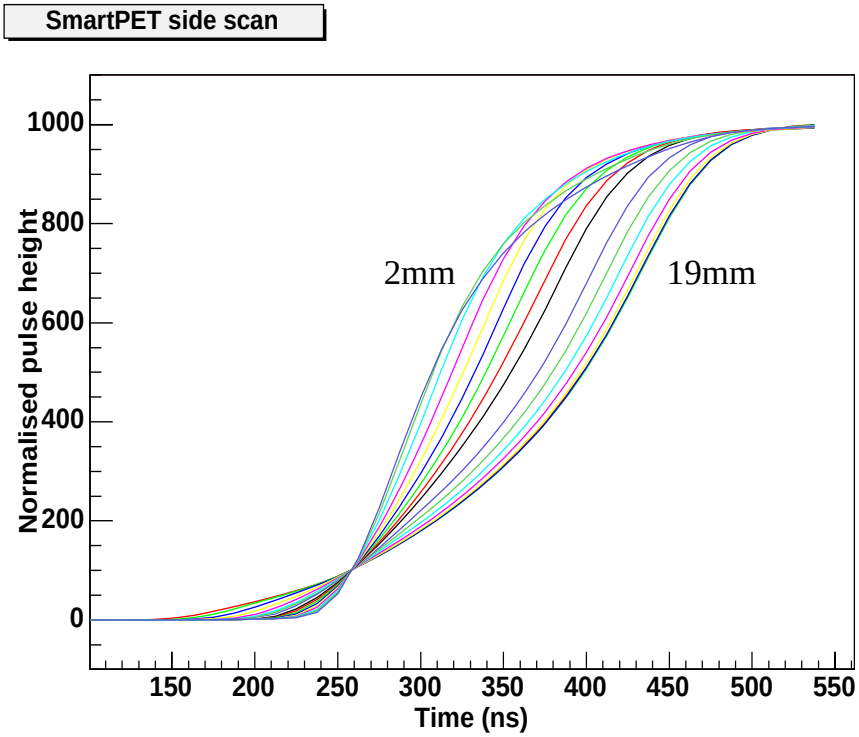

Figure 6.1: Averaged 662 keV pulses calibrated at different depths in the first SmartPET planar detector [Tur05]. Pulse heights have been normalised to 1000 and pulses have been lined up at the T10 position to provide a starting point away from the noise for further pulse shape analysis.

A recommendation can be made for the initial tests made upon detector delivery from a manufacturer. For use with pulses shape analysis, initial tests should include more than the standard energy resolution tests for acceptance of the detector. They should also include the response of the preamplifiers through the test inputs and a test of the basic rise time distributions to ensure rise times are suitable.

6.3 Future work

For an increased granularity beyond the segmentation, a number of improvements can be made to the *GREAT* planar detector and its character-

isation. With the present preamplifiers an improved strip granularity can be achieved by re-scanning the surface of the detector using a finely collimated source with a larger energy gamma ray and calibrating the transient heights. In order to gain an increased granularity in the depth a scan of the detector depth should be made to calibrate the pulse shapes. Ultimately, if the future of the *GREAT* planar detector involves pulse shape analysis, the present preamplifiers should be replaced in favour of preamplifiers with a fast rise-time response.

Appendix A

Detector Characteristics

A.1 Crystal orientation

The orientation of the crystal affects charge carrier mobility, with drift velocity depending on orientation. For the *GREAT* planar detector, it was specified that the planar axes should be parallel to the crystal planes. The orientation of the detector with respect to the crystal planes is shown in Figure A.1.

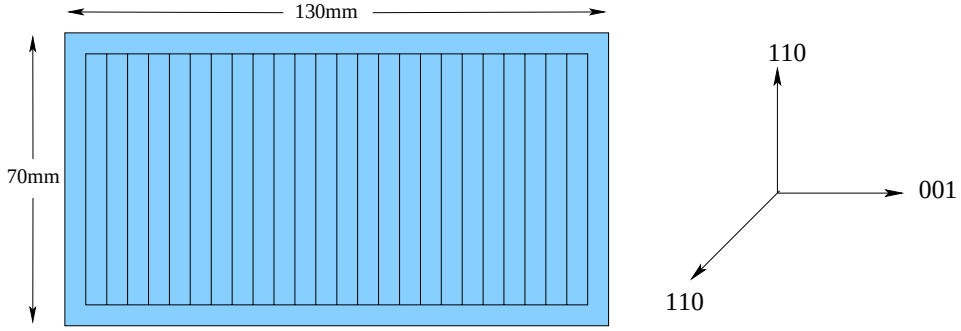

Figure A.1: Crystal orientation of the *GREAT* planar detector.

A.2 Operational characteristics

Measured DC offset and noise, and energy resolutions are shown for all channels in Tables A.1, A.2 and A.3.

Contact	**DC offset (mV)**	**noise (mV)**
1	+100	5
2	$\leq +5$	5
3	≤ -5	5
4	+5	5
5	≤ -5	5
6	≤ -5	5
7	-5	5
8	$\leq +5$	5
9	$\leq +5$	5
10	$\leq +5$	5
11	+10	5
12	+12	5
13	0	5
14	0	5
15	$\leq +5$	5
16	$\leq +5$	5
17	$\leq +5$	5
18	$\leq +5$	5
19	≤ -5	5
20	$\leq +5$	5
21	+7	4
22	+15	5
23	≤ -5	5
24	≤ -5	5
A	-5	3
B	≤ -5	4
C	≤ -5	5
D	≤ -5	4
E	-5	5
F	+5	5
G	-8	5
H	-5	4
I	+25	5
J	$\leq +5$	5
K	≤ -5	4
L	-9	5

Table A.1: DC offset and noise measured from preamplifier outputs

	60 keV		122 keV	
Contact	**FWHM (keV)**	**FWTM (keV)**	**FWHM (keV)**	**FWTM (keV)**
1	1.73	5.97	1.64	4.36
2	1.80	4.11	1.65	3.40
3	1.75	3.92	1.74	3.69
4	1.69	3.92	1.72	3.45
5	1.80	4.12	1.74	3.83
6	1.81	3.95	1.69	3.46
7	1.73	3.72	1.63	3.37
8	1.64	3.76	1.65	3.43
9	1.63	3.91	1.66	3.35
10	1.63	3.53	1.55	3.15
11	1.60	3.37	1.58	3.32
12	1.75	3.83	1.68	3.38
13	1.76	3.90	1.65	3.55
14	1.69	3.91	1.57	3.08
15	1.69	3.71	1.66	3.40
16	1.66	3.68	1.66	3.16
17	1.65	3.71	1.61	3.24
18	1.73	3.82	1.71	3.33
19	1.74	3.35	1.71	3.91
20	1.60	3.24	1.67	3.50
21	1.61	3.19	1.66	3.46
22	1.65	3.23	1.66	3.61
23	1.65	3.11	1.74	3.82
24	2.17	5.03	2.05	4.92
A	2.02	4.05	2.09	3.98
B	1.55	3.15	1.66	3.17
C	1.63	3.00	1.79	3.11
D	1.44	2.85	1.52	2.93
E	1.58	3.07	1.67	3.27
F	1.56	2.94	1.70	2.96
G	1.58	3.09	1.67	3.14
H	1.35	2.76	1.52	2.91
I	1.76	3.32	1.82	3.34
J	1.78	3.27	1.81	3.37
K	1.54	2.95	1.61	3.08
L	2.22	4.15	2.24	4.13

Table A.2: Analogue acquired energy resolution results at 60 and 122 keV for all strips. Contacts 1-24 are the boron(DC) strips and contacts A-L are the lithium(AC) strips.

	60 keV	**122 keV**	**662 keV**
Contact	**FWHM (keV)**	**FWHM (keV)**	**FWHM (keV)**
1	4.55	5.40	6.4
2	4.94	5.14	7.92
3	4.72	5.28	11.20
4	4.74	4.64	8.90
5	4.40	4.65	10.50
6	4.60	4.69	7.44
7	4.93	4.60	7.43
8	4.70	4.85	8.40
9	4.38	4.43	6.43
10	4.48	4.22	5.82
11	4.39	4.19	5.12
12	4.61	5.14	7.21
13	4.70	4.81	7.46
14	4.36	4.61	8.85
15	5.00	4.65	6.48
16	5.08	4.59	8.87
17	4.64	4.71	6.44
18	4.85	4.82	6.39
19	4.67	4.51	7.11
20	4.72	5.08	7.05
21	4.73	4.53	10.44
22	4.65	4.94	9.53
23	4.63	5.12	6.65
24	5.73	5.26	6.54
A	4.23	4.41	4.63
B	4.50	4.47	5.30
C	4.24	4.01	5.16
D	4.48	3.85	5.42
E	4.07	3.89	5.32
F	4.47	4.16	5.75
G	4.74	3.87	4.89
H	3.90	3.73	4.72
I	3.90	3.93	4.71
J	3.97	3.99	4.92
K	3.86	3.68	4.33
L	3.92	4.17	5.23

Table A.3: Digitally acquired energy resolutions at 60, 122 and 662 keV for all strips. Contacts 1-24 are the boron(DC) strips and contacts A-L are the lithium(AC) strips.

Appendix B

Electric Field Simulations

The characterisation of HPGe detectors for pulse shape analysis requires an excellent understanding of the whole signal generation process. An aid to understanding pulse production in any particular detector is a comparison with simulation. A simulation package has been developed at the Intstitut de Recherche Subatomique (IReS), Strasbourg, France [Med04]. The multi geometry simulation (MGS) code is a matrix based numerical method developed to operate in MatLab [Mat]. The simulation starts with a definition of the detector geometry and specifications and calculates, via a number of intermediate steps, the electric and weighting fields within the crystal. This enables charge trajectories and velocities to be found for specified energy interactions at defined positions. The simulation calculates the induced real and transient charges produced by the coupling of the moving charges and the sensing electrodes for comparison with experimental data. The code has incorporated within it a scan facility that can mimic an experimental scan with a collimated source for the simulation of pulse shapes from a selected area of the crystal.

B.1 Calculating the fields

The necessary steps to produce a full simulation of the *GREAT* planar detector are outlined as follows:

1. *Create geometry.* The geometry and basic parameters of the *GREAT*

Grid step (size of matrix)	1 mm
Crystal length	130 mm
Crystal height	70 mm
Crystal depth	15 mm
Forward space (distance between housing and anode face of crystal)	9 mm
Back space (distance between housing and cathode face of crystal)	14 mm
Lateral space (distance between housing and sides of crystal)	25 mm
Lateral space (distance between housing and top/bottom of crystal)	10 mm
Anode bias	+800 V
Cathode bias	0 V
Minimum impurity concentration	1×10^9 cm^{-3}
Maximum impurity concentration	5×10^9 cm^{-3}
Germanium permittivity	16
Temperature (crystal)	90 K

Table B.1: Parameters required by MGS code to create matrices.

planar detector have been included in the MGS code along with a library of standard detector templates. A first step in the simulation is to confirm or change the basic geometry and electrical properties. The parameters used in the simulation are shown in Table B.1. The geometry matrix created for the remaining simulation steps can be plotted as a visual check as shown in Figure B.1.

2. *Solve Poisson.* The Poisson equation can be solved by MGS algorithms by using a number of different methods: direct, relaxation and successive over relaxation (SOR). The direct method solves a large number of simultaneous equations and requires a large amount of storage to carry out the calculations. The relaxation and SOR methods use an iterative approach. Following an initial guess, iterations are made until a solution is found. The iterative methods were chosen for the *GREAT* planar simulation due to computing limitations. A matrix of the potential is produced for the detector volume; the potential for the *GREAT* planar can be seen in Figure B.2 which shows a positive potential of +800 V at the anode through to 0 V at the cathode.

3. *Solve electric field.* An electric field matrix is produced by differentiating the potential. An option for plotting the vectorial electric field with the electric potential is also available.

4. *Solve drift velocity.* The MGS code can take account of the anisotropy of charge carrier drift velocity using drift velocity information supplied by [Mih00]. The angle of anisotropy for the *GREAT* planar detector is zero because the crystal axes are parallel to the lattice planes. The drift velocity of the charge carriers is calculated from the electric field and has been plotted in Figure B.3.

5. *Solve weighting field* Calculation of the weighting field is necessary for the determination of induced charges on the electrodes. The simulation uses previous results from the drift velocity calculation and the potential mapping solution to calculate induced charges using Ramo's theorem and solves the weighting potential by the use of the same algorithms used to solve the Poisson equation. The simulated weighting field around boron(DC) 2 has been plotted in Figure B.4. The weighting field around the strip falls to a half beyond the immediate vicinity of the strip.

6. *Create pulse shapes* The matrices are now complete and the user can input a position and energy of interaction within the detector volume and the charge trajectories and induced pulses are outputted for analysis. A scan of a larger area can be made for comparison with experimental data. The response of the preamplifier is not included in the simulation. For a like-to-like comparison of pulse shapes from simulation to experimental data, the preamplifier response should be added by the user. Simulation data shown in this work has not had a preamplifier response added.

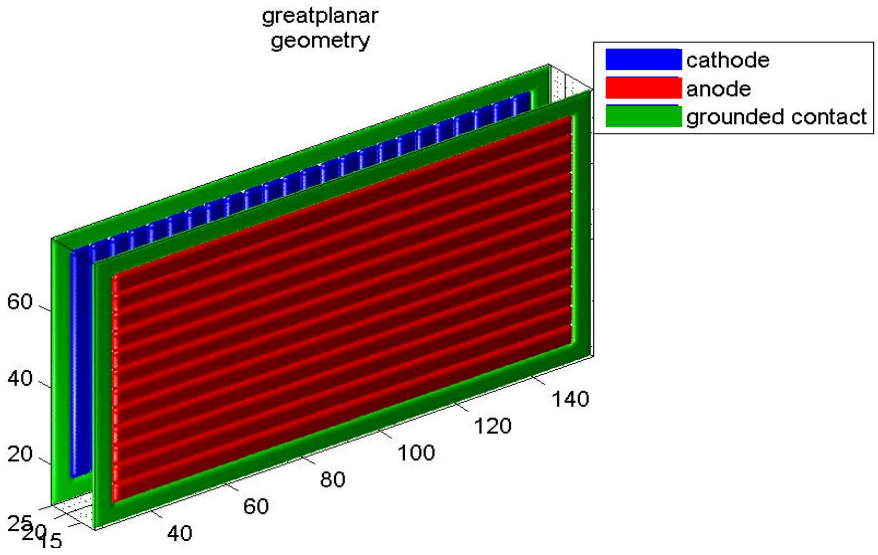

Figure B.1: Step 1: create geometry. The axes scales start at a non-zero position due to the inclusion of the distances from the housing to the crystal in the simulation.

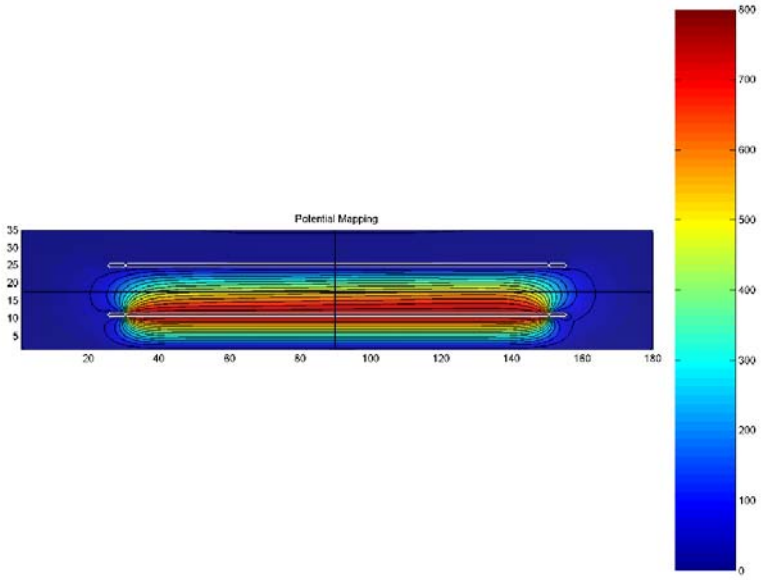

Figure B.2: Step 2: solve the electric potential for the detector volume. A positive potential of +800 V at the anode to 0 V at the cathode.

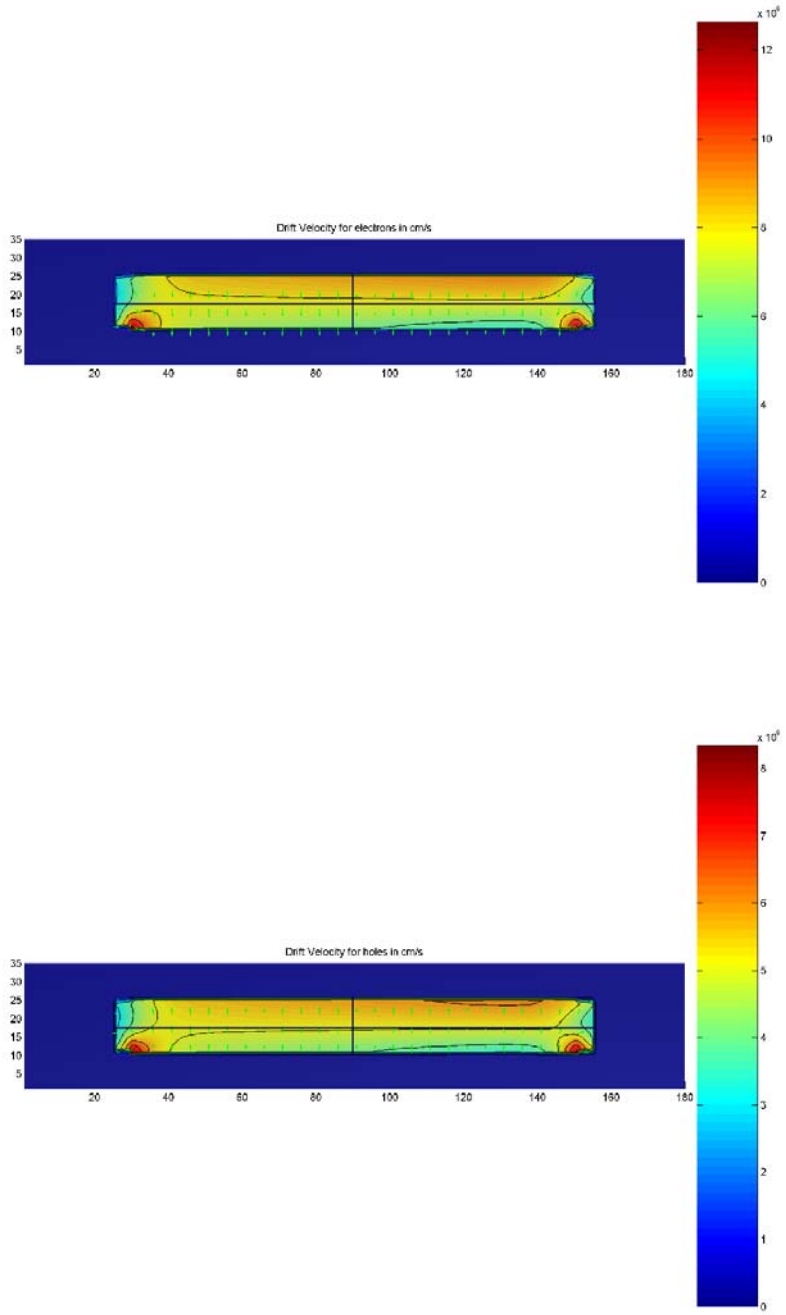

Figure B.3: Step 4: drift velocity of electrons (top) and holes (bottom).

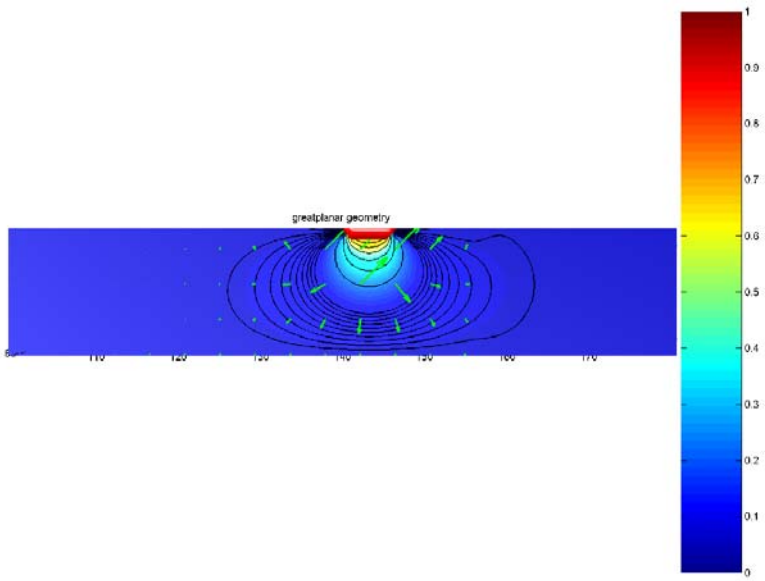

Figure B.4: Step 5: weighting field. The simulated weighting field of boron(DC) 2 falls to half its value at ∼5 mm away from the strip.

Appendix C

Collimator Simulation

A simulation has been made to investigate the spread of the collimated beam onto the surface of the crystal using Monte Carlo N-Particle code (MCNP) [MCN]. MCNP is a general purpose code that simulates photon transport in an arbitrary three-dimensional configuration geometry.

Two simulations were performed [Coo05] describing two collimator geometries, as used in experiments 2 and 3. The collimators' dimensions were 2 mm core diameter, 80 mm long and 1 mm core diameter, 40 mm long. For the simulation they were set inside a lead brick similar to those used in the experiments. The lead brick had dimensions 80 mm high, 72 mm deep and 152 mm wide. Both experiments used a 7.4 MBq Cobalt-57 point source. The distance from the edge of the collimator to the crystal surface was 20 mm.

The geometry and results of the simulation of the 1 mm diameter collimator are shown in Figure C.1. For a point source, the simulation showed 87% of the total flux lies within a 1 mm diameter spot on the surface of the detector crystal and 99% of the total flux is within a 1.6 mm diameter spot on the crystal surface. For the 2 mm diameter collimator shown in Figure C.2, 99% of the total flux is within a 2 mm diameter spot on the crystal surface.

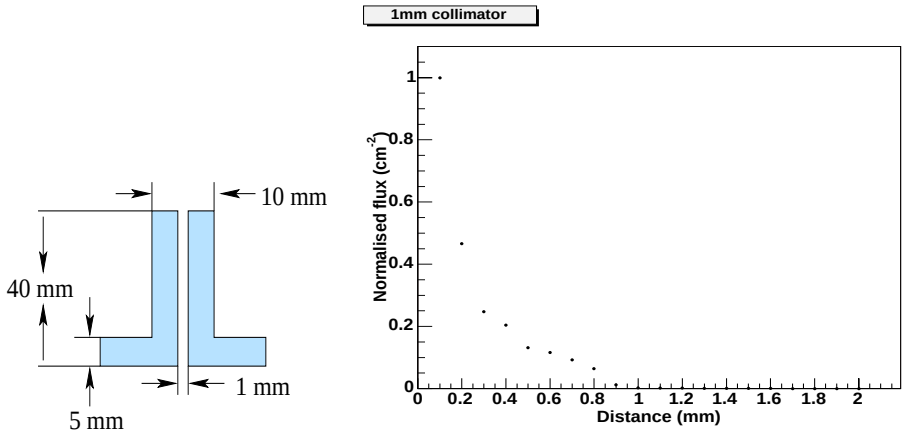

Figure C.1: 1 mm collimator geometry and simulation results. Distance is described as 0 mm at the centre of the collimator and flux has been normalised to the maximum flux through the collimator.

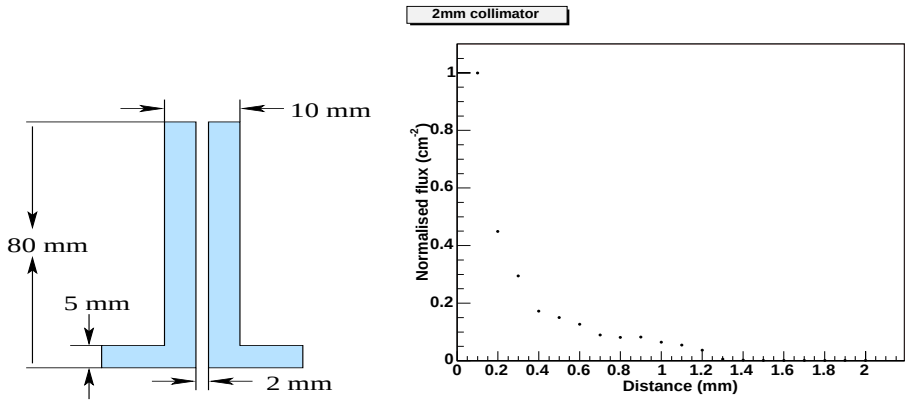

Figure C.2: 2 mm collimator geometry and simulation results.

Appendix D

Background Investigation

The collimator simulations show only the spread of the beam onto the surface of the crystal and do not show any photons passing through the sides of the collimator or lead brick. The amount of background observed in the experiments is far more than the spread of the collimator shows. With the acquisition system set to collect anything above the noise, interactions from all energies were acquired and stored for the experiments performed. Also, a higher background might be expected for the *GREAT* planar detector due to the beryllium and aluminium windows in front of the two sides of the crystal and no extra shielding around the detector, only that around the source. The amount of leakage through the source shielding has been investigated by observing the number of gamma rays detected when the collimated source is placed at different lateral distances away from the crystal as shown in Figure D.1.

The investigation to check the effectiveness of source shielding was conducted from two perspectives:

1. Concentrating on data collected when the 1 mm collimated source was not in front of the crystal. What effect on counts collected on all boron(DC) strips did moving the source nearer to the crystal have?

2. Were a larger number of counts collected when the shielded, collimated source was moved across the crystal surface getting closer to a particular strip? The strip chosen for display was boron(DC) 24 because

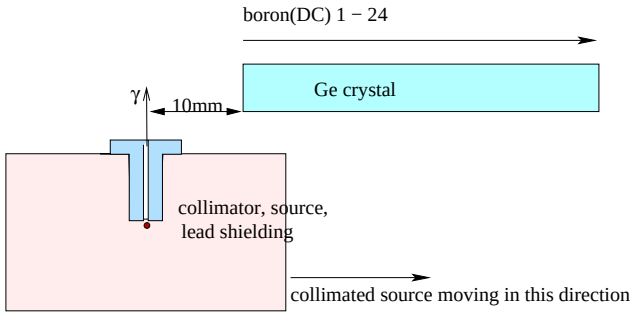

Figure D.1: 1 mm collimated source moved in 1 mm steps in a lateral direction towards the crystal.

it had the largest distance available to test the effectiveness of the shielding over.

The results from both can be seen in Figure D.2. While the collimated source was moved in 10, 1 mm steps towards boron(DC) 1, only the results from the 10 mm lateral distance position and the 4 mm lateral distance position have been displayed (a). No differences in the number of counts collected were observed as the collimated source was moved closer towards the crystal. This result is repeated in investigation 2 by the number of counts observed on boron(DC) 24 shown in Figure D.1 (b). As the collimated source was moved across the crystal towards the strip in 1 mm steps, no increase in the number of counts collected was observed. It can be concluded that the large observed background was not a result of poor source shielding.

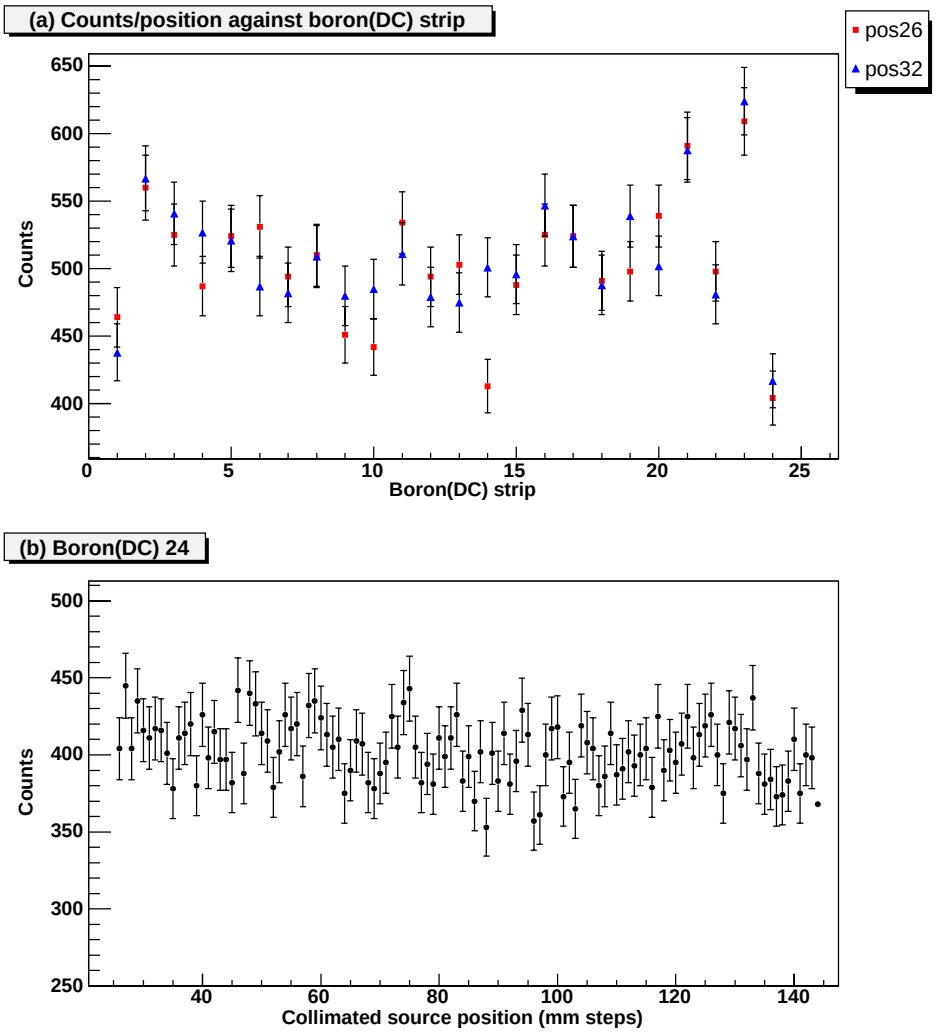

Figure D.2: (a) the counts recorded on the boron(DC) strips when the 1 mm collimated source is not positioned in front of the crystal. posy26 is a lateral position 10 mm away from boron(DC) 1. posy32 is a lateral position 4 mm away from boron(DC) 1. (b) the counts recorded on boron(DC) 24 while the 1 mm collimated source is raster scanned in 1 mm steps from a lateral position 10 mm away from boron(DC) 1 to a position 6 mm away from boron(DC) 24.

References

[Amm00] Amman, M., Luke, P.N. (2000): *Position-Sensitive Germanium Detectors for Gamma-Ray Imaging and Spectroscopy.* SPIE.

[Bar95] Barrett, H.H. et al. (1995): *Charge Transport in Arrays of Semiconductor Gamma-Ray Detectors.* Physical Review Letters, Vol. 75, No. 1.

[Bla99] Blair, J. et al. (1999): *Spatial Resolution Attainable in Germanium Detectors by Pulse Shape Analysis.* Nuclear Instruments and Methods in Physics Research A, 422, p. 331-336.

[Blo95] Bloomfield, P.M et al. (1995): *The Design and Physical Characteristics of a Small Animal Positron Emission Tomograph.* Physics in Medicine and Biology, Vol. 40, p. 1105-1126.

[Bur03] Burks, M. et al. (2003): *A 4-π Field of View Compton Imager Based on a Single Planar Germanium Detector.* IEEE Nuclear Science Symposium, Portland, Oregon, USA.

[Can74] Canali, C. et al. (1974): *Hot Hole Anisotropic Effect in Silicon and Germanium.* Solid State Communications, Vol. 15, p. 1213-1216.

[Cha99] Chatziioannou, A.F. (1999): *Performance Evaluation of microPET: A High Resolution Lutetium Oxyorthosilicate PET Scanner for Medical Imaging.* Journal of Nuclear Medicine, Vol. 40, p. 1164-1175.

[Cha02] Chatziioannou, A.F. (2002): *PET Scanners Dedicated to Molecular Imaging of Small Animal Models.* Molecular Imaging and Biology, Vol. 4, p. 47-63.

[Cob2] Coburn, W. et al. (2002): *Results of Charge Sharing Tests in a Ge-Strip Detector.* IEEE Transactions on Nuclear Science, Vol. 49.

[Coo05] Cooper, R.J. (2005): Private communication.

[Dab89] Dabrowski, W. (1989): *Transport Equations and Ramo's Theorem.* Progress in Quantum Electronics, Vol. 13, p. 233-266.

[Dav52] Davisson, C.M., Evans, R.D. (1952): *Gamma-Ray Absorption Coefficients.* Reviews of Modern Physics, Vol. 24, No. 2.

[Dav65] Davisson, C.M. (1965): Interaction of γ-Radiation with Matter *Alpha-, Beta- and Gamma-Ray Spectroscopy.* Ed. by Siegbahn, K., Pub. by North-Holland, p. 37-78.

[Des02] Descovich, M. (2002): *Improving the Position Resolution of Highly Segmented HPGe Detectors using Pulse Shape Analysis Methods.* Ph.D. Thesis, University of Liverpool.

[Gat01] Gatti, E. et al. (2001): *Spatial Localization of Multiple Simultaneous Hits in Segmented HPGe Detectors: A New Algorithm.* Nuclear Instruments and Methods in Physics Research A, 458, p. 738-744.

[Gou82] Goulding, F.S., Landis, D.A. (1982): *Signal Processing for Semiconductor Detectors.* IEEE Transactions on Nuclear Science, Vol. NS-29, No. 3.

[Gro03] Gros, S. et al. (2003): *Characterisation of a Clover Detector for the Development of a Compton Camera.* IEEE Nuclear Science Symposium, Portland, Oregon, USA.

[Gro05] Gros, S.A. (2005): *Characterizing the EXOGAM Clover.* Ph.D. Thesis, University of Liverpool.

[Ham96] Hamel, L.A. et al. (1996): *Signal Generation in CdZnTe Strip Detectors.* IEEE Transactions on Nuclear Science, Vol. 43, No. 3, p. 1422-1426.

[Har84] (1984): *Harshaw Radiation Detectors Catalogue.*

[Her05] Herzberg, R.D. (2005): Private communication.

[Hon04] (2004): *Improving DOI Information using 3-Layer Crystals for Small Animal PETs.* IEEE Nuclear Science Symposium, Rome, Italy.

[Kno00a] Knoll, G.F. (2000): *Radiation Detection and Measurement.* John Wiley & Sons, third edition, p. 53.

[Kno00b] Knoll, G.F. (2000): *Radiation Detection and Measurement.* John Wiley & Sons, third edition, p. 375.

[Kno00c] Knoll, G.F. (2000): *Radiation Detection and Measurement.* John Wiley & Sons, third edition, p. 611.

[Kno00d] Knoll, G.F. (2000): *Radiation Detection and Measurement.* John Wiley & Sons, third edition, p. 417.

[Knp65a] Knop, G., Paul, W. (1965): Interaction of Electrons. Ed. by Siegbahn, K., Pub. by North-Holland, p. 12.

[Knp65b] Knop, G., Paul, W. (1965): Interaction of Electrons. Ed. by Siegbahn, K., Pub. by North-Holland, p. 15.

[Kro95a] Kroeger, R.A. et al. (1995): *Spatial Resolution and Imaging of Gamma-Rays with Germanium Strip Detectors.* SPIE Proceedings, Vol. 2518, p. 236.

[Kro99] Kroeger, R.A. et al. (1999): *Charge Spreading and Position Sensitivity in a Segmented Planar Germanium Detector.* Nuclear Instruments and Methods in Physics Research A, 422, p. 206-210.

[Kro95b] Kroeger, R.A. et al. (1995): *Imaging in High Energy Astrophysics*. Ed. by Bassani, L. and di Cocco, G., Pub. by Kluwer Press, p. 325.

[Kro00] Kröll, Th. et al. (2004): *γ-Ray Tracking with the MARS Detector*. The European Physical Journal A, A20, p. 205-206.

[Kro01] Kröll, Th., Bazzacco, D. (2001): *Simulation and Analysis of Pulse Shapes from Highly Segmented HPGe Detectors for the γ-Ray Tracking Array MARS*. Nuclear Instruments and Methods in Physics Research A, 463, p. 227-249.

[Kur03] Kurfess, J.D. et al. (2003): *Development and Applications of Position-Sensitive Solid-State Gamma Ray Detectors*. Nuclear Instruments and Methods in Physics Research A, 505, p. 256-264.

[Laz03] Lazarus, I.H. (2003): *The GRT4 VME Pulse Processing Card for Segmented Germanium Detectors*. IEEE Nuclear Science Symposium, 2003, N29-36.

[Luk96] Luke, P.N. (1996): *Electrode Configuration and Energy Resolution in Gamma-Ray Detectors*. Nuclear Instruments and Methods in Physics Research A, 380, p. 232-237.

[Mal75] Malm, H.L. et al. (1975): *Gamma-Ray Spectroscopy with Single-Carrier Collection in High-Resistivity Semiconductors*. Applied Physics Letters, Vol. 26, No. 6.

[Mat] http://www.mathworks.com

[MCN] http://laws.lanl.gov/x5/MCNP/index.html

[Med04] Medina, P. et al. (2004): *A Simple Method for the Characterization of HPGe Detectors*. Instrumentation and Measurement Technology Conference 2004, Italy.

[Mih00] Mihailescu, L. et al. (2000): *The Influence of Anisotropic Electron Drift Velocity on the Signal Shapes of Closed-End HPGe Detectors.* Nuclear Instruments and Methods in Physics Research A, 447, p. 350-360.

[Mom99] Momayezi, M. et al. (1999): *Position Resolution in a Ge-Strip Detector.* SPIE Proceedings, Vol. 3768, p. 530.

[Nol94] Nolan, P.J. et al. (1994): *Large Arrays of Escape-Suppressed Gamma-Ray Detectors.* Annual Review of Nuclear and Particle Science, Vol. 45, p. 561-607.

[NSM] http://www.ioffe.rssi.ru/SVA/NSM/Semicond/Ge

[Ort] http://www.ortec-online.com/pdf/preamptut.pdf

[Pea02] Pearson, C.J. et al. (2002): *Digital Gamma-Ray Tracking Algorithms in Segmented Germanium Detectors.* IEEE Transactions on Nuclear Science, Vol. 49, No. 3.

[Phl02] Phlips, B.F. et al. (2002): *Small Animal PET Imaging with Germanium Strip Detectors.* IEEE Medical Imaging Conference, Norfolk, Virginia.

[Pro04] Protić, D., Krings, T. (2004): *Detection Characteristics of Ge Detectors with Microstructured Amorphous Ge Contacts.* IEEE Transactions on Nuclear Science, Vol. 51, No. 3.

[Pul03] Pullia, A. et al. (2003): *Extraction of Electrical Parameters of HPGe Segmented Detectors.* IEEE Nuclear Science Symposium, Portland, Oregon, USA.

[Rad88a] Radeka, V. (1988): *Low-Noise Techniques In Detectors.* Annual Review of Nuclear and Particle Science, Vol. 38, p. 222.

[Rad88b] Radeka, V. (1988): *Low-Noise Techniques In Detectors.* Annual Review of Nuclear and Particle Science, Vol. 38, p. 224.

[Ram39] Ramo, S. (1939): *Currents Induced by Electron Motion.* Proceedings of the Institute of Radio Engineers, Vol. 27, p. 584.

[Reg77] Reggiani, L. et al. (1977): *Hole Drift Velocity in Germanium.* Physical Review B, Vol. 16, No. 6.

[Sha02] Sharma, D.P. et al. (2002): *A Study of Charge Sharing in Pixellated Cadmium-Zinc-Telluride Detectors.* IEEE

[Sho38] Shockley, W. (1938): *Currents to Conductors Induced by a Moving Point Charge.* Journal of Applied Physics, Issue 10, p. 635.

[Sze02a] Sze, S.M. (2002): *Semiconductor Devices: Physics and Technology.* John Wiley & Sons, second edition, p. 93-99.

[Sze02b] Sze, S.M. (2002): *Semiconductor Devices: Physics and Technology.* John Wiley & Sons, second edition, p. 49.

[Tur05] Turk, G.H.B. (2005): Private communication.

[Val03] Valiente-Dobón, J.J. et al.(2003): *Performance of a 6x6 Segmented Germanium Detector for γ-Ray Tracking.* Nuclear Instruments and Methods in Physics Research A, 505, p. 174-177.

[Vet00] Vetter, K. et al. (2000): *Three-Dimensional Position Sensitivity in Two-Dimensionally Segmented HPGe Detectors.* Nuclear Instruments and Methods in Physics Research A, 452, p. 223.

[Wat97] Watanabe, M. et al. (1997): *A High Resolution Animal PET Scanner using Compact PS-PMT Detectors.* IEEE Transactions on Nuclear Science, Vol. 44, p. 1277-1282.

[Wul03a] Wulf, E.A. et al. (2002): *Timing Methods for Depth Determination in Germanium Strip Detectors.* Nuclear Instruments and Methods in Physics Research A, 505, p. 178-182.

[Wul02] Wulf, E.A. et al. (2002): *Depth Measurement in a Strip Detector.* IEEE Transactions on Nuclear Science, Vol. 49, p. 1876-1880.